Phase-Field Models for Microstructural Characterization of Electrode Materials

電極材料の組織・特性解析を実現するフェーズフィールドモデルの構築

January 2014

Shunsuke Yamakawa

Abstract

Chapter 1: Computational modeling studies are useful for elucidating the driving forces behind microstructure formation and for predicting the resultant microstructures. The phase-field method is a powerful technique that can predict various microstructural evolutions. In the context of improving the performance of polymer-electrolyte fuel cells (PEFCs) and Li-ion secondary batteries (LIBs), the phase-field method has been applied to electrode materials to predict microstructures in the length scales ranging from nanometers to micrometers. The objective of the present work is to first construct an effective phase-field model to describe the compositional variation and phase transformation within a single-alloy catalyst particle in a PEFC and provide information on the crucial aspects that affect the internal structure of a catalyst particle. The second objective is to construct an effective phase-field model to describe the Li diffusion process in polycrystalline $LiCoO_2$ in a LIB and explore the crucial aspects of anisotropic materials to quantitatively understand their Li transport properties.

Chapter 2: In this chapter, the development of a phase-field model that demonstrates the phase transformations and surface segregation within platinum-based alloy nanoparticles is described. Fe–Pt binary-alloy nanoparticles with diameters less than 10 nm were investigated. The calculations clearly showed that the surface segregation and phase transformations were sensitive to the alloy components and particle size. The degree of $L1_0$ ordering decreased with a decrease in the particle size. The calculated gradations were in good agreement

with the experimental results. The simulated phase boundary between the solid and liquid phases was slightly below that obtained with the classical model because of surface premelting, which is not considered in the classical model. In addition, FePt exhibited hardly any significant segregation, and an increase in the Pt concentration in the outermost surface was compensated by a decrease in the concentration in the sub-surface. The results were consistent with those obtained by previously reported Monte Carlo simulations. Thus, these results imply that the present phase-field model is sufficiently accurate to describe the internal structure of a single nanoparticle.

Chapter 3: In this chapter, a phase-field model that describes the radial distributions of the phase transformations and surface segregation in a single-alloy nanoparticle is introduced to clarify the overall behavior of surface segregation of various Pt-based alloy nanoparticles. From the results of the calculations for CrPt, FePt, CoPt, NiPt, CuPt, PdPt, IrPt, and AuPt binary nanoparticles with a diameter of 3 nm at 973 K, the compositional variation within a single particle was found to depend on the balance between the atomic interaction within particles and the surface free energy. In addition, the obtained specific steady-state composition of the surface varied significantly with alloy combination. Based on the general tendencies of a binary system to exhibit segregation, attempts to control the amount of platinum segregation on the surface using a ternary-alloy system were examined.

Chapter 4: To gain a quantitative understanding of the relationship between the morphology of the microstructure and Li diffusivity, phase-field models for non-Fickian Li diffusion in two-dimensional polycrystalline microstructures were

proposed by considering the grain size, spatial distribution of the crystal orientation for each grain, crystallographic anisotropy of the self-diffusion coefficient of Li, and Li diffusion along or across the grain boundary (GB) modeled as a thin layer. The simulation results showed that the apparent Li diffusivity was sensitive to the GB diffusivity, spatial distribution of the crystal orientation for each grain, and grain size. It was also found that the diffusivity of a small grained structure was determined by the properties of the grain boundary, while the diffusivity of a large-grained structure depended considerably on the relative orientation angle between neighboring grains, even when the GB diffusivity was large.

Chapter 5: In this chapter, the constant-current discharge properties of polycrystalline $LiCoO_2$ were theoretically investigated in relation to the grain size, spatial distribution of the crystal orientation for each grain, and GB diffusivity. The phase-field method to treat the Li diffusion generated from the elastic stress field associated with Li concentration is proposed in this chapter. The simulation results showed that the discharge properties were affected by the microstructure at a high discharge rate through modification of the Li diffusivity. Both the intergranular angle mismatch and GB diffusivity were determined to be crucial parameters for evaluating the apparent discharge properties. Since the Li diffusivity was promoted to alleviate the elastic stress, the discharge capacity slightly increased. The effect of the elastic strain energy was weaker than the effects of intergranular angle mismatch and GB diffusivity; however, the elastic strain energy led to a nontrivial change in the Li diffusivity during discharge.

Acknowledgments

I would like to express my sincere gratitude to Prof. Toshiyuki Koyama, who introduced me to the field of phase-field simulations and provided me with an opportunity to join Nagoya Institute of Technology. I am very grateful for the immense support, guidance, and encouragement from him throughout the work carried out for this thesis. Without his tremendous help, this thesis would not have been possible.

I am deeply grateful to Dr. Ryoji Asahi for helpful suggestions and valuable discussions. I wish to thank Dr. Yu Morimoto and Dr. Hajime Murata for providing information on experimental details. I would also like to thank Dr. Ryosuke Jinnouchi, Dr. Hisatsugu Yamasaki, Dr. Yoshiumi Kawamura, and Dr. Yuhki Tsukada for valuable discussions.

I also thank my colleagues in the theoretical and experimental groups at Toyota Central R&D Labs., Inc., from whom I received substantial help and insightful comments.

Table of Contents

Chapter 1
Introduction

This chapter begins with a brief introduction to high-performance batteries and battery electrode materials. Following an explanation of the numerical simulation techniques used for nanostructural characterization, the research objectives and the outline of the present thesis are described.

1.1 General Trends in High-Performance Batteries

As global energy consumption increases steadily, continuous depletion of fossil fuel resources and global warming caused by carbon dioxide emissions are turning into major obstacles that threaten the environment and prosperity of future generations [1]. Driven by immediate demands for alternative fuel resources that can replace existing fossil fuels, extensive studies are being conducted to develop new, clean, and efficient sources of energy. One interesting approach to improve the fuel efficiency and suppress carbon dioxide emissions in vehicles is the application of hybrid systems consisting of a secondary battery and engine. In such hybrid systems, a secondary battery that stores the electricity generated by the engine plays a major role in responding to significant changes in the power output of an electric motor caused by varying road conditions. Therefore, batteries that meet the demands of high energy storage and high power are required. Lithium ion batteries (LIBs) have attracted

increased attention recently as high-performance secondary batteries for application in vehicles.

Typical LIBs use carbon as the active anode material and lithium metal oxides as active materials for the cathode. The electrochemical reactions [2] occurring at the anode and cathode are represented by Eqs. (1.1) and (1.2), respectively:

$$\mathrm{C} + x\,\mathrm{Li}^{+} + xe^{-} \underset{\text{Discharge}}{\overset{\text{Charge}}{\rightleftarrows}} \mathrm{Li}_x\,\mathrm{C}, \tag{1.1}$$

$$\mathrm{Li}\,\mathrm{MO}_2 \underset{\text{Discharge}}{\overset{\text{Charge}}{\rightleftarrows}} \mathrm{Li}_{1-x}\,\mathrm{MO}_2 + x\,\mathrm{Li}^{+} + xe^{-}. \tag{1.2}$$

As shown in Fig. 1.1, the ionic conduction between the two electrodes is maintained by a liquid or solid electrolyte. The intercalation–deintercalation of Li in the active materials of both electrodes is a fundamental phenomenon that determines the performance of the batteries. In particular, Li-ion conduction in the cathode material substantially affects the performance of Li-ion batteries at high charge/discharge rates. Therefore, there are continual attempts to improve the power density of lithium batteries by enhancing the ionic diffusivity in cathode materials [2,3].

However, in order to build a vehicle with zero emission, manufacturers are intensively promoting the replacement of a reciprocating engine with fuel-cell systems. The fuel-cell system is usually used in combination with a secondary battery system. In typical hydrogen–oxygen fuel cells [4], the following electrochemical reactions occur at the anode (Eq. (1.3)) and cathode (Eq. (1.4)):

$$\mathrm{H}_2 \rightarrow 2\,\mathrm{H}^{+} + 2e^{-}, \tag{1.3}$$

$$\frac{1}{2}O_2 + 2H^+ + 2e^- \rightarrow H_2O. \quad (1.4)$$

A typical fuel-cell system finding application in vehicles uses a polymer electrolyte [5] to ensure adequate performance at room temperature. These fuel cells are called polymer-electrolyte fuel cells (PEFCs) [6]. As shown in Fig. 1.2, the sequential processes occurring in a PEFC are the (1) dissolutions of hydrogen and oxygen gases at the gas–electrolyte interface, (2) diffusions of dissolved hydrogen and oxygen into the electrolyte–catalyst interface, (3) electrochemical reaction at the catalyst–electrolyte interface, (4) conduction of electrons by the current collector, and (5) transport of protons from the anode across the electrolyte to the cathode. One of the key challenges in achieving high-performance fuel-cell systems is the development of highly effective electrocatalysts for oxygen reduction at the cathode. Thus far, numerous electrocatalysts including pure platinum and platinum alloys have been proposed.

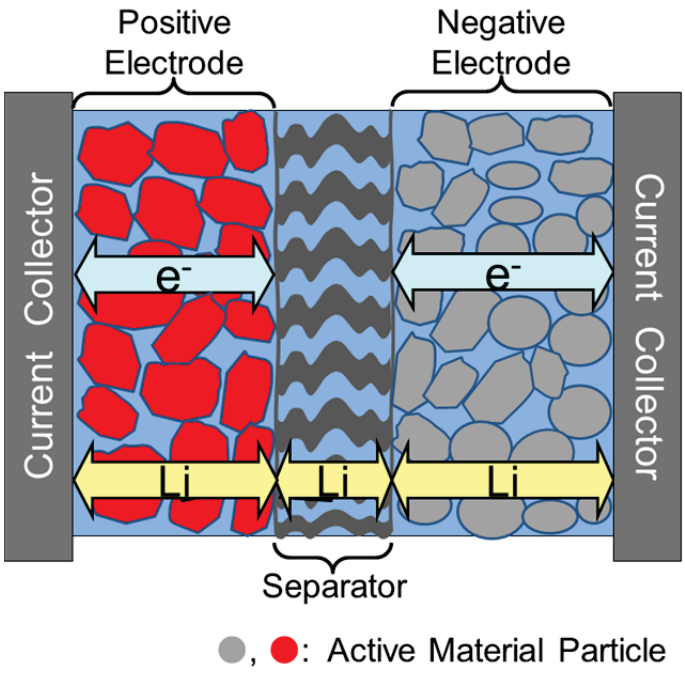

Fig. 1.1. Schematic illustrations of a LIB system.

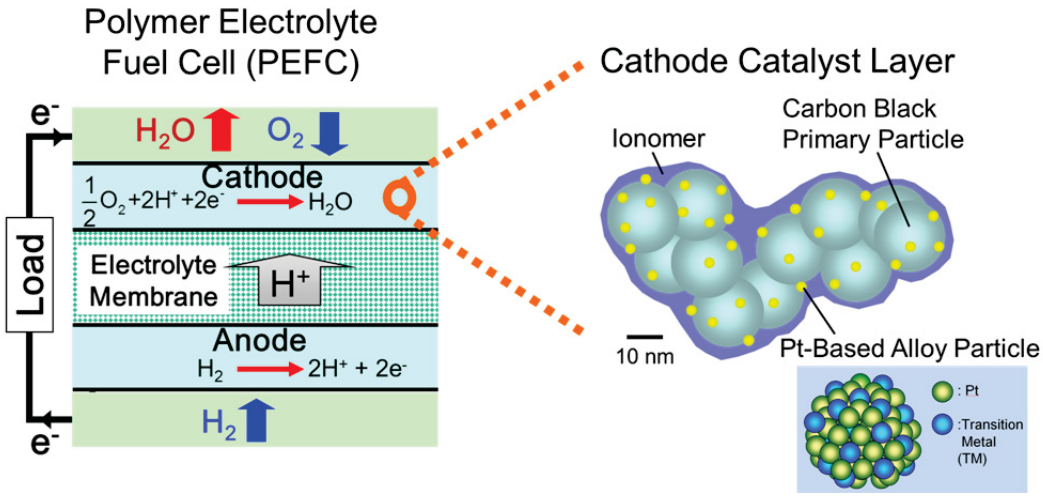

Fig. 1.2. Schematic illustrations of a PEFC system and an electrocatalyst supported on the carbon substrate.

1.2 Challenges Encountered in Electrode Materials

This section briefly reviews the challenges encountered in achieving high-performance electrode materials for PEFCs and LIBs.

1.2.1 Electrocatalysts in PEFCs

Recently, intensive efforts have been made to develop PEFCs for applications in vehicles [7]. Nanoscale particles of platinum supported on a carbon carrier are widely used as a catalyst for PEFCs. To achieve further improvement in the oxygen reduction reaction (ORR), shown in Eq. (1.4), in the cathode layers of PEFCs, implementations of platinum–transition-metal alloy nanoparticles as cathode electro-catalysts are expected [8]. The alloying technique is also expected to reduce the required amount of platinum loading by replacing some platinum with less expensive metals. Because the catalytic activity of the alloys in the ORR is significantly affected by the surface structure, the surface structure of the platinum alloy nanoparticles has been evaluated as a function of the alloying element and its composition [9]. Theoretical estimations, including first-principles calculations, indicate that the catalytic activity of a Pt–3d-transition-metal binary alloy depends on the oxygen adsorption energy, which is explained by the d-band center [10]. Among numerous candidate alloys, the catalytic activities of some Pt-based alloys are predicted to be superior to that of pure platinum. Recently, evaluations of the

electro-catalyst alloy system have been expanded from binary to ternary alloys [11,12].

On the other hand, it has been experimentally observed that the alloy compositions of nanoparticles often differ from the nominal bulk composition [13]. During the nanoparticle fabrication process, a compositional difference between the bulk and the alloy surface may be induced by differences in the surface energies of the alloying elements and changes in the interaction energies between them. This compositional difference is known as surface segregation [14], which affects the catalytic activities of the alloys [15]. However, the diameters of the currently used pure platinum catalyst particles are controlled to remain below 10 nm to ensure the availability of a large surface area for the electrochemical reaction [16], as shown in Fig. 1.2. On the scale of a few nanometers, the effect of the surface energy on the thermodynamic equilibrium is inversely proportional to the particle size, which causes degradation because of Ostwald ripening [16]. Therefore, the particle size is also expected to affect surface segregation. To overcome these obstacles when designing and fabricating binary-alloy nanoparticles, it is necessary to understand the fundamental effects of particle size, alloy composition, and heat-treatment temperature on the microstructure formation.

1.2.2 Positive Electrode Materials in LIBs

Layered Li transition-metal oxides, which are characterized by two-dimensional (2D) Li diffusion paths [17–20], are the most widely used positive-electrode active materials in LIBs. They are expected to allow the occurrence of topotactic electrochemical reactions for high power applications [21]. Nevertheless, a Li transition-metal oxide contains many shortcomings, such as limited range of current density, that need to be resolved.

Schematic illustrations of a porous electrode in a liquid-state battery and a thin-film electrode in an all-solid-state battery are shown in Fig. 1.3. In a commercial liquid-state LIB, the electrolyte, which intrudes into pores within a secondary particle, may provide short-circuit transport paths for Li. Nevertheless, experimental observation [22] has shown that secondary particles contain numerous grain boundaries, which implies that a primary particle within a secondary particle is not completely isolated and the surface is not entirely exposed to the electrolyte. Furthermore, in the case of an all-solid-state battery with a flat thin-film electrode, since most crystal grains are not in direct contact with the solid electrolyte particles, intergranular diffusion between crystal grains plays a crucial role in the Li transport.

$LiCoO_2$ is the most popular cathode material, and its crystal structure [23] is represented in Fig. 1.4. The self-diffusion coefficient, D_{self}, of Li in Li_xCoO_2 has been investigated using both theoretical and experimental approaches [24–26]. The value of D_{self} estimated from muon spin spectroscopy [24] was found to range from 1×10^{-10} to 1×10^{-9} $cm^2 \cdot s^{-1}$ for Li_xCoO_2 ($0.5 < x < 0.8$) at 300 K,

which was in good agreement with the value calculated from first principles [26]. However, the chemical diffusion coefficient, D_{chem}, evaluated by electrochemical measurements, was found to vary from 1×10^{-12} to 1×10^{-10} $cm^2 \cdot s^{-1}$ [27,28] for (104)-textured thin films. Grains with their (104) planes parallel to the Li transport direction was shown to facilitate Li transport [29]. It is known that D_{chem} can be expressed as a product of D_{self} and the thermodynamic factor, ω. Since the binary solution of Li–vacancy in the 2D layer is not ideal, the value of ω must be larger than 1 for a wide range of Li concentrations. Therefore, D_{chem} is expected to be larger than D_{self}, which contradicts the experimental data. Thus, the transport properties of Li appear to be limited by microstructural inhomogeneities such as crystal anisotropy, grain size, and grain boundaries.

In order to fabricate materials with improved performances, an understanding of the properties that contribute to the performance of LIBs is necessary. Without an accurate and detailed comprehension of the Li-ion conduction mechanism at the nanometer to micrometer levels, the rational design of Li-based active materials with better performance will remain a challenge. The details of the effect of the microstructure on the Li-ion conduction are yet to be clearly and completely understood, however, because of the difficulties involved in the experimental assessment of the conduction mechanism.

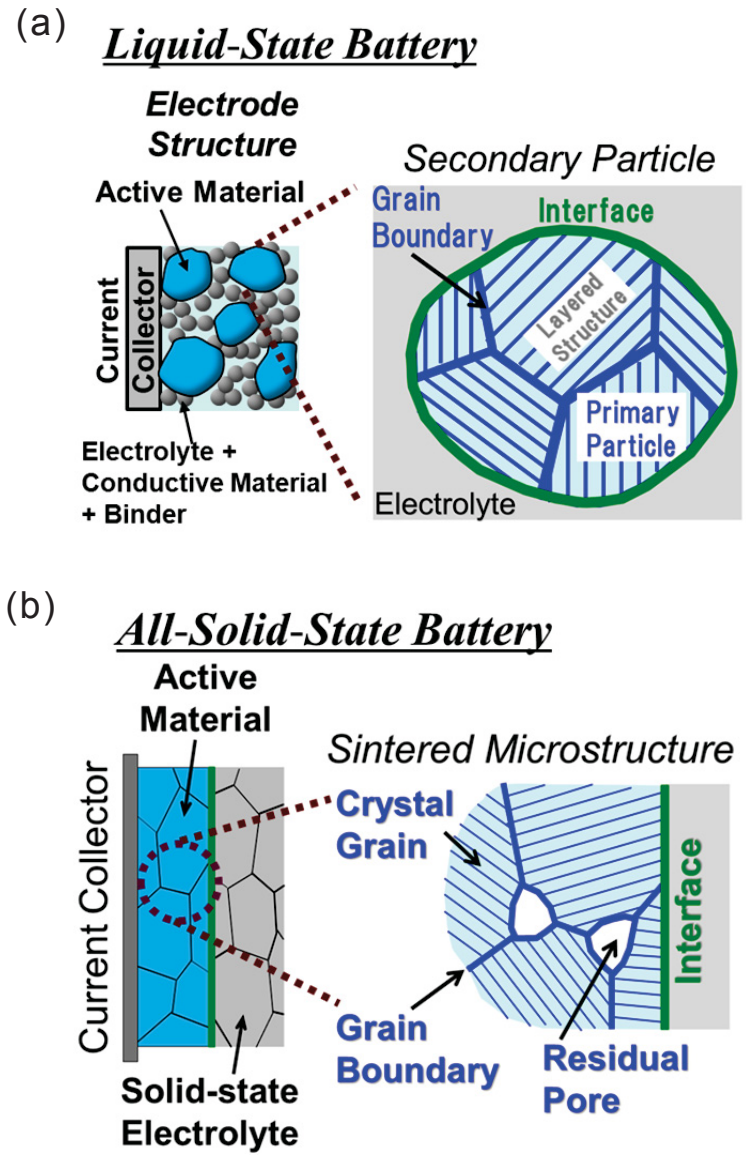

Fig. 1.3. Schematic illustrations of (a) a porous electrode in a liquid-state LIB and (b) a thin-film electrode in an all-solid-state LIB.

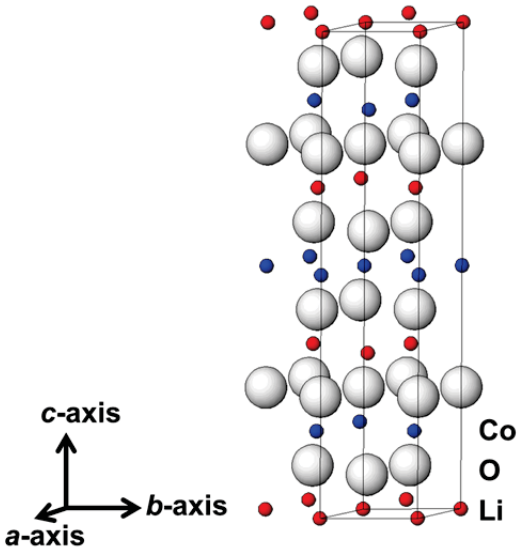

Fig. 1.4. Crystal structure of $LiCoO_2$.

1.3 Simulation Methodology

This section explains the methodology used for the numerical simulation of the nanostructural and microstructural characteristics. The temporal evolution of the microstructure is calculated using the phase-field method based on the free-energy function.

1.3.1 Phase-Field Method

The methods of simulating the material structure on the nanometer to micrometer scale are roughly classified into two categories. The first class of

methods simulate the temporal evolution of the microstructure by directly calculating the atomic motion. In methods belonging to the second category, the evolution of the microstructure is described by calculating the transform of a set of spatially dependent field variables. Molecular dynamics and Monte Carlo methods based on classical or first-principles potential typically belong to the first group. The phase-field method, which is a continuum model belonging to the second group and is in accordance with local thermodynamic equilibrium, has been widely used since the second half of the 1980s to study a variety of microstructure formations such as dendritic growth, spinodal decomposition, and grain growth [30].

In the phase-field method, the conservative variables, which characterize the atomic concentrations, and the non-conservative variables, which characterize the structural heterogeneities, are defined as the field variables in the simulation area. The total free energy of the simulated system is described using these variables. The temporal evolutions of the conservative variables are calculated using the Cahn–Hilliard equation [31], which is represented as follows:

$$\frac{\partial c}{\partial t} = \nabla \cdot \left(M \nabla \frac{\delta G_{\text{sys}}}{\delta c} \right), \tag{1.5}$$

where c is the local atomic concentration, G_{sys} represents the total free energy of the simulated system, and M is the mobility of the component that correlates with the atomic self-diffusion coefficient, D.

The temporal evolutions of the non-conservative variable are calculated using the Allen–Cahn equation [32]:

$$\frac{\partial s}{\partial t} = -L_s \frac{\delta G_{\text{sys}}}{\delta c}. \tag{1.6}$$

In the above equation, s is the so-called phase-field parameter, which is usually introduced to describe the phase interface or grain boundary, and L_s denotes the mobility of the interface or boundary. Finally, as a consequence of the temporal evolution, quasi-stationary microstructures corresponding to the minimum free energy are obtained.

Depending on the type of interactions, a number of variations of the expression of G_{sys} for the targeted system should be considered. Typically, G_{sys} includes G_{c}, E_{grad}, and E_{str}, which correspond to the bulk chemical free energy, the gradient energy, and the elastic strain energy, respectively. Each of these terms is described in detail in the following sections.

1.3.1.1 Bulk Free Energy

The bulk stress-free chemical free energy, G_{c}, is assumed to be the volume integral of a well-defined local free energy density over the entire volume, V:

$$G_{\text{c}} = \frac{1}{V}\int_{\mathbf{r}} G_{\text{m}}(\mathbf{r},t)\,\mathrm{d}\mathbf{r}, \tag{1.7}$$

where $\mathbf{r}$ is the position vector; t is the time; and G_{m} is the molar Gibbs free energy, which is estimated assuming that the thermodynamic fields are spatially uniform and can be approximated by a regular solution model. The interaction energies between the atoms are evaluated by the calculation of phase diagram (CALPHAD) method [33], an important technique based on thermodynamic

models. In this method, various parameters are determined using the model to appropriately represent the experimental observations or the theoretically estimated phase boundaries and thermodynamic properties. For example, the molar free energy is modeled as a substitutional binary solution according to the following equation:

$$G_{\mathrm{m}} = \sum_{i=A\mathrm{or}B} c_i {}^{\circ}G_i + RT \sum_{i=A\mathrm{or}B} c_i \ln c_i + c_{\mathrm{A}} c_{\mathrm{B}} L_{\mathrm{AB}}, \tag{1.8}$$

where c_{A} and c_{B} are the molar fractions of the elements A and B, respectively; ${}^{\circ}G_i$ is the Gibbs formation energy of the pure element i; and R and T are the gas constant and absolute temperature, respectively. The second term is the ideal entropy of mixing, and the last term is the excess Gibbs free energy. The term L_{AB} is the binary interaction parameter, and the form of the composition dependence, which is known as the Redlich–Kister (RK) power series, is given by

$$L_{\mathrm{AB}} = \sum_{\upsilon=0}^{k} \left(c_{\mathrm{A}} - c_{\mathrm{B}}\right)^{\upsilon} {}^{\upsilon}L_{\mathrm{AB}}, \tag{1.9}$$

where ${}^{\upsilon}L_{\mathrm{AB}}$ represents the parameters in the RK series. To describe the ordered phase, two or more sublattices are used. For example, a binary alloy using four sublattices can be expressed as

$$\left(A, B\right)_{0.25}\left(A, B\right)_{0.25}\left(A, B\right)_{0.25}\left(A, B\right)_{0.25}. \tag{1.10}$$

The Gibbs free energy equation for this ordered model is divided into two parts as shown in Eq. (1.11). The two portions indicate the contribution from the disordered state, $G_{\mathrm{m}}^{\mathrm{dis}}$, and that from the long-range ordering, $\Delta G_{\mathrm{m}}^{\mathrm{ord}}$:

$$G_{\mathrm{m}} = G_{\mathrm{m}}^{\mathrm{dis}}\left(c_i\right) + \Delta G_{\mathrm{m}}^{\mathrm{ord}}\left(y_i^{(s)}\right). \tag{1.11}$$

The free energy contribution from $G_{\mathrm{m}}^{\mathrm{dis}}$ is provided by Eq. (1.8). In the above equation, y_i is the site fraction of the constituent i on the sublattice s, which is defined by the following equation:

$$c_i = 0.25\sum_{s=1}^{4} y_i^{(s)}. \tag{1.12}$$

To ensure that $\Delta G_{\mathrm{m}}^{\mathrm{ord}}$ is zero in the disordered state, the ordered term in a four-sublattice model is described by

$$\Delta G_{\mathrm{m}}^{\mathrm{ord}}\left(y_i^{(s)}\right) = G_{\mathrm{m}}^{\mathrm{ord}}\left(y_i^{(s)}\right) - G_{\mathrm{m}}^{\mathrm{ord}}\left(c_i\right). \tag{1.13}$$

The expression for the ordered term in a four-sublattice model with an arbitrary number of components is given in the following form:

$$G_{\mathrm{m}}^{\mathrm{ord}} = \sum_i \sum_j \sum_k \sum_l y_i^{(1)} y_j^{(2)} y_k^{(3)} y_l^{(4)} {}^{\circ}G_{i:j:k:l} + 0.25RT\sum_s \sum_i y_i^{(s)} \ln y_i^{(s)} + {}^{E}G_{\mathrm{m}}, \tag{1.14}$$

where ${}^{\circ}G_{i:j:k:l}$ is the Gibbs free energy of formation with components i, j, k, and l for each sublattice site. The excess Gibbs free energy can be written as follows using interaction parameters:

$$\begin{aligned} {}^{E}G_{\mathrm{m}} = & \sum_{i_1} \sum_{i_2>i_1} \sum_j \sum_k \sum_l y_{i_1}^{(r)} y_{i_2}^{(r)} y_j^{(s)} y_k^{(t)} y_l^{(u)} L_{i_1,i_2:j:k:l} + \cdots + \\ & \sum_{i_1} \sum_{i_2>i_1} \sum_{j_1} \sum_{j_2>j_1} \sum_k \sum_l y_{i_1}^{(r)} y_{i_2}^{(r)} y_{j_1}^{(s)} y_{j_2}^{(s)} y_k^{(t)} y_l^{(u)} L_{i_1,i_2:j_1,j_2:k:l} + \cdots + . \end{aligned} \tag{1.15}$$

Recently, thermodynamic assessments using the CALPHAD technique have been carried out for a number of alloy systems [33]. Therefore, the phase-field method can be applied extensively to numerous alloy systems in combination with the CALPHAD database.

1.3.1.2 Gradient Energy

If all of the thermodynamic fields are not spatially uniform, then G_c (it is homogeneous in Sec. 1.3.1.1) must be supplemented by E_{grad} to account for the energetic interactions between the system and its environment. In this approach, the changes in the thermodynamic variables are assumed to change smoothly from one phase or domain to another [34]. By introducing this term, phase-field models can overcome the computational difficulty of tracking a moving boundary, which is usually diffuse in real physical systems. Therefore, in this case, the total free energy is the sum of two different functions as shown below:

$$G_{sys} = G_c + E_{grad}. \tag{1.16}$$

To derive E_{grad}, the Taylor series about G_c in terms of the derivatives of the concentration, c, is used and is approximated as follows:

$$G_c\left(c,\nabla c,\nabla^2 c\right) \approx G_c\left(c,0,0\right) + \mathbf{K}_0\left(c\right)\cdot\left(\nabla c\right) + K_1\left(c\right)\left(\nabla^2 c\right) + K_2\left(c\right)\left(\nabla c\right)^2. \tag{1.17}$$

The first term on the right corresponds to the homogeneous chemical free energy. A value of 0 is assigned to $\mathbf{K}_0$ to ensure that the energy is invariant with coordinate transformation. Therefore, E_{grad} is defined as

$$\begin{aligned} E_{grad} &= \frac{1}{V}\int_{\mathbf{r}}\left[K_1\left(c\right)\left(\nabla^2 c\right) + K_2\left(c\right)\left(\nabla c\right)^2\right]\mathrm{d}\,\mathbf{r} \\ &= \frac{1}{V}\int_{\mathbf{r}}\left[-\frac{\partial K_1}{\partial c} + K_2\left(c\right)\right]\left(\nabla c\right)^2\,\mathrm{d}\,\mathbf{r} \\ &= \frac{1}{V}\int_{\mathbf{r}}\frac{1}{2}\kappa\left(c\right)\left(\nabla c\right)^2\,\mathrm{d}\,\mathbf{r}, \end{aligned} \tag{1.18}$$

where the term κ is a function of the concentration:

$$\kappa\left(c\right) = 2\left[-\frac{\partial K_1}{\partial c} + K_2\left(c\right)\right]. \tag{1.19}$$

However, it is assumed to have a constant value in practical applications.

The gradient energy coefficient, κ, can be determined from the relationship between the free energy function and surface energy [35,36]. Considering a surface with a gradient only in the x direction, the excess free energy, $\Delta G_{\text{interface}}$, across the interface is expressed as

$$\Delta G_{\text{interface}} = \frac{1}{V}\int_{\mathbf{r}} [\Delta f(c) + \frac{\kappa}{2}(\mathrm{d}c/\mathrm{d}x)^2]\mathrm{d}\mathbf{r} = S\gamma, \tag{1.20}$$

$$\gamma = \frac{1}{V}\int_{-\infty}^{\infty} [\Delta f(c) + \frac{\kappa}{2}(\mathrm{d}c/\mathrm{d}x)^2]\mathrm{d}x. \tag{1.21}$$

In the above equation, S is the interfacial area, and γ is the excess free energy per unit area, which is usually called the interfacial (surface) energy. In addition, Δf indicates the difference between the chemical free energy, G_{c}, at the interface and the linear combinations of the free energies of two homogeneous phases. At equilibrium, when c is treated as stationary points of γ, the following relationship is satisfied:

$$\frac{\partial \gamma}{\partial c} = 0. \tag{1.22}$$

However, when c, which is a function of x, is regarded as a stationary function that yields a stationary value of γ, the Euler–Lagrange equation (given below) is derived using a variational method:

$$I - \left(\frac{\mathrm{d}c}{\mathrm{d}x}\right)\left[\frac{\partial I}{\partial(\mathrm{d}c/\mathrm{d}x)}\right] = 0, \tag{1.23}$$

where

$$I = \Delta f(c) + \frac{\kappa}{2}(\mathrm{d}c/\mathrm{d}x)^2. \tag{1.24}$$

The following relationship is derived from Eq. (1.24):

$$\Delta f(c) - \frac{\kappa}{2}(\mathrm{d}c/\mathrm{d}x)^2 = const. \tag{1.25}$$

Since both Δf and dc/dx are zero at $x = \pm\infty$, *const* in Eq. (1.25) is equal to zero as well and the following relationship is obtained:

$$\Delta f(c) = \frac{\kappa}{2}(\mathrm{d}c/\mathrm{d}x)^2. \tag{1.26}$$

Substituting Eq. (1.26) to Eq. (1.21) yields

$$\gamma = \frac{2}{V}\int_{-\infty}^{\infty} \Delta f(c)\,\mathrm{d}x, \tag{1.27}$$

and modifying Eq. (1.26) gives

$$\mathrm{d}x = \sqrt{\frac{\kappa}{2\Delta f(c)}}\,\mathrm{d}c. \tag{1.28}$$

Therefore, Eq. (1.27) can be expressed as

$$\gamma = \frac{1}{V}\int_{c_\mathrm{B}}^{c_\mathrm{A}} \sqrt{2\kappa\Delta f(c)}\,\mathrm{d}c\,, \tag{1.29}$$

where the variables c_A and c_B denote the equilibrium concentrations of the two phases, and the coefficient κ is determined using the excess energy, Δf, and γ. The thickness of the interfacial layer, Δd, can be approximated by the following equation from the concentration gradient when Δf is maximized:

$$\Delta d = (c_\mathrm{A} - c_\mathrm{B})/(\mathrm{d}c/\mathrm{d}x) = (c_\mathrm{A} - c_\mathrm{B})[\kappa/(2\Delta f_{\max})]^{1/2}. \tag{1.30}$$

1.3.1.3 Elastic Strain Energy

In some cases of microstructure formation, the elastic strain energy, E_{str}, caused by the lattice mismatch also contributes to the total free energy [37]. In this case, the total free energy is the sum of three different functions:

$$G_{\mathrm{sys}} = G_{\mathrm{c}} + E_{\mathrm{grad}} + E_{\mathrm{str}}. \tag{1.31}$$

Using the Einstein summation convention [37], the term E_{str} is expressed as

$$E_{\mathrm{str}} = \frac{1}{2V}\int_{\mathbf{r}} C_{ijkl}(\mathbf{r})\left[\varepsilon_{ij}^{c}(\mathbf{r},t) - \varepsilon_{ij}^{0}(\mathbf{r},t)\right]\left[\varepsilon_{kl}^{c}(\mathbf{r},t) - \varepsilon_{kl}^{0}(\mathbf{r},t)\right]\mathrm{d}\mathbf{r}, \tag{1.32}$$

where C_{ijkl} is the elastic stiffness constant, and $\varepsilon_{ij}^{\mathrm{c}}$ and ε_{ij}^{0} are the constrained strain and the eigenstrain, respectively. The term E_{str} is practically evaluated by calculating $\varepsilon_{ij}^{\mathrm{c}}$ for a given C_{ijkl} and ε_{ij}^{0}. The term $\varepsilon_{ij}^{\mathrm{c}}$ is calculated using the stress equilibrium equation, as described in detail in Sec. 5.2.1.

1.3.2 Charge Transfer Reactions

Processes involving the exchange of charged species at the interface between the electrolyte and the electrodes are referred to as charge transfer reactions or Faradaic reactions. The theories that can quantitatively rationalize the kinetics of electrode reactions [38] are briefly explained in this section. A typical electrode reaction proceeds as follows:

$$\mathrm{O}^{z+} + ne^{-} \rightleftarrows \mathrm{R}^{(z-n)+}. \tag{1.33}$$

The equilibrium potential of the electrode reaction is obtained using the Nernst equation according to

$$U_{\mathrm{eq}} = U^{0} + \frac{RT}{nF}\ln\frac{a_{\mathrm{O}}}{a_{\mathrm{R}}} = U^{0'} + \frac{RT}{nF}\ln\frac{c_{\mathrm{O}}}{c_{\mathrm{R}}}, \tag{1.34}$$

where U^{0} and $U^{0'}$ are the standard and formula redox potentials, respectively; a_{O} and a_{R} indicate the activity coefficients of the reaction product and reactants, respectively; c_{O} and c_{R} indicate the interfacial concentrations of the reaction product and reactants, respectively. The rates per unit surface area of the forward and backward reactions, v_{f} and v_{b}, respectively, are written in the following form using the reaction constants, k_{f} and k_{b}:

$$v_{\mathrm{f}} = k_{\mathrm{f}}c_{\mathrm{O}}, \quad v_{\mathrm{b}} = k_{\mathrm{b}}c_{\mathrm{R}}. \tag{1.35}$$

The Faraday current density, i, generated by the electrode interface reaction is obtained by multiplying the reaction rate with the Faraday constant, F, and the number of transferred charges, n, and by subtracting the current in the forward and backward reactions:

$$i = nF\left(v_{\mathrm{f}} - v_{\mathrm{b}}\right) = nF\left(k_{\mathrm{f}}c_{\mathrm{O}} - k_{\mathrm{b}}c_{\mathrm{R}}\right). \tag{1.36}$$

The kinetic rate constants of the electrochemical reaction are obtained from

$$k_{\mathrm{f}} = A_{\mathrm{f}}\exp\left(-\frac{\Delta G_{\mathrm{f}}}{RT}\right), \quad k_{\mathrm{b}} = A_{\mathrm{b}}\exp\left(-\frac{\Delta G_{\mathrm{b}}}{RT}\right), \tag{1.37}$$

where the coefficients A_{f} and A_{b} are the frequency factors, and ΔG_{f} and ΔG_{b} are the activation energies. This theory is based on the modeling of the reaction pathway as a curve through an energy landscape. The activation energy is then explicitly quantified as the difference between the energy minimum occupied by the reactants and the energy of the saddle point over which the reaction pathway

must traverse on its way to achieve the products. When an external electric field, U, is applied, the activation energy is altered according to

$$\Delta G_{\mathrm{f}} = \Delta G_{\mathrm{f}}^{0} + \alpha nFU, \quad \Delta G_{\mathrm{b}} = \Delta G_{\mathrm{b}}^{0} - (1-\alpha)nFU, \tag{1.38}$$

where α is the transfer coefficient. By substituting Eq. (1.37) and Eq. (1.38) into Eq. (1.36), the following equation is obtained:

$$i = nFk^{0}\left\{c_{\mathrm{O}} \exp\left[-\frac{\alpha nF\left(U-U^{0'}\right)}{RT}\right] - c_{\mathrm{R}} \exp\left[\frac{(1-\alpha)nF\left(U-U^{0'}\right)}{RT}\right]\right\}, \tag{1.39}$$

where

$$k^{0} = A_{\mathrm{f}} \exp\left(-\frac{\Delta G_{\mathrm{f}}^{0} + \alpha nFU^{0'}}{RT}\right) = A_{\mathrm{b}} \exp\left(-\frac{\Delta G_{\mathrm{b}}^{0} - (1-\alpha)nFU^{0'}}{RT}\right). \tag{1.40}$$

Here, i is assumed to be zero at equilibrium. Furthermore, using the exchange current density, i_0, which is defined as $i_0 = nFk^{0}\left(c_{\mathrm{O}}^{*}\right)^{1-\alpha}\left(c_{\mathrm{R}}^{*}\right)^{\alpha}$, and the over potential, η, which is defined as $\eta = U - U_{\mathrm{eq}}$, Eq. (1.39) can be rewritten as

$$i = i_0\left\{\frac{c_{\mathrm{O}}}{c_{\mathrm{O}}^{*}} \exp\left[-\frac{\alpha nF\eta}{RT}\right] - \frac{c_{\mathrm{R}}}{c_{\mathrm{R}}^{*}} \exp\left[\frac{(1-\alpha)nF\eta}{RT}\right]\right\}. \tag{1.41}$$

This equation is known as the current–overpotential equation. The first and second terms on the right hand side describe the cathodic and anodic components of current. At sufficiently large currents or large overpotentials, either of the two current components is negligible. When i_0 is small, the excess potential associated with providing the activation energy required to satisfy the current density is more visible. This kind of excess potential is usually called the activation overpotential. However, when the exchange current is large, the current is limited by mass transfer. In this case, the observed overpotential is associated with the surface concentrations of the oxidant and the reductant, and

the potential is called the concentration overpotential, which is required to drive the mass transfer.

1.3.3 Finite-Volume Method

The cell-centered finite-volume method (FVM) is a general numerical scheme for solving partial differential equations (PDEs) [39]. This section explains the procedure for calculating the Cahn–Hilliard equation, shown in Eq. (1.5), using the FVM. Here, it is assumed that the scalar variable c is locally conserved. Conservation of the concentration variable is derived by the following equation using the flux $\boldsymbol{J}$ for c:

$$\frac{\partial c}{\partial t} = -\nabla \cdot \boldsymbol{J}, \tag{1.42}$$

$$\boldsymbol{J} = -M\nabla\mu; \quad \mu = \delta G_{\mathrm{sys}} / \delta c, \tag{1.43}$$

where μ represents the diffusion potential. The simulation region is divided into many small control volumes for a one-dimensional problem, as shown in Fig. 1.5.

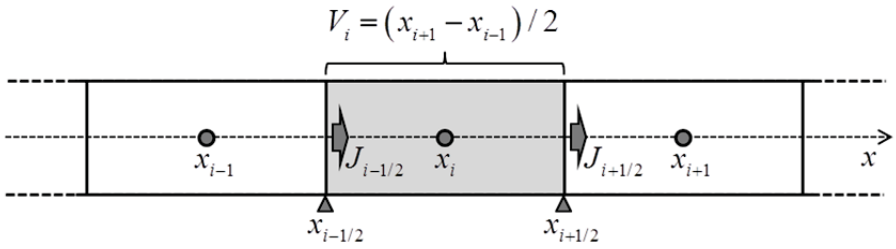

Fig. 1.5 Schematic illustration of a one-dimensional model.

By integrating both sides of Eq. (1.42) in the control volume at node i (shown in Fig. 1.5) using the divergence theorem (also called Gauss's theorem), the right hand side of Eq. (1.42) can be expressed as

$$-\int_{V_i} \nabla \cdot \boldsymbol{J}\, \mathrm{d}V = -\int_{S_i} \boldsymbol{J} \cdot \mathrm{d}\boldsymbol{S} = -\left(S_{i+1/2} J_{i+1/2} - S_{i-1/2} J_{i-1/2}\right). \tag{1.44}$$

Here, the direction of the surface vector **S** is set in the outward direction of the control volume surface such that **S** at node $i + 1/2$ is in the direction of $+x$ and **S** at node $i - 1/2$ is in the direction of $-x$. $S_{i\pm1/2}$ represents the surface area at intermediate nodes between two cells and is defined by

$$S_{i\pm1/2} = \begin{cases} 1, & \text{One-Dimensional} \\ 4\pi\left(\dfrac{x_{i\pm1} + x_i}{2}\right)^2, & \text{Spherical Symmetry} \end{cases}. \tag{1.45}$$

The left hand side of Eq. (1.42) can be expressed as

$$\int_{V_i} \frac{\partial c}{\partial t}\, \mathrm{d}V \approx \frac{\partial c_i}{\partial t} V_i, \tag{1.46}$$

where V_i denotes the cell volume of the node i, which can be determined using

the trapezoidal rule as follows:

$$V_i = \begin{cases} \dfrac{1}{2}(x_{i+1} - x_{i-1}), & \text{One-Dimensional} \\ \dfrac{4\pi}{3}\left[\left(\dfrac{x_{i+1}+x_i}{2}\right)^3 - \left(\dfrac{x_i + x_{i-1}}{2}\right)^3\right], & \text{Spherical Symmetry} \end{cases} . \tag{1.47}$$

The following equation is obtained from Eqs. (1.44) and (1.46):

$$\frac{\partial c_i}{\partial t} = -\left(S_{i+1/2}J_{i+1/2} - S_{i-1/2}J_{i-1/2}\right) / V_i . \tag{1.48}$$

Here, the flux at the intermediate points $i \pm 1/2$ can be obtained (as shown in Eq. (1.49)) by using the diffusion potentials, μ (defined in Eq. (1.43)), of nodes $i \pm 1$ and applying the central difference formula:

$$J_{i\pm1/2} = -M_{i\pm1/2}\frac{\mu_{i\pm1} - \mu_i}{\left|x_{i\pm1} - x_i\right|}, \tag{1.49}$$

where the coefficient $M_{i\pm1/2}$ denotes the mobility at the cell interface. In the present study, $M_{i\pm1/2}$ was simply set as

$$M_{i\pm1/2} = \frac{1}{2}\left(M_{i\pm1} + M_i\right). \tag{1.50}$$

When the mobility is constant and the grid spacing is uniform, Eq. (1.48) represents a discretized formula obtained using the finite-difference method with second order accuracy. Furthermore, the global conservation with respect to c is numerically guaranteed because the flux from one cell into the neighboring cell is exactly the negative of the flux from the neighbor into the first cell.

1.4 Research Objectives

This thesis describes the development of a numerical simulation technique for investigating two distinctive nanoscale to microscale phenomena. First, the fundamental effects of particle size, alloy composition, and heat-treatment temperature on the microstructure formation of Pt-based alloy nanoparticles were investigated. In this case, computational modeling studies are used as tools to explain the driving forces and predict the resultant surface structures. Next, the constitutive relationship between the Li conductivity and the quantitative microstructural features of a layered Li–transition-metal oxide, such as grain size, spatial distribution of the crystal orientation of each grain, and grain boundary (GB) diffusivity was investigated.

Atomistic simulations such as first-principles calculations, molecular dynamics, and Monte Carlo simulations have been regarded as powerful tools that can accurately probe the mechanism of microstructural formation from the view of atomic motion. However, in practical calculations, the system size will obviously be limited by its excessive computational cost on a much smaller scale than the nano–microscale phenomena. As an alternative approach, the phase-field method, which is described in section 1.3.1, is a possible numerical simulation technique for investigating mesoscale phenomena based on the formulation of free energy functions.

The objective of this work is to first construct an effective phase-field model to describe the compositional variation and phase transformation within a

single-alloy catalyst particle in PEFCs and provide information on the crucial aspects that affect the internal structure of a catalyst particle. In the case of alloy nanoparticle models, the free energy of the interface between the condensed phase and the gas phase was approximated by a regular solution of the atom–vacancy complex system. In the case of alloy nanoparticles, the free energy of the inner particle was defined assuming that the lattice points were occupied by the atomic component elements and vacancies. The energy function of the alloy nanoparticle was constructed to include the surface free energies of the alloy component elements and the thermodynamic assessments of the binary systems using the CALPHAD method. Therefore, it is possible to calculate the nanostructures in line with the specific material parameters.

The second objective of this work is to construct an effective phase-field model to describe the diffusion of Li in polycrystalline $LiCoO_2$ in LIBs. Information obtained from the model on the crucial aspects of anisotropic materials is then used to quantitatively understand their Li transport properties. In the case of the Li diffusion model, the energy function is constructed with the Gibbs free energy of the binary solution in the Li–vacancy system evaluated from the experimental or theoretical open-circuit potential of Li_xCoO_2 and the elastic strain energy associated with Li intercalation–deintercalation. To quantitatively predict the Li diffusivity, the models secure the formulation such that the material's kinetic parameters, including the Li diffusion process and electrochemical reaction of Li insertion, crystallographic misfit, and elastic constants obtained from theoretical calculations or from experiments as empirical data, can be introduced. Since observable phenomena represent the

consequences of a multi-step process, it is difficult to separately evaluate the role of each basic step. Therefore, an integrated computational approach that simultaneously simulates the microstructure and evaluates the transport properties presented is helpful in obtaining a quantitative understanding of each basic step of the Li transport process.

1.5 Outline of the Thesis

This thesis consists of six chapters including (1) Introduction, (2) Phase-Field Modeling of Phase Transformations in Fe–Pt Alloy Nanoparticles, (3) Surface Segregations in Platinum-Based Alloy Nanoparticles, (4) Numerical Study of Li Diffusion in Polycrystalline $LiCoO_2$, (5) Effect of Microstructure on the Discharge Properties of Polycrystalline $LiCoO_2$, and (6) Conclusions and Future Work. Since each chapter addresses different problems, every chapter includes an introductory section at its beginning.

Chapter 1 describes the general trends in high-performance batteries and challenges encountered in the development of electrode materials. The simulation methodology is then explained, followed by a brief discussion of the research objectives and the outline of the thesis.

Chapter 2 describes the fundamental formulation of a phase-field model constructed for describing the compositional variations and phase transformations within the Fe–Pt binary-alloy nanoparticles to understand the

effects of particle size and heat-treatment temperature on the microstructure formation.

In Chapter 3, the binary alloy model described in Chapter 2 is applied to Cr–Pt, Fe–Pt, Co–Pt, Ni–Pt, Cu–Pt, Pd–Pt, Ir–Pt, and Au–Pt binary-alloy nanoparticles. The overall picture of the compositional variation within a single particle with the alloy combinations, particle size, and heat-treatment temperature is elucidated. Moreover, based on the general tendencies for a binary system to exhibit segregation, control of the amount of platinum segregation on the surface using a ternary-alloy system is examined.

In Chapter 4, phase-field models are proposed to simulate the non-Fickian Li diffusion in 2D polycrystalline microstructures by considering the grain size, the spatial distribution of the crystal orientation in each grain, the crystallographic anisotropy of D_{self} of Li, and the Li diffusion along or across GBs modeled as a thin layer. The relationship between the apparent Li diffusivity and a 2D polycrystalline microstructure is discussed.

In Chapter 5, a method to treat the Li diffusion generated from the elastic stress field associated with Li concentration is proposed by solving the 2D inhomogeneous elastic equilibrium equations. Using this method, the effects of the elastic inhomogeneity on the apparent Li diffusivity of oriented single crystals and polycrystalline $LiCoO_2$ are investigated. Moreover, the effects of microstructure on the discharge properties of polycrystalline $LiCoO_2$ are clarified by simultaneously considering the microstructural factors investigated in Chapter 4 and the elastic stress field.

In Chapter 6, the key results obtained from the previous chapters are summarized. Further, future work that can be undertaken on the phase-field modeling of the microstructural evolution and properties is suggested.

Chapter 2
Phase-Field Modeling of Phase Transformations in Fe–Pt Alloy Nanoparticles

2.1 Introduction

To predict and design the surface structure of platinum-based alloy nanoparticles, various computational methodologies have been proposed, such as those based on the thermodynamic model [40], Monte Carlo simulation model with embedded-atom method (EAM) potential [41–49], and first-principles methods [9]. It appears that a thermodynamic method based on the knowledge of bulk thermodynamic parameters rather than nanoscale parameters is useful for understanding general trends in surface segregation, which occurs in many alloy systems. A previously proposed thermodynamic method estimates surface atomic fractions using vaporization enthalpies of pure elements and alloy solution activity coefficients [40]. Additionally, the dependence of surface composition on alloy particle size has been discussed. However, the combined effect of particle size and phase transformations on the degree of surface segregation has not been well understood.

The phase-field method [50] has been increasingly used as a numerical simulation method for predicting nanoscale phenomena. This method was applied for investigating the particle-size dependence in the ordering of FePt nanoparticles [51,52]. The results clearly showed that the disordered phase

induced by FePt particle surfaces becomes dominant as particle size decreases. Using the phase-field model to simulate the temporal evolution of the platinum density profile, it successfully represented the formation of platinum nanoparticles on a carbon substrate [53]. These application results support the use of the phase-field model to describe systems in thermodynamic equilibrium when the surface-area-to-volume ratio is high. This chapter focuses on the description of surface segregation by considering the phase transformations of internal particles. Recent progress in the methodology of the phase-field technique allows for simultaneous evaluation of the conservative temporal evolution of atomic concentration and non-conservative temporal evolution of phase transformations using the solutions of the Cahn–Hilliard [31] and Allen–Cahn [32] equations, respectively.

In this chapter, a phase-field model that describes atomic concentration and phase transformations inside platinum-based alloy nanoparticles is proposed for revealing the effects of particle size, alloy composition, and heat-treatment temperature on microstructure formation. To verify the accuracy of this simulation, the model was compared with experimental and other simulation results for the compositional variations and phase transformations in FePt nanoparticles.

2.2 Methods of Calculation

The phase-field model was developed to describe the radial distributions of the ordered–disordered phase, solid–liquid phase, and the atomic concentration of a single-alloy nanoparticle. Their temporal evolutions were calculated using the Cahn–Hilliard and Allen–Cahn equations on the basis of the free-energy function associated with an alloy's thermodynamics and surface free energy, including the effects of phase transformations. Formulations and implementations of the simulation method are described herein.

2.2.1 Formulation

Three types of field variables related to the atomic concentration, c, long-range crystallographic ordering, s, and phase transition, θ, between solid and liquid were introduced. A condensed-matter phase is distinguished from a surrounding vapor phase by the vacancy concentration. The temporal evolution of the radial distribution of each atomic concentration within a nanoparticle was calculated using the ternary Cahn–Hilliard equation [54,55], as expressed in the following conservative form:

$$\frac{\partial c_i}{\partial t} = \nabla \cdot \left[M_{ii} \nabla \left(\frac{\delta G_{\text{sys}}}{\delta c_i} \right) - M_{ij} \nabla \left(\frac{\delta G_{\text{sys}}}{\delta c_j} \right) \right]; \; i = \text{Pt, TM}; \; j = \text{Pt, TM}; \; i \neq j, \tag{2.1}$$

$$c_{\text{Pt}} + c_{\text{TM}} + c_{\text{Va}} = 1, \tag{2.2}$$

where c_i is the local atomic concentration of component i as a function of the

radial coordinate, r, and the time variable, t, and its value is normalized with respect to the maximum concentration so that it is a dimensionless value between 0 and 1. The subscripts TM and Va indicate the concentrations represent those of transition-metal element alloyed with platinum and the vacancy, respectively; in this chapter, TM corresponds to Fe, and M_{ii} is the mobility of component i owing to the gradient of the functional derivative of G_{sys} with respect to the concentration of component i. The coefficients M_{ii} and M_{ij} are expressed as $M_{ii} = c_i(1 - c_i)D / RT$ and $M_{ij} = c_i c_j D / RT$, respectively, when all species have the same diffusion coefficient, D [55]. Here, R and T are the gas constant and absolute temperature, respectively.

The equilibrium radial distributions of the ordered–disordered phase and the solid–liquid phase within a nanoparticle were calculated using the Allen–Cahn equation [32], expressed in the following nonconservative form:

$$\frac{\partial s}{\partial t} = -L_s \frac{\delta G_{\mathrm{sys}}}{\delta s}, \tag{2.3}$$

$$\frac{\partial \theta}{\partial t} = -L_\theta \frac{\delta G_{\mathrm{sys}}}{\delta \theta}, \tag{2.4}$$

where s is defined as the long-range order (LRO) parameter so that s values of 0 and 1 correspond to the disordered and ordered phases, respectively; θ is defined as the phase-field parameter so that θ values of 0 and 1 correspond to the liquid and solid phases, respectively; and L_s and L_θ denote the mobility of the ordered–disordered and solid–liquid phase interfaces, respectively. As a consequence of temporal evolution, quasi-stationary microstructures corresponding to the minimum free energy were obtained.

The total free energy of the simulated system, G_{sys}, is defined as the volume integral of the local chemical free energy and the gradient energy term over the entire volume, V, as follows:

$$G_{\mathrm{sys}} = \frac{1}{V}\int_{\mathbf{r}} \{h(\theta) G_{\mathrm{chem}}^{(\mathrm{S})} + \left[1-h(\theta)\right] G_{\mathrm{chem}}^{(\mathrm{L})} + \frac{\kappa_{\mathrm{Pt-TM}}}{2}\left[\left(\nabla c_{\mathrm{Pt}}\right)^2 + \left(\nabla c_{\mathrm{TM}}\right)^2\right] + \frac{\kappa_{\mathrm{Va}}}{2}\left(\nabla c_{\mathrm{Va}}\right)^2 + h\left(c_{\mathrm{Pt+TM}}\right)\frac{\kappa_{\mathrm{s}}}{2}\left|\nabla s\right|^2 + W\theta\left(1-\theta\right) + \frac{\kappa_{\theta}}{2}\left(\nabla\theta\right)^2\} \mathrm{d}\mathbf{r}; \quad (2.5)$$

$$h(x) = x^3\left(6x^2 - 15x - 10\right); \;\; x \;=\; \theta,\;\; c_{\mathrm{Pt+TM}}; \quad (2.6)$$

$$c_{\mathrm{Pt+TM}} = c_{\mathrm{Pt}} + c_{\mathrm{TM}}; \quad (2.7)$$

$$W = \left(c_{\mathrm{Pt}} W_{\mathrm{Pt}} + c_{\mathrm{TM}} W_{\mathrm{TM}}\right) / c_{\mathrm{Pt+TM}}; \quad (2.8)$$

$$\kappa_{\theta} = \left(c_{\mathrm{Pt}} \kappa_{\theta,\mathrm{Pt}} + c_{\mathrm{TM}} \kappa_{\theta,\mathrm{TM}}\right) / c_{\mathrm{Pt+TM}}. \quad (2.9)$$

Because the spatial derivative terms multiplied by $\kappa_{\mathrm{Pt-TM}}$ are not zero when the spatial derivative term multiplied by κ_{Va} is not zero, κ_{Va} is represented by the subtraction of $\kappa_{\mathrm{Pt-TM}}$ from a linear combination of κ_{Pt} and κ_{TM}, as given in the following equations:

$$\kappa_{\mathrm{Va}} = \left[c_{\mathrm{Pt}}\left(\kappa_{\mathrm{Pt}} - \kappa_{\mathrm{Pt-TM}}\right) + c_{\mathrm{TM}}\left(\kappa_{\mathrm{TM}} - \kappa_{\mathrm{Pt-TM}}\right)\right] / c_{\mathrm{Pt+TM}}, \quad (2.10)$$

with

$$\kappa_i = h(\theta)\kappa_i^{(\mathrm{S})} + \left[1-h(\theta)\right]\kappa_i^{(\mathrm{L})}; \;\; i \;=\; \mathrm{Pt},\;\; \mathrm{TM}; \quad (2.11)$$

where $\kappa_i^{(\mathrm{S})}$ and $\kappa_i^{(\mathrm{L})}$ are the gradient energy coefficients of the solid–vapor and liquid–vapor interfaces, respectively, of atomic element i.

The terms $G_{\mathrm{chem}}^{(\mathrm{S})}$ and $G_{\mathrm{chem}}^{(\mathrm{L})}$ denote the changes in the chemical free energies between the solid and vapor phases and between the liquid and vapor phases, respectively. The chemical free energies were evaluated along with the approximation of the regular solution model expressed as follows:

$$G_{\text{chem}}^{(\text{S})} = c_{\text{Pt}}\,{}^{\circ}G_{\text{Pt}}^{(\text{S})} + c_{\text{TM}}\,{}^{\circ}G_{\text{TM}}^{(\text{S})} + L_{\text{Pt-Va}}^{(\text{S})} c_{\text{Pt}} c_{\text{Va}} + L_{\text{TM-Va}}^{(\text{S})} c_{\text{TM}} c_{\text{Va}} + L_{\text{Pt-TM}}^{(\text{S})} c_{\text{Pt}} c_{\text{TM}} + \Delta G_{\text{Pt-TM}}^{(\text{ord})} + RT\left(c_{\text{Pt}} \ln c_{\text{Pt}} + c_{\text{TM}} \ln c_{\text{TM}} + c_{\text{Va}} \ln c_{\text{Va}}\right), \tag{2.12}$$

$$G_{\text{chem}}^{(\text{L})} = c_{\text{Pt}}\,{}^{\circ}G_{\text{Pt}}^{(\text{L})} + c_{\text{TM}}\,{}^{\circ}G_{\text{TM}}^{(\text{L})} + L_{\text{Pt-Va}}^{(\text{L})} c_{\text{Pt}} c_{\text{Va}} + L_{\text{TM-Va}}^{(\text{L})} c_{\text{TM}} c_{\text{Va}} + L_{\text{Pt-TM}}^{(\text{L})} c_{\text{Pt}} c_{\text{TM}} + RT\left(c_{\text{Pt}} \ln c_{\text{Pt}} + c_{\text{TM}} \ln c_{\text{TM}} + c_{\text{Va}} \ln c_{\text{Va}}\right), \tag{2.13}$$

where the superscripts (S) and (L) indicate the solid and liquid phases, respectively; and ${}^{\circ}G_i^{(j)}$ is the Gibbs formation energy of pure element *i* in phase *j*, obtained from data of the Scientific Group Thermodata Europe (SGTE) [56]. When these formulations are applied to a pure material, Eqs. (2.12) and (2.13) result in expressions similar to those reported in Ref. [57], which were applied to the sintering of two spherical pure-element particles. The energy difference between the ordered and disordered phases, $\Delta G_{\text{Pt-Fe}}^{(\text{ord})}$, is defined by the site fraction of component *i* on sublattice *j*, $y_i^{(j)}$ [58]. To reduce the number of field variables, a three-component LRO parameter, **S** [59], which is defined as follows, was adopted:

$$\mathbf{S} = \begin{pmatrix} s_1 \\ s_2 \\ s_3 \end{pmatrix} = \frac{1}{2}\begin{pmatrix} s_{1,\text{Pt}} - s_{1,\text{Fe}} \\ s_{2,\text{Pt}} - s_{2,\text{Fe}} \\ s_{3,\text{Pt}} - s_{3,\text{Fe}} \end{pmatrix}, \tag{2.14}$$

with

$$\mathbf{S}_i = \begin{pmatrix} s_{1,i} \\ s_{2,i} \\ s_{3,i} \end{pmatrix} = \frac{1}{2}\begin{pmatrix} y_i^{(1)} + y_i^{(2)} - y_i^{(3)} - y_i^{(4)} \\ y_i^{(1)} - y_i^{(2)} - y_i^{(3)} + y_i^{(4)} \\ y_i^{(1)} - y_i^{(2)} + y_i^{(3)} - y_i^{(4)} \end{pmatrix}; \quad i = \text{Pt, Fe.} \tag{2.15}$$

Here, the $y_i^{(j)}$ values are obtained uniquely using $\mathbf{S}_i$ and c_i values. The parameter $\mathbf{S} = (s_1, s_2, s_3)$ has the values of (±1, 0, 0), (0, ±1, 0), and (0, 0, ±1) for the complete $L1_0$ and $L1_1$ ordered phases, and (±0.5, ±0.5, ±0.5) for the

complete $L1_2$ ordered phase. The coefficient $L_{i-\mathrm{Va}}^{(j)}$ is a pair-wise interaction parameter between alloy element *i* and a vacancy, and it is defined as follows:

$$L_{i-\mathrm{Va}}^{(j)} = \Delta H_{\mathrm{f},i}^{(j)} - T\Delta S_{\mathrm{f}};\ j = \mathrm{S},\ \mathrm{L}; \tag{2.16}$$

where $\Delta H_{\mathrm{f},i}^{(j)}$ and ΔS_{f} are the enthalpy and entropy of mono-vacancy formation, respectively. The terms $L_{\mathrm{Pt-Fe}}^{(\mathrm{S})}$ and $L_{\mathrm{Pt-Fe}}^{(\mathrm{L})}$ were provided as polynomial equations with respect to the atomic concentrations based on the thermodynamic assessments of the Fe–Pt [58] binary systems using the CALPHAD method. The Fe–Pt system has the ordered phase in the temperature–concentration phase diagram for the bulk material. Therefore, $L_{\mathrm{Pt-Fe}}^{(\mathrm{S})}$ and $L_{\mathrm{Pt-Fe}}^{(\mathrm{L})}$ had negative values. In addition, it may be claimed that the volume in one nanoparticle is too small for an assessment of the macroscopic thermodynamic equilibrium state. It may be presumed that these calculation results using the CALPHAD data could be treated as an average state corresponding to a long timescale or ensemble averages of two or more particles with the same particle diameter.

2.2.2 Physical Constants and Parameters

The surface energy of the condensed-matter–vapor interface corresponds to a summation of the excess free energy in the diffusive transition region from very low to very high vacancy concentration, which depends on the alloy components. In the case of the condensed-matter–vapor interface with a one-dimensional gradient, the following relationship exists among the surface energy, $\gamma_i^{(j)}$, interfacial thickness, $\Delta d_i^{(j)}$, and gradient energy coefficient, $\kappa_i^{(j)}$,

in accordance with the derivations described in Sec. 1.3.1.2:

$$\gamma_i^{(j)} = \frac{\sqrt{\kappa_i^{(j)}}}{V_{\mathrm{m},i}^{(j)}} \int_{c_\mathrm{v}\approx 0}^{c_\mathrm{c}\approx 1} \sqrt{2\Delta G(c)}\,\mathrm{d}c, \tag{2.17}$$

$$\Delta d_i^{(j)} = (c_\mathrm{c} - c_\mathrm{v}) \sqrt{\frac{\kappa_i^{(j)}}{2\Delta G(c=0.5)}}, \tag{2.18}$$

where the subscript i indicates the alloy component (Pt or Fe); c_c and c_v are the atomic concentrations of the condensed and vapor phases, respectively; $V_{\mathrm{m},i}^{(j)}$ is the molar volume; and ΔG is the free-energy change across the interface, which correlates with $L_{i-\mathrm{Va}}^{(j)}$. In these calculations, $L_{i-\mathrm{Va}}^{(\mathrm{S})}$ and $\kappa_i^{(\mathrm{S})}$ were determined to reproduce the $\gamma_i^{(\mathrm{S})}$ and $\Delta d_i^{(\mathrm{S})}$ values. The $\Delta d_i^{(\mathrm{S})}$ value for the solid phase was set at 3.0×10^{-10} m by adjusting the mono-vacancy formation energy, $\Delta H_{\mathrm{f},i}^{(\mathrm{S})}$, which led to a change in the $L_{i-\mathrm{Va}}^{(\mathrm{S})}$ values. Here, the values obtained for the solid surface energy, $\gamma_i^{(\mathrm{S})}$, of the (111) surfaces of Pt and Fe from first-principles calculations [60] were employed. Table 2.1 shows the surface energy including the temperature correction. The temperature correction was made using the following equation [61]:

$$\gamma_i^{(\mathrm{S})}(T) = \gamma_i^{(\mathrm{S})}(0) - RT / A, \tag{2.19}$$

where A is the surface area per mole of surface atoms, as defined by [61]

$$A = 1.612 N^{1/3} V^{2/3}, \tag{2.20}$$

where N is Avogadro's number and V is the molar volume. The liquid surface energy, $\gamma_i^{(\mathrm{L})}$, was estimated from $\gamma_i^{(\mathrm{L})} = \gamma_i^{(\mathrm{S})} / 1.18$ [61]. For representation of the differences in the bond strengths in solids and liquids, $\Delta H_{\mathrm{f},i}^{(\mathrm{L})}$ was assumed to be a relative value of $\Delta H_{\mathrm{f},i}^{(\mathrm{S})}$, as defined by the equation

$$\Delta H_{\mathrm{f},i}^{(\mathrm{L})} = \frac{\Delta H_{\mathrm{v},i}}{\Delta H_{\mathrm{m},i} + \Delta H_{\mathrm{v},i}} \Delta H_{\mathrm{f},i}^{(\mathrm{S})}, \tag{2.21}$$

where $\Delta H_{\mathrm{m},i}$ is the heat of fusion and $\Delta H_{\mathrm{v},i}$ is the heat of vaporization. As the surface energy is considered to be associated with $\Delta H_{\mathrm{f}} / A$, $\gamma_i^{(\mathrm{S})} / \gamma_i^{(\mathrm{L})}$ is rewritten as $\left(\Delta H_{\mathrm{f},i}^{(\mathrm{S})} / \Delta H_{\mathrm{f},i}^{(\mathrm{L})}\right) \times \left(A^{(\mathrm{L})} / A^{(\mathrm{S})}\right)$. In the case of platinum, $\Delta H_{\mathrm{f,Pt}}^{(\mathrm{S})} / \Delta H_{\mathrm{f,Pt}}^{(\mathrm{L})}$ was calculated to be about 1.04 (from Eq. (2.21)), and $A^{(\mathrm{L})} / A^{(\mathrm{S})}$ was about 1.07 (from Eq. (2.20)). Therefore, $\left(\Delta H_{\mathrm{f,Pt}}^{(\mathrm{S})} / \Delta H_{\mathrm{f,Pt}}^{(\mathrm{L})}\right) \times \left(A^{(\mathrm{L})} / A^{(\mathrm{S})}\right)$ was about 1.11. The derived value was approximately equal to the abovementioned value of 1.18 obtained from $\gamma_i^{(\mathrm{L})} = \gamma_i^{(\mathrm{S})} / 1.18$. Therefore, it is suggested that the assumption of Eq. (2.21) is physically relevant. The $\kappa_i^{(\mathrm{L})}$ value was then determined to reproduce the $\gamma_i^{(\mathrm{L})}$ and $\Delta H_{\mathrm{f},i}^{(\mathrm{L})}$ values. The ΔS_{f} value in Eq. (2.16) approximately adopted a formulation of $1.32R$, which was originally used for platinum [62]. The estimated $\Delta H_{\mathrm{f},i}^{(\mathrm{S})}$, $\kappa_i^{(\mathrm{S})}$, and $\kappa_i^{(\mathrm{L})}$ values at 973.15 K (a typical annealing temperature for the synthesis of nanoparticles) are listed in Table 2.1. The estimated $\Delta H_{\mathrm{f},i}^{(\mathrm{S})}$ values in Table 2.1 are in fairly good agreement with the experimental values [63].

In the case of the solid–liquid interface, the values of the interfacial energy barrier, W_i, and $\kappa_{\theta,i}$ were determined by introducing the values obtained for $\gamma_i^{(\mathrm{S-L})} \left(= \gamma_i^{(\mathrm{S})} - \gamma_i^{(\mathrm{L})}\right)$ and the width of the solid–liquid interface $\Delta d_i^{(\mathrm{S-L})}$ (which was assumed to be approximately equal to that of the solid–vapor interface) into the following equations:

$$\gamma_i^{(\mathrm{S-L})} = \sqrt{\kappa_{\theta,i}} \int_0^1 \frac{\sqrt{2W_i}}{V_i^{(\mathrm{S-L})}} \mathrm{d}\theta, \tag{2.22}$$

$$\Delta d_i^{(\mathrm{S-L})} = \sqrt{\frac{\kappa_{\theta,i}}{2W_i}}, \tag{2.23}$$

where $V_i^{(\mathrm{S-L})}$ is introduced as

$$V_i^{(\mathrm{S-L})} = h(\theta)V_i^{(\mathrm{S})} + \left[1 - h(\theta)\right]V_i^{(\mathrm{L})}. \tag{2.24}$$

Equation (2.18) is modified slightly to the following expression [35] for the estimation of the κ_s value for the ordered–disordered phase interface:

$$\Delta x = 2\sqrt{\frac{\kappa_s}{2\Delta G(s=0)}}, \tag{2.25}$$

where Δx is the width of the anti-phase boundary (APB), and $\Delta G(s = 0)$ corresponds to the absolute value of $\Delta G_{\mathrm{Pt-Fe}}^{(\mathrm{ord})}$. For the reproduction of the experimental results shown in Fig. 2.1, a Δx value of 1.0×10^{-9} m was used, which was close to the experimentally observed value of approximately 1.38×10^{-9} m for FePt [64]. The values of κ_s at 973.15 K were 1.63×10^{-15} J·m^2·mol^{-1} for $L1_0$.

The value of $\kappa_{\mathrm{Pt-Fe}}$ was defined as having a negative sign according to Eq. (2.17). However, a negative $\kappa_{\mathrm{Pt-Fe}}$ value may induce instability during the numerical simulation. It is confirmed that when $\kappa_{\mathrm{Pt-Fe}}$ is set to a positive value of the order of about 10^{-17}, such instability is avoided, and the value has a minor effect on the final concentration profile. In this study, the $\kappa_{\mathrm{Pt-Fe}}$ value for the Fe–Pt system was set at 5×10^{-17} J·m^2·mol^{-1}.

Table 2.1. Estimated parameters of the alloy elements at 973.15 K.

Atomic element	Fe	Pt
Surface Energy, $\gamma_i^{(S)}$/J·m^{-2}	2.05	1.35
Molar volume,		
$V_{m,i}^{(S)}/10^{-6}$ m^3·mol^{-1}	7.28	9.15
$V_{m,i}^{(L)}/10^{-6}$ m^3·mol^{-1}	7.83	10.1
Mono-vacancy formation energy, $\Delta H_{f,i}^{(S)}$/96485 J·mol^{-1}	1.65 *1.54*[a]	1.42 *1.32*[a], *1.35*[a]
Gradient energy coefficient,		
$\kappa_i^{(S)}/10^{-15}$ J·m^2·mol^{-1}	5.81	4.92
$\kappa_i^{(L)}/10^{-15}$ J·m^2·mol^{-1}	5.08	4.57
$\kappa_{\theta,i}/10^{-15}$ J·m^2·mol^{-1}	0.947	0.804
Solid–liquid interface energy, W_i /kJ·mol^{-1}	19.0	16.0

[a] Reference [63].

2.2.3 Numerical Calculation

The numerical calculation of the one-dimensional problem along the radial direction of a nanoparticle was performed using the finite-volume method with the explicit Euler method. In the present calculation, the isotropic surface energy of a nanoparticle was assumed. The simulation was executed mainly at a temperature of 973.15 K, with an initial grid spacing of 0.005 nm. Changes in the local molar volume, depending on the changes in atomic concentrations and phase transformations, were taken into account to ensure mass conservation. Therefore, the grid spacing at each grid point was updated for each time step. The initial simulation size, l, was defined as the particle radius plus 0.75 nm,

and the boundary conditions at $r = 0$ and $r = l$ were chosen such that the spatial derivatives of the field variables were zero. In the external region of the particle, only vaporized atomic elements were present, *i.e.*, it was an inert atmosphere. The initial concentration of platinum was equal to that of the alloying element combined with platinum, the initial θ value was equal to the $c_{\mathrm{Pt+Fe}}$ value, the initial s values in Eq. (2.15) were set as $(s_{1,\mathrm{Pt}}, s_{2,\mathrm{Pt}}, s_{3,\mathrm{Pt}}) = (c_{\mathrm{Pt+Fe}}, 0, 0)$, and $\mathbf{S}_{\mathrm{Fe}} = -\mathbf{S}_{\mathrm{Pt}}$ was assumed for all positions. The variable $\mathbf{S}_{\mathrm{Pt}}$ is denoted as the variable $\mathbf{S}$ in Sec. 2.3, the representative variable for estimating the degree of $\mathrm{L1_0}$ or $\mathrm{L1_1}$ ordering. In this simulation study, we focused on obtaining the steady-state microstructure. Therefore, the simulated time step was varied according to the flux of atomic concentration to reduce the simulation time. The mobility values of L_s and L_θ in Eqs. (2.3) and (2.4) were set to be larger than the atomic concentration change so that the rate of atomic diffusion was not limited by the mobility of the solid–liquid and ordered–disordered phase interfaces.

2.3 Results and Discussion

The results of the practical applications of the developed method are explained here. First, to verify the accuracy of this simulation, the results of the phase transformations and compositional variations in FePt nanoparticles with diameters of less than 10 nm were compared with those of experiments and other simulations.

2.3.1 Phase Transformations

To verify the accuracy of this phase-field model, the simulated results were compared with experimental and other simulation results. Figure 2.1 shows the experimentally observed particle-size dependence of the $L1_0$ ordering in FePt particles that were fabricated or annealed at 973.15 K [65–67]. The degree of $L1_0$ ordering decreased as the particle size decreased. When the APB width was assumed to be 1.0 nm, in accordance with the experimental results described in Sec. 2.2, the calculated *s* values were in good agreement with the experimental results. This implies that the present phase-field model is sufficiently accurate to describe the order–disorder phase transition within a nanoparticle. Figure 2.2 shows the temperature dependence of the $L1_0$ ordering of FePt particles with diameters of 4 nm. The order–disorder phase-transition temperature decreased as the particle size decreased. This figure also shows previously reported results from Monte Carlo simulations [43]. At first glance, the present model reproduced the general trend of the temperature dependence seen from the Monte Carlo simulations, although the simulated phase-transition temperature was slightly below that obtained from the Monte Carlo simulations. In the present simulation, the ordered–disordered phase interface had a finite width inside a particle. Therefore, the disordered phase was dominant at the particle surface. On the other hand, it is well known that the surface state from the Monte Carlo simulation result is affected significantly by the adopted surface potential [44]. In short, there is no conclusive evidence of any method providing more accurate results than others.

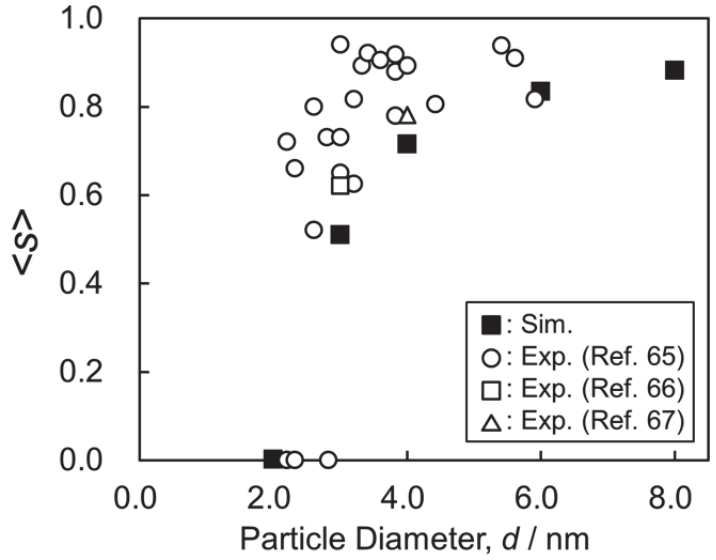

Fig. 2.1. Comparison of the dependence of $L1_0$ ordering of the FePt particles on particle size with experimental results.

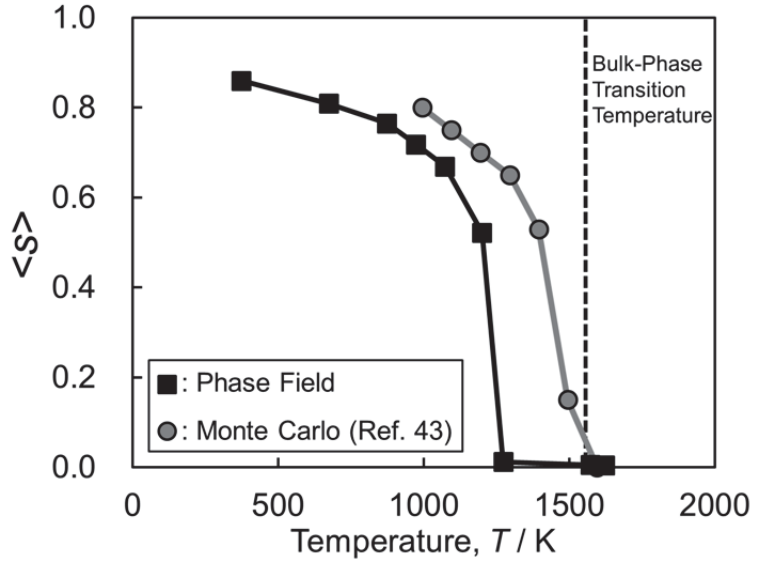

Fig. 2.2. Comparison of dependence of the $L1_0$ ordering of the FePt particles on temperature with the results of Monte Carlo simulation. The particle diameter was 4 nm.

Another important feature was the particle-size dependence of the solid–liquid transition temperature. Figure 2.3 shows the equilibrium phase of the FePt nanoparticle versus the holding temperature and the particle size. When the particle diameter was on the nanometer scale, the influence of the surface tension of the particle on its chemical potential was significant. The difference in surface tension between the solid and liquid phases also led to a difference in the equilibrium vapor pressures of those phases. Generally, the surface tension of the liquid phase is smaller than that of the solid phase, and the liquid phase is formed at a temperature lower than the melting point of the bulk to decrease the free energy. Furthermore, at temperatures lower than the complete melting temperature of the nanoparticles, it is known that a kind of core–shell structure

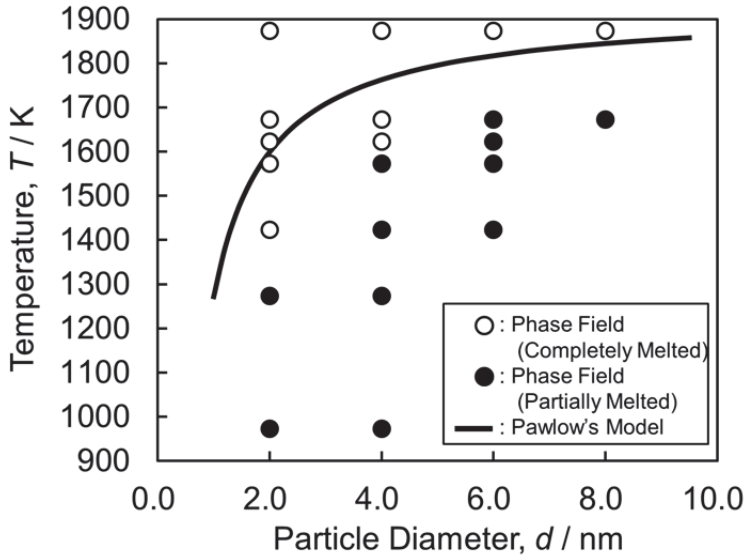

Fig. 2.3. Phases of the FePt particles calculated with respect to the particle size (circles) compared to the phase boundaries predicted by Pawlow's model (solid line).

is formed in the particle only through melting of the particle surface, which is known as surface pre-melting [68]. In this figure, the open circles denote completely melted particles and filled circles denote partially melted particles. The simulated transition temperature of the solid–liquid phases corresponded to the interface of these circles. The temperature dependence was more remarkable in particles of less than 10 nm in diameter. Figure 2.3 also shows the theoretical prediction from Pawlow's model, which yields the following equation [69]:

$$T_{\mathrm{m}} = T_{\mathrm{m}}^{\mathrm{Bulk}} \left\{ 1 - \frac{2\sigma_{\mathrm{s}} v_{\mathrm{s}}}{\Delta H_{\mathrm{m}} r_{\mathrm{s}}} \left[1 - \frac{\sigma_{\mathrm{l}}}{\sigma_{\mathrm{s}}} \left(\frac{v_{\mathrm{l}}}{v_{\mathrm{s}}} \right)^{2/3} \right] \right\}. \tag{2.26}$$

In Eq. (2.26), the relationship between the melting temperature, T_{m}, and the particle radius, r_{s}, is estimated on the basis of the equilibrium between solid and liquid particles. Each parameter in Eq. (2.26) is defined as the mean of the physical constants of Pt and Fe: $T_{\mathrm{m}}^{\mathrm{Bulk}}$ is 1926.6 K; the molar heat of fusion, ΔH_{m}, is 16.4 kJ·mol^{-1}; the molar volumes of the solid, v_{s}, and liquid, v_{l}, are 8.10 × 10^{-6} and 8.97 × 10^{-6} m^3·mol^{-1}, respectively; and the surface tensions of the solid, σ_{s}, and liquid, σ_{l}, are 1.85 and 1.57 J·m^{-1}, respectively. The simulated phase boundary between the solid and liquid phases was slightly below that obtained with Pawlow's model. It was postulated that this subtle but meaningful difference was due to surface pre-melting [70]. The surface layers of the FePt particles were partially in the liquid phase, as described in the next section. This layer was expected to induce the more significant melting-temperature dependence on the particle size, as shown in Fig. 2.3.

2.3.2 Surface Segregation

Figure 2.4 shows the radial distributions of the atomic concentrations (c_{Pt}, c_{Fe}, and c_{Pt+Fe}), values of $|\mathbf{S}| \times c_{Pt+Fe}$ of the ordered–disordered phase, and values of θ of the solid–liquid phase of nanoparticles with diameters of 2 and 4 nm at 973.15 K. The region in which the value of c_{Pt+Fe} changes from 0 to 1 corresponds to the particle surface. The change in the black line corresponding to the fraction of the solid phase from 0 to 1 inside the particle implies that surface pre-melting occurred. As the particle size decreased, the stable phase inside the particle changed from an ordered phase to a disordered phase. In addition, this simulation also evaluated the atomic concentrations of the alloying elements. As seen in Fig. 2.4 (a), the FePt particles did not show significant concentration decomposition because the strong attractive interaction energy between Fe and Pt overcame the differences in surface energy. Monte Carlo simulations with the cluster expansion fitted to *ab initio* data [44] indicated that FePt did not exhibit significant segregation, and an increase in Pt concentration in the outermost surface was compensated by a decrease in Pt concentration in the sub-surface. The results shown in Fig. 2.4 (a) are consistent with those obtained from the simulation reported in Ref. [44].

Figure 2.4 (b) shows the results for the $FePt_3$ nanoparticle, where the $|\mathbf{S}|$ value of 0.866 corresponds to the $L1_2$ phase. The simulation predicted that Pt shells formed on the surface layers (indicated by gray arrows), and the $L1_2$ phase existed stably in this particle. As explained in the next chapter, the structure of Fe–Pt particle was similar to that of Co–Pt particle. The $FePt_3$ particle showed

that its core–shell structure was similar to the experimental observed structure of the $CoPt_3$ particle [71], although the structure of the $FePt_3$ particle has not been studied experimentally.

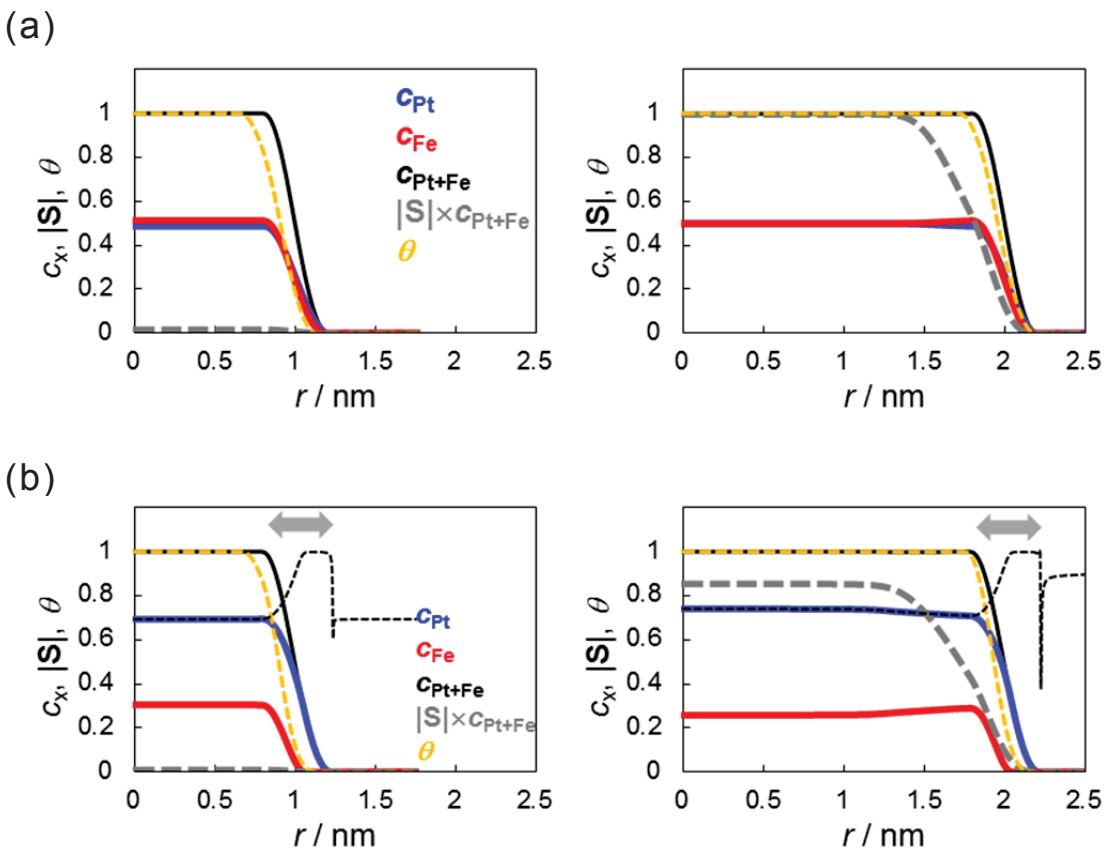

Fig. 2.4. Radial distribution of the mole fraction of each atom, c_x, the long-range ordering parameter, $|\mathbf{S}|$, and the solid–liquid phase transition parameter, θ, within (a) FePt and (b) $FePt_3$ nanoparticles with diameters of (left column) 2 nm and (right column) 4 nm at 973.15 K. The horizontal axis denotes the distance from the particle center. The $|\mathbf{S}|$ value of 0 corresponds to the disordered phase. The $|\mathbf{S}|$ values of 1 and 0.866 correspond to the $L1_0$ phase in (a) and the $L1_2$ phase in (b), respectively. The dashed black lines in (b) show the values of c_{Pt}/c_{Pt+Fe}.

2.4 Summary

Phase-field simulations were performed to investigate phase transformations and surface segregation in the Fe–Pt binary-alloy nanoparticles. The phase-field model based on an alloy's thermodynamic and surface free energy was developed to describe the radial distributions of the ordered–disordered phase, solid–liquid phase, and the alloy composition of a single-alloy nanoparticle.

From the results, it was evident that surface segregation, atomic ordering, and solid–liquid phase transition are sensitive to the alloy components and particle size. The degree of $L1_0$ ordering decreased with a decrease in the particle size. The calculated gradations were in good agreement with the experimental results. The simulated phase boundary between the solid and liquid phases was slightly below that obtained with the classical model because of surface premelting, which is not considered in the classical model. In addition, FePt exhibited hardly any significant segregation, and an increase in the Pt concentration in the outermost surface was compensated by a decrease in the concentration in the sub-surface. The results were consistent with those obtained by previously reported Monte Carlo simulations.

Although the surface energy was accounted for through parameter values related to a flat plane surface, the proposed phase-field approach provides a sufficiently accurate description of the internal structure of a single nanoparticle.

Chapter 3
Surface Segregations in Platinum-Based Alloy Nanoparticles

3.1 Introduction

In the previous chapter, the phase-field method is proposed for describing the internal structure of a single Fe–Pt nanoparticle. It is based on the thermodynamic theory of alloys and the surface free energy, which simultaneously calculates the atomic segregation and phase transformations within single platinum-based alloy nanoparticles. According to thermodynamics theory, the steady state of the atomic distribution and phase parameter corresponds to the state with minimum free energy. This phase-field method has sufficient accuracy to evaluate the effects of the particle size, alloy composition, and heat-treatment temperature on the ordered–disordered and solid–liquid phase transitions. Thus it can be used to describe the atomic surface segregation in Pt-based binary-alloy nanoparticles.

The objective of the present chapter is to first examine the surface compositions resulting from the balance between the surface and the chemical interaction among atomic components for various alloy combinations. Second, with these results, a general scheme of the binary-alloy system to obtain a thinly coated Pt surface structure in a nanoparticle is derived. Finally, applications of this method to a ternary-alloy system are presented.

3.2 Surface Segregation of Binary Nanoparticles

To obtain the general attributes of the abovementioned relationship, the radial distribution of the phase state and the atomic compositions of CrPt, FePt, CoPt, NiPt, CuPt, PdPt, IrPt, and AuPt nanoparticles with diameters below 10 nm at 973 K were investigated. In addition, the validity of the simulation results were examined through comparisons with previously reported Monte Carlo simulations.

3.2.1 Computational Details

A one-dimensional calculation along the particle radial coordinates was used to evaluate the distribution of the alloy composition and the ordered–disordered phase from the center to the surface of a single spherical particle. Detailed explanations of the numerical calculation scheme for a binary-alloy nanoparticle utilizing the phase-field method are presented in the previous chapter.

The coefficients $L^{(S)}_{Pt-TM}$ and $L^{(L)}_{Pt-TM}$, as well as $\Delta G^{(ord)}_{Pt-TM}$ (TM = Cr, Fe, Co, Ni, Cu, Pd, Ir, or Au) shown in Eqs. (2.12) and (2.13), are provided as polynomial equations with respect to the atomic concentrations based on the thermodynamic assessments of the Cr–Pt [72], Fe–Pt [58], Co–Pt [73], Ni–Pt [74], Cu–Pt [75], Pd–Pt [76], Ir–Pt [77], and Au–Pt [78] binary systems using CALPHAD. The coefficients $\Delta H_{f,i}$, $\kappa_i^{(S)}$, and $\kappa_i^{(L)}$ (i = Pt, TM) used in Eqs. (2.17) and (2.18) are calculated simultaneously based on the (111) surface energy of the fcc structure

of the pure metal element [60,79] and assuming a solid–vapor interface width of 3×10^{-10} m. Here, the values used for the solid surface energy, $\gamma_i^{(S)}$, of the (111) surfaces of Pt, Fe, and Co were obtained from first-principles calculations [60], and the values of $\gamma_i^{(S)}$ for Ni, Cu, Pd, Ir, and Au were evaluated from embedded-atom calculations [79]. Since there is a discrepancy between the Pt surface energies in Refs. [60] and [79], the values in Ref. [79] were scaled to fit the Pt value in Ref. [79] to the Pt value in Ref. [60]. The surface energy of fcc-Cr was estimated based on the relative value of γ-Fe and α-Fe in Ref. [60] and the relative value of bcc-Cr and α-Fe in Ref. [80].

In the case of a solid–liquid interface, the values of the interfacial energy barrier W_i, and $\kappa_{\theta,i}$ were determined by introducing the solid–liquid interfacial energy and the width of the solid–liquid interface, as described by Eqs. (2.22) and (2.23) in Sec. 2.2.2. The evaluated values are listed in Table 3.1. The estimated $\Delta H_{f,i}^{(S)}$ values in Table 3.1 are in fairly good agreement with the experimental values [63,81,82].

The gradient energy coefficient, κ_s, represents the gradient energy coefficient with respect to the ordered–disordered phase interface. Using $\Delta G_{Pt-TM}^{(ord)}$ and assuming an anti-phase boundary width of 1×10^{-9} m, the values of κ_s for CrPt ($L1_0$), FePt ($L1_0$), CoPt ($L1_0$), and CuPt ($L1_1$) were found to be 0.303 $\times 10^{-15}$, 1.63×10^{-15}, 0.160×10^{-15}, and 0.137×10^{-15} J·m^2·mol^{-1}, respectively.

The variable κ_{Pt-TM} represents a significant value in binary systems such as Ir–Pt and Au–Pt with a miscibility gap. Using the interfacial energy heights estimated from the CALPHAD data and assuming an interface width of 1×10^{-9} m, the values of $\kappa_{Pt\text{-}TM}$ for the Ir–Pt and Au–Pt binary systems were determined

to be 1.66×10^{-15} and 1.67×10^{-15} J·m^2·mol^{-1}, respectively. The $\kappa_{\mathrm{Pt-TM}}$ values for the other binary systems examined in the present computational study were set at 5×10^{-17} J·m^2·mol^{-1} in the same manner described in Sec. 2.2.2.

Table 3.1. Estimated parameters of the alloy elements at 973.15 K.

Atomic element	Cr	Fe	Co	Ni	Cu	Pd	Ir	Pt	Au
Surface energy, $\gamma_i^{(S)}$/J·m^{-2}	2.62	2.05	1.88	1.66	1.11	1.11	2.41	1.35	0.67
Molar volume,									
$V_{m,i}^{(S)}/10^{-6}$ m^3·mol^{-1}	6.60	7.28	6.76	6.65	7.20	8.94	8.62	9.15	10.3
$V_{m,i}^{(L)}/10^{-6}$ m^3·mol^{-1}	8.20	7.83	7.51	7.34	7.88	10.0	9.46	10.1	11.3
Mono-vacancy formation energy, $\Delta H_{f,i}^{(S)}$/96485 J·mol^{-1}	1.85 *2.0*[a]	1.65 *1.54*[a]	1.45 *1.34*[a]	1.31 *1.78*[a] *1.80*[c]	1.05 *1.28*[a] *1.48*[a]	1.22 *1.85*[a] *1.54*[c]	2.15 *1.97*[b] *2.24*[c]	1.42 *1.32*[a] *1.35*[a] *1.50*[c]	0.96 *0.89*[a] *0.97*[c]
Gradient energy coefficient,									
$\kappa_i^{(S)}/10^{-15}$ J·m^2·mol^{-1}	6.76	5.81	5.03	4.38	2.89	3.86	8.15	4.92	2.74
$\kappa_i^{(L)}/10^{-15}$ J·m^2·mol^{-1}	7.87	5.08	4.72	4.08	2.65	3.72	7.45	4.57	2.50
$\kappa_{\theta,i}/10^{-15}$ J·m^2·mol^{-1}	1.13	0.947	0.797	0.681	0.439	0.636	1.33	0.804	0.426
Solid–liquid interface energy, W_i /kJ·mol^{-1}	25.0	19.0	17.0	15.0	11.0	13.0	27.0	16.0	9.3

[a] Reference [63].
[b] Reference [81].
[c] Reference [82].

3.2.2 Results and Discussion

Figure 3.1 shows the radial distributions of the atomic concentrations (c_{Pt}, c_{TM}, and c_{Pt+TM}), values of $|\mathbf{S}| \times c_{Pt+TM}$ of the ordered–disordered phase, and the values of θ of the solid–liquid phase of nanoparticles with diameters of 2, 4, and 6 nm at 973.15 K. The compositional ratio of Pt to the alloyed metal element was 1:1. The region where the summation of the concentration of the component elements, excluding the vacancy (indicated by the black solid line), varies from 0 to 1 corresponds to the particle surface. The difference in the composition ratios between the surface and the particle center is obtained from the distributions of c_{Pt} and c_{TM} with respect to the horizontal axis in Fig. 3.1.

The CoPt particle showed no significant concentration decomposition, as was the case for the FePt particle and described in the previous chapter, which is consistent with Monte Carlo predictions [45]. In contrast, the surfaces of IrPt and AuPt consisted of one of the two alloy component elements. In IrPt nanoparticles, Pt enrichment was obtained at the particle surface. As the total mass was conserved, the enriched alloy element concentrations on the particle surface resulted in reduced concentrations of these elements inside the particles. Our results were probably consistent with those of the Monte Carlo simulation employing the EAM potential [48], which simulated the Pt segregation on the flat (100) and (111) surfaces of the Ir–Pt alloy. In the cases of CrPt, NiPt, CuPt, and PdPt, the concentration of one component was slightly higher than that of the other, while both elements were still present on the particle surface. In CuPt nanoparticles, both the energetic tight-binding Ising model (TBIM) [83] and

Monte Carlo simulation employing the modified embedded-atom method (MEAM) [47] predicted Cu enrichment of the (100) and (110) surfaces owing to the low surface energy of Cu. For the (111) surface, the Monte Carlo model with MEAM sustained Pt segregation, which was in contrast to the results of the TBIM model. Schurmans *et al.* [47] reported that the reduction in elastic strain energy causes the Pt segregation. In PdPt nanoparticles, slight Pd enrichment on the particle surface occurred, which was in good agreement with the Monte Carlo simulation [48]. Moreover, the difference between the Ni and Pt surface energies was very small. Our simulation predicted slight Ni enrichment on the NiPt particle surface, which was opposite to the prediction made by the Monte Carlo simulation [49]. Therefore, it is suggested that in the case of a small difference in surface energy, as in the NiPt particle, the actual surface could be determined by atomic size mismatch, which was not considered in this model.

Figure 3.1 also shows the phase transformations inside the nanoparticles. At first glance, the stable phase inside the particle changed from an ordered to disordered state as the particle size decreased. The appearance of the ordered phase also varied depending on the alloy combination. The $L1_0$ phase existed stably in the interior of CoPt, CrPt, and FePt particles with diameters above 4 nm. As mentioned in Sec. 3.3.2, the CrPt particles with diameters below 4 nm exhibited the $L1_2$ ordered phase. In the case of CuPt particles, the $L1_1$ phase existed stably in the particles with diameters above 4 nm. The NiPt and PdPt particles demonstrated that the disordered phase was more stable than the ordered phase in all the cases examined.

(a)

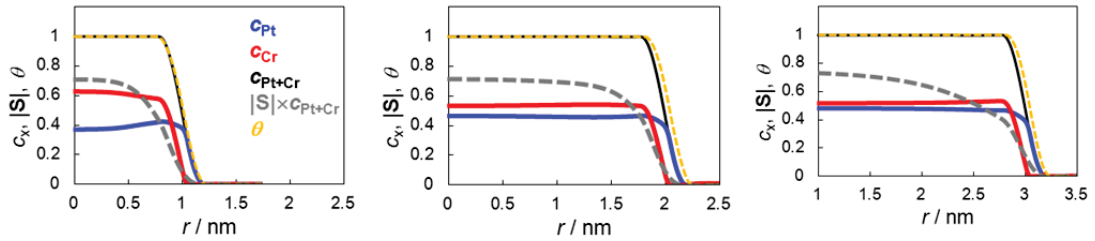
c_{Pt}
c_{Cr}
c_{Pt+Cr}
$|S|\times c_{Pt+Cr}$
θ
c_x, $|S|$, θ
r / nm

(b)

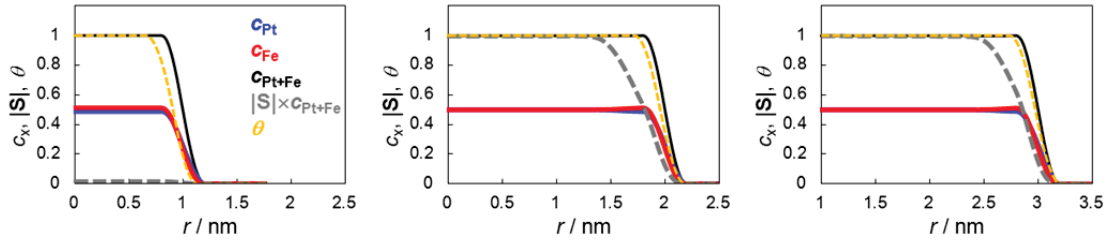
c_{Pt}
c_{Fe}
c_{Pt+Fe}
$|S|\times c_{Pt+Fe}$
θ
c_x, $|S|$, θ
r / nm

(c)

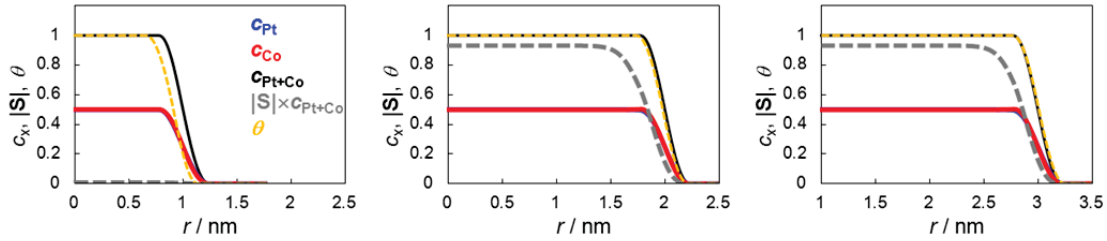
c_{Pt}
c_{Co}
c_{Pt+Co}
$|S|\times c_{Pt+Co}$
θ
c_x, $|S|$, θ
r / nm

(d)

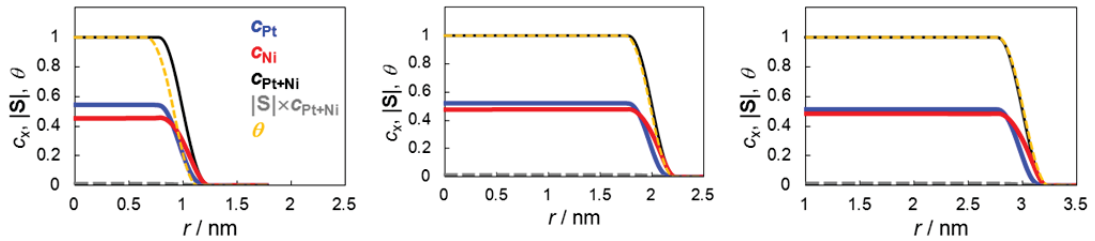
c_{Pt}
c_{Ni}
c_{Pt+Ni}
$|S|\times c_{Pt+Ni}$
θ
c_x, $|S|$, θ
r / nm

(e)

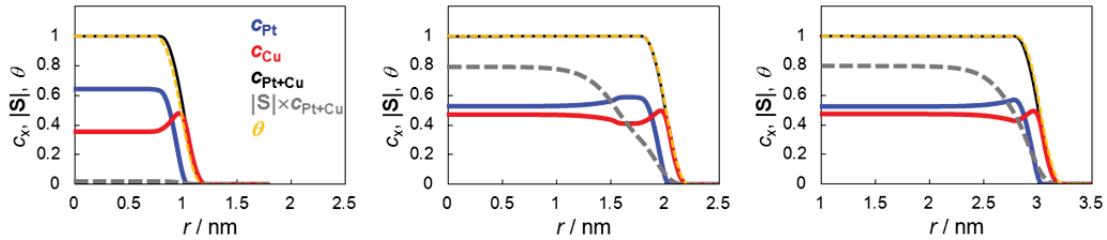
c_{Pt}
c_{Cu}
c_{Pt+Cu}
$|S|\times c_{Pt+Cu}$
θ
c_x, $|S|$, θ
r / nm

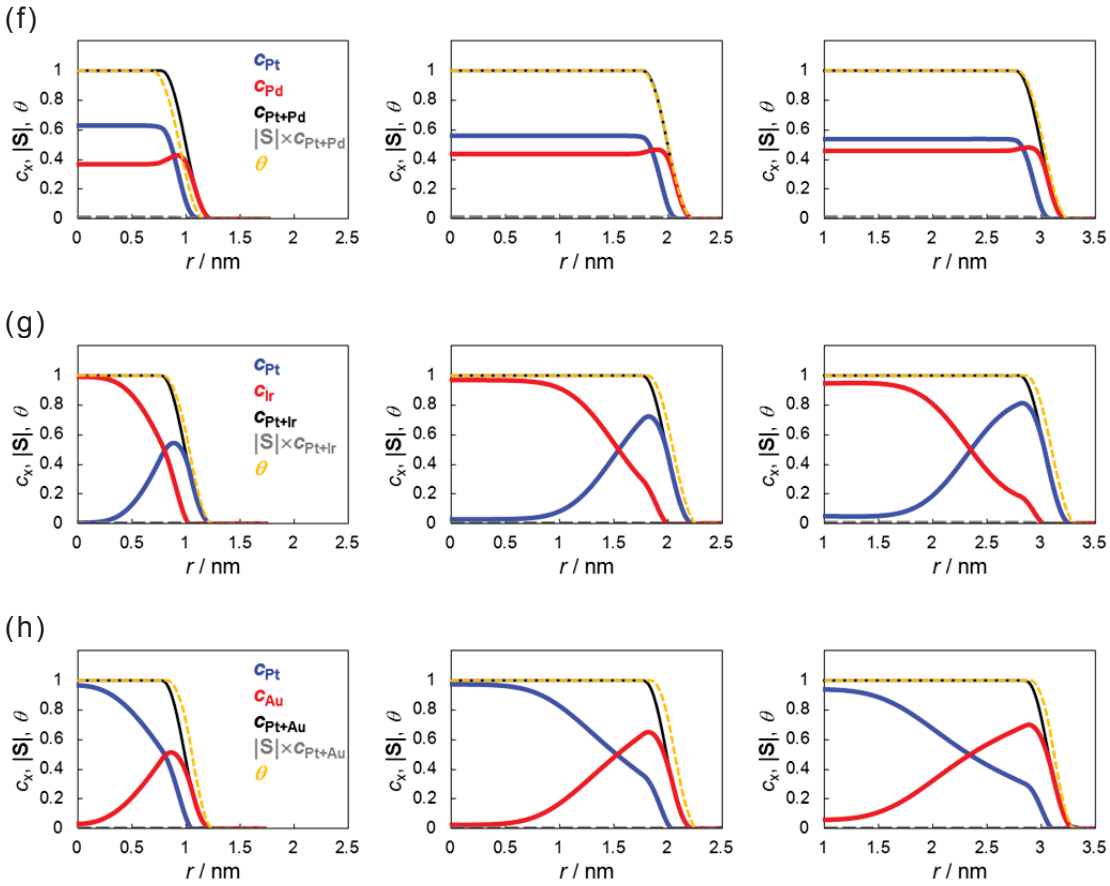

Fig. 3.1. Radial distribution of the mole fraction of each atom, c_x, the long-range ordering parameter, $|\mathbf{S}|$, and the solid–liquid phase transition parameter, θ, within (a) CrPt, (b) FePt, (c) CoPt, (d) NiPt, (e) CuPt, (f) PdPt, (g) IrPt, and (h) AuPt nanoparticles with diameters of 2 nm, 4 nm, and 6 nm at 973.15 K. The horizontal axis denotes the distance from the particle center. The $|\mathbf{S}|$ value of 0 corresponds to the disordered phase. Except for the CrPt particle with a diameter of less than 4 nm, the $|\mathbf{S}|$ value of 1 corresponds to the $L1_0$ (or $L1_1$) ordered phase. In the case of the CrPt particle with a diameter of less than 4 nm, the $|\mathbf{S}|$ value of 0.866 corresponds to the $L1_2$ ordered phase.

To quantitatively understand the extent of the surface segregation, the values obtained from the equation $(\Sigma c_{Pt} - \Sigma c_{TM}) / \Sigma(c_{Pt} + c_{TM})$ for the shell region of the nanoparticle, *i.e.*, $r \geq (d/2 - 0.5)$, which corresponded to the surface shell of the nanoparticle (d is the particle diameter in nm), were evaluated. A positive or negative value indicates Pt or TM segregation, respectively. The values are plotted against the surface energy difference, as shown in Fig. 3.2. The coefficients γ'_{Pt} and γ'_{TM} are defined as γ_{Pt} and γ_{TM} multiplied by the atomic surface areas of their (111) crystal planes, respectively. The difference in surface energy between the two metallic elements acted as a driving force of the surface segregation for these alloy particles. Figure 3.2 shows that the alloy element with the lower surface energy had a tendency to segregate near the surface. The results presented in Fig. 3.2 also indicate that the degree of the segregation decreased as the particle diameter decreased. Because the surface energy difference increased inversely proportional to the particle size, the surface segregation was expected to increase as the particle diameter decreased. On the other hand, since the particle volume decreased as the particle diameter decreased, the degree of the segregation was restricted by the amount of the segregated element contained in a particle. Therefore, it is concluded that the degree of the segregation was affected by the decrease in particle volume more than the increase in surface energy difference.

The surface segregations did not depend on only the alloy surface energies and the particle volume. As shown in Fig. 3.2, the effect of the particle diameter on the degree of the segregation also changed with alloy composition. In the case of AuPt and IrPt, the significant surface segregation was triggered by the

large difference in surface energy. On the other hand, FePt and CoPt particles did not exhibit significant surface segregation, although the absolute difference in surface energy between Fe and Pt was almost identical to that between Cu and Pt.

Thus, because the degrees of the segregation for all examined alloy nanoparticles with the same diameter did not fit on the same straight line, it appears that factors other than the surface energy difference affected the surface segregation. Other potential factors include the attractive interaction between two elements within the alloy particle that suppressed the degree of surface segregation as well as the repulsive interaction that acted as the promoting factor.

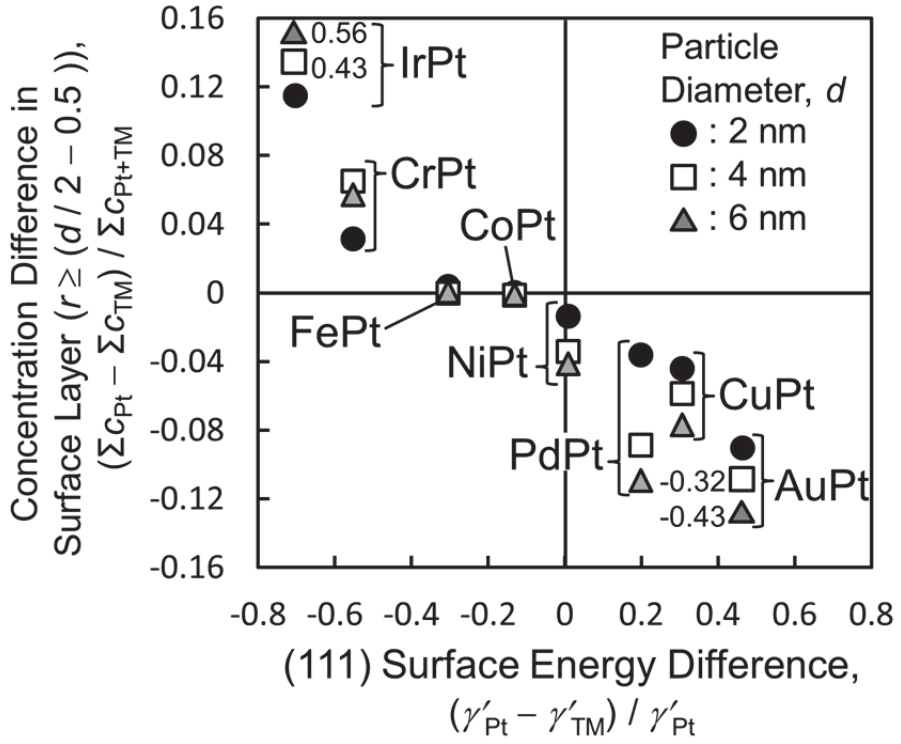

Fig. 3.2. Relationship between the degree of surface segregation and surface energy difference. Positive values on the vertical axis indicate segregation of Pt on the particle surface; positive values on the horizontal axis indicate that the surface energy of Pt was larger than that of the transition metal.

In order to depict the general characteristics of the surface segregation, information regarding the degree of segregation was plotted on a two-dimensional map with respect to the surface energy and the free energy of mixing of the binary alloy using the CALPHAD data, as shown in Fig. 3.3. In addition, the corresponding radial distributions of the values of c_i and $|\mathbf{S}| \times c_{\mathrm{Pt+TM}}$ were calculated, as shown in Figure 3.4. The free energies of mixing of alloys, except IrPt and AuPt, with respect to the vertical axis in Fig. 3.3 were evaluated as deviations from the linear combinations of the free energies of two pure end products of the solutions. In the case of IrPt and AuPt, the mixing energies were evaluated as deviations from the tie-lines that connect the equilibrium compositions of the Pt-rich and Ir-rich (or Au-rich) phases. The composition ratio is 1:1, and the temperature is 973.15 K. The surface energy difference on the horizontal axis is the same as that of Fig. 3.2. To simplify the description of the interatomic interaction and the surface energy, the calculation was performed under conditions that did not consider the existence of the liquid phase. The degree of surface segregation in the alloy particles is expressed by the numerical values shown in parentheses.

In Fig. 3.3, an alloy with a large negative value with respect to the vertical axis means that the solid solution state, including the ordered phase, is stable. No segregation occurs in the FePt particle, for example, despite the surface energy difference, because of the effect of this large mixing energy. In the case of IrPt or AuPt, the mixing energy has a positive value with respect to the vertical axis, which indicates that the solid solution is unstable and decomposition into a TM-rich phase or a Pt-rich phase has occurred. Here, the

phase decomposition triggered by surface segregation is promoted and the surface layer is occupied by one of the two elements. In the case of other binary systems such as CrPt, NiPt, CuPt, and PdPt, the surface-segregated species is determined by the surface energy difference, and the degree of the surface segregation is determined by the balance between the surface energy and chemical interaction between the atomic components.

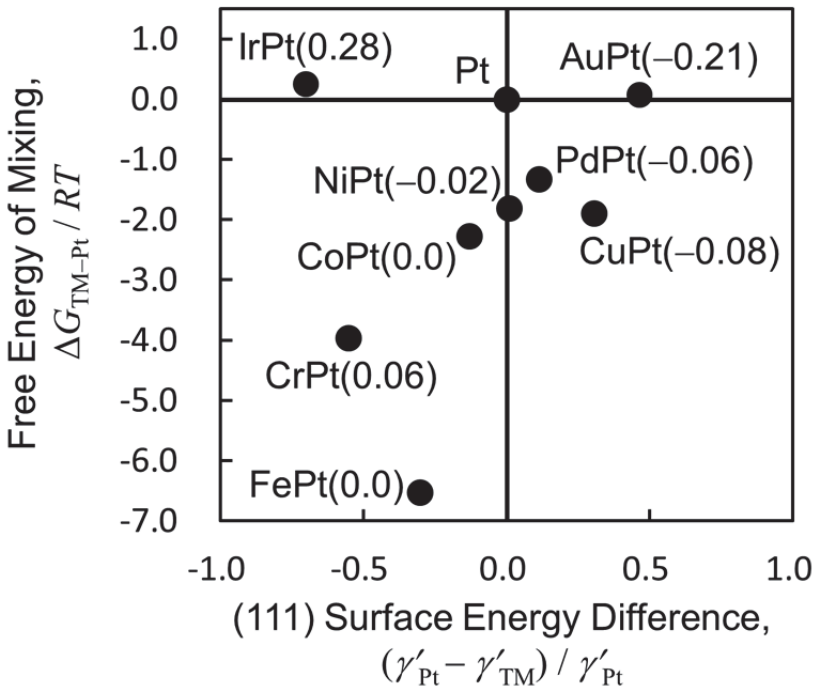

Fig. 3.3. Trend of surface atomic segregation of Pt-based binary nanoparticles. The number within the parentheses following the name of each alloy element is the value calculated using the equation $(\Sigma c_{Pt} - \Sigma c_{TM}) / \Sigma(c_{Pt} + c_{TM})$ for the region where $r \geq (d/2 - 0.5)$ (d is the particle diameter in nm), which corresponds to the surface shell of the nanoparticle. Numerical calculation results were obtained for a particle with a diameter of 3 nm at 973 K.

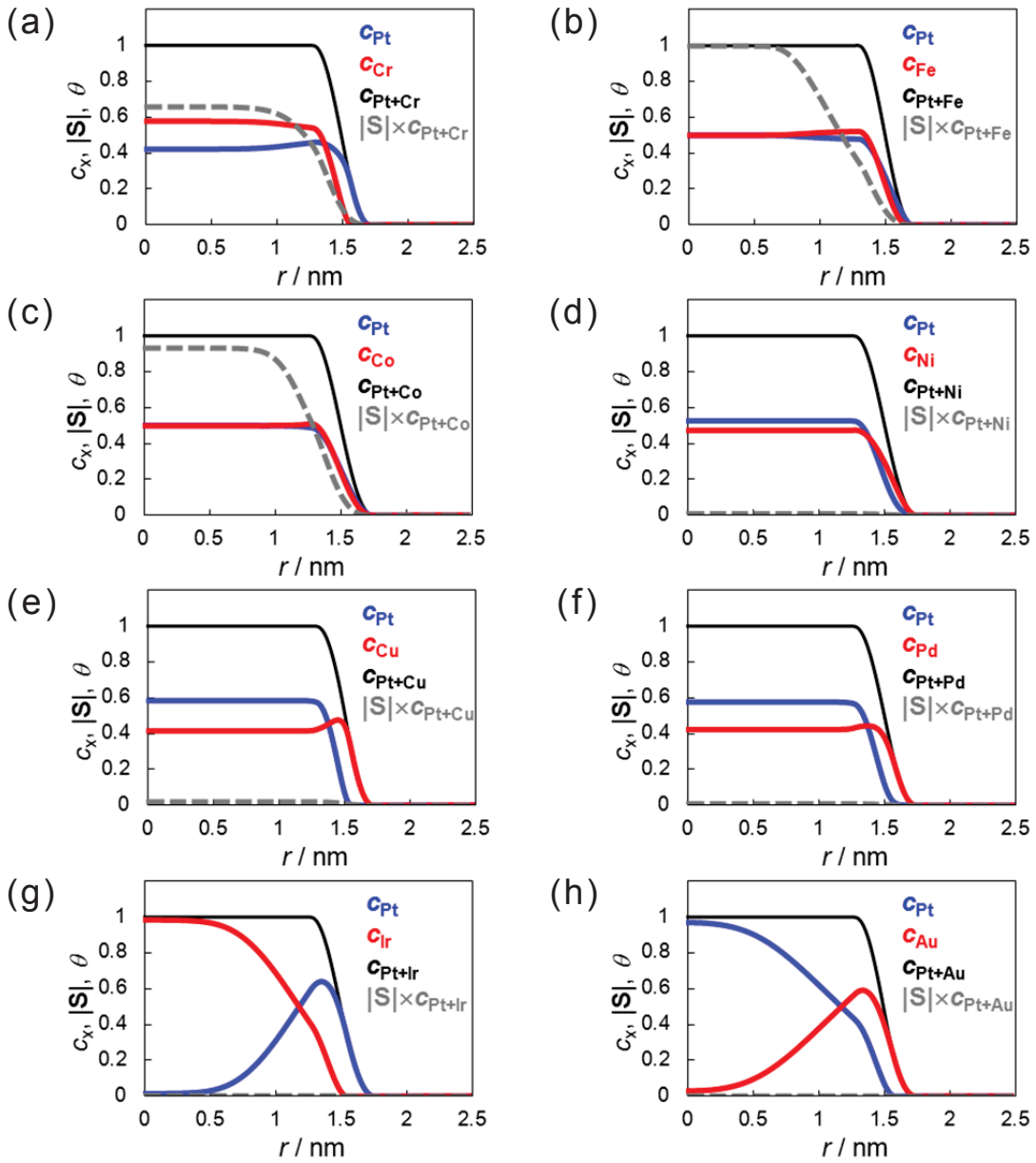

Fig. 3.4. Radial distribution of the mole fraction of each atom, c_x, and the long-range ordering parameter, |**S**|, within (a) CrPt, (b) FePt, (c) CoPt, (d) NiPt, (e) CuPt, (f) PdPt, (g) IrPt, and (h) AuPt nanoparticles with a diameter of 3 nm at 973.15 K. The horizontal axis denotes the distance from the particle center. Except for CrPt particle, the |**S**| values of 0 and 1 correspond to the disordered phase and $L1_0$ (or $L1_1$) ordered phase, respectively. In the case of CrPt particle, the |**S**| values of 0 and 0.866 correspond to the disordered phase and $L1_2$ ordered phase, respectively.

Furthermore, the degree of surface segregation of the binary alloys located on the third quadrant of this map (such as CrPt, FePt, and CoPt) is slightly smaller than that of the binary alloys on the fourth quadrant (such as NiPt, CuPt, and PdPt). In the case of CrPt, FePt, and CoPt, the ordered phase is stable. If the ordered phase is generated because the energy change as a function of the deviation of the composition from a 1:1 composition is more significant, the compositional shift is more strongly suppressed. Therefore, the asymmetry behavior with respect to the horizontal axis in the degree of surface segregation presumably results from the ordered phase formation. Moreover, as shown in Figs. 2.1 and 2.2, the degree of ordering increases as the holding temperature decreases and the particle diameter increases. Therefore, in order to reduce excessive surface segregation and prevent instability in the alloy system, it is possible to take advantage of the formation of the ordered phases by increasing the particle size and decreasing the temperature.

3.3 Surface Segregation of Ternary Nanoparticles

In this section, the binary-alloy model is extended to a multinary form for application to a ternary-alloy system.

3.3.1 Formulation

The conservative temporal evolution of the atomic concentration can be calculated by solving the following equation:

$$\frac{\partial c_i}{\partial t} = \nabla \cdot \left[\sum_{j=1}^{n-1} M_{ij} \nabla \left(\frac{\delta G_{\text{sys}}}{\delta c_j} \right) \right], \quad i \le n-1, \tag{3.1}$$

where c_i is the local atomic concentration of component i as a function of the radial coordinate r and the time variable t, and its value is normalized with respect to the maximum concentration so that it is a dimensionless value between 0 and 1. Here, the binary-alloy (TM–Pt) system is represented by a three-component setup (n = 3): Pt (component 1), the transition-metal element alloyed with platinum TM1 (component 2), and the vacancy Va (component 3). In a ternary-alloy (TM1–TM2–Pt) system, component 3 corresponds to the secondary transition-metal element TM2 and component 4 corresponds to the vacancy. The coefficient M_{ij} is the mobility of component i owing to the gradient of the functional derivative of G_{sys} with respect to the concentration of component j; it is expressed as

$$M_{ii} = c_i(1-c_i)D/RT \quad \text{and} \quad M_{ij} = M_{ji} = -c_i c_j D/RT. \tag{3.2}$$

Here, D is the self-diffusion coefficient; R and T are the gas constant and absolute temperature, respectively. The temporal evolution of the concentration of each component can be calculated under the following condition:

$$\sum_{i=1}^{n} c_i = 1. \tag{3.3}$$

The equilibrium radial distributions of the ordered phase–disordered A1 fcc phase within a nanoparticle can be calculated by solving the following non-conservative equation:

$$\frac{\partial s_i}{\partial t} = -L_s \frac{\delta G_{\text{sys}}}{\delta s_i}, \tag{3.4}$$

where $\mathbf{S} = (s_1, s_2, s_3)$ is defined as the three-component long-range order (LRO) parameter [59]. The parameter (s_1, s_2, s_3) is represented by the values of (1, 0, 0) for complete $L1_0$ and $L1_1$ ordering, and (0.5, 0.5, 0.5) for $L1_2$ ordering. The coefficient L_s is the mobility of the ordered–disordered phase interfaces.

The total free energy of the simulated system, G_{sys}, is defined as the volume integral of the local chemical free energy and gradient energy over the entire volume, V, as follows:

$$G_{\text{sys}} = \frac{1}{V}\int \left[G_{\text{chem}} + \frac{1}{2}\sum_{i=1}^{n} \kappa_i \left(\nabla c_i\right)^2 + h\left(c\right)\frac{\kappa_s}{2}\left|\nabla s\right|^2 \right] \mathrm{d}V, \tag{3.5}$$

$$c = \sum_{i=1}^{n-1} c_i, \tag{3.6}$$

$$h\left(c\right) = c^3\left(6c^2 - 15c + 10\right). \tag{3.7}$$

Here, G_{chem} denotes the changes in the bulk chemical free energies and is evaluated together with the approximation of the regular solution model as

follows:

$$G_{\text{chem}} = \sum_{i=1}^{n-1} c_i {}^{\circ}G_i + \sum_{i=1}^{n-1} \sum_{j=2, j>i}^{n} L_{ij} c_i c_j + \Delta G^{(\text{ord})} + RT \sum_{i=1}^{n} c_i \ln c_i \,, \tag{3.8}$$

where ${}^{\circ}G_i$ is the Gibbs formation energy of pure element i in the solid phase. If the thermodynamic field is not spatially uniform, the bulk free energy, G_{chem}, must be supplemented by an additional energy term with respect to the gradients of the field variables to account for the interfacial interactions.

The term κ_i ($i < n$) represents the gradient energy coefficient with respect to the solid–solid interface between two co-existing phases of mixtures with a miscibility gap:

$$\kappa_i = \left(\sum_{j \neq i}^{n-1} c_j \kappa_{ij} \right) / \sum_{j \neq i}^{n-1} c_j \,, \quad i \leq n-1. \tag{3.9}$$

The κ_{ij} value is determined using the interfacial energy heights estimated from the CALPHAD data and assuming an interface width of 1×10^{-9} m. The coefficient L_{in} represents the interaction energy between alloy element i and a vacancy; κ_n represents the gradient energy coefficient with respect to the solid–vapor interface. L_{in} and κ_n are obtained using the following equations:

$$L_{in} = \Delta H_{\text{f},i} - T \Delta S_{\text{f}} \,, \tag{3.10}$$

$$\kappa_n = \frac{1}{c} \sum_{j=1}^{n-1} c_j \left(\kappa_{nj} - \kappa_j \right). \tag{3.11}$$

In Eq. (3.10), $\Delta H_{\text{f},i}$ and ΔS_{f} are the enthalpy and entropy of mono-vacancy formation, respectively. The ΔS_{f} value adopted an approximate formulation of $1.32R$, which was originally used for platinum [62].

The gradient energy coefficient, κ_s, represents the gradient energy

coefficient with respect to the ordered–disordered phase interface. Most values of the above parameters are already provided in Sec. 3.2.1. In addition, for the calculation of the values for parameters of the Fe–Cr–Pt and Ir–Cr–Pt systems, the CALPHAD data of Fe–Cr [84] and Cr–Ir [85] binary systems were applied.

3.3.2 Results and Discussion

Based on the general trends for the binary system, as shown in the previous section, this method was applied to a ternary-alloy system. From the viewpoint of industrial application as the electro-catalysts of the cathodes in PEFCs, it was certified that, when exposed to a corrosive operating environment such as a low pH and high cathode potential, the transition metals of these alloys dissolve into the aqueous solution containing the polymer electrolyte [86]. The catalytic activity of the ORR is exhibited through a thin skin of pure Pt on the surface of the catalyst particles. Therefore, it may be useful to consider a microstructure where a Pt skin layer is formed on a particle's surface and adhered to its interior. Among the examined binary alloys, the Cr–Pt system is the closest to this structure. Figure 3.5 shows the results for a ternary alloy containing Cr with a diameter of 3 nm at 973 K. First, a $Fe_{0.25}Cr_{0.25}Pt_{0.5}$ nanoparticle was examined. In this case, interactions in the Fe–Pt system were stronger than those in the Cr–Pt system. The relative surface energies of the component elements resulted in Pt enrichment on the surface, and the degree of Pt enrichment was almost the same as that of Cr–Pt. Moreover, the interaction between Fe and Cr was

attractive, but the mixing energy was not very large compared with that of the $L1_0$ ordered phase of Fe–Pt. Therefore, the decomposition in the Fe and Cr concentrations occurred, and the ordered structure was maintained by increasing the Fe concentration inside the particles. The particle interior thus changed to a more stable $L1_0$ ordered structure by adding Fe to Cr–Pt while maintaining the amount of Pt on the surface. Next, a $Ir_{0.4}Cr_{0.1}Pt_{0.5}$ nanoparticle was examined. The Ir–Pt alloy showed the decomposition described in the previous section. On the other hand, Cr–Pt and Cr–Ir formed solid solutions. The interactions in the Cr–Pt system were stronger than those in the Cr–Ir system. The relative surface energies between these components resulted in Pt enrichment on the surface. Therefore, Cr was present in the Pt shell, but a slight increase in the Ir concentration of the Pt shell was observed owing to Cr attracting Ir. Because the complete separation of Pt and Ir was suppressed by the presence of Cr while forming the Pt shell, it is thought that this ternary alloy also improved the stability of the Pt-shell–Ir-core structure.

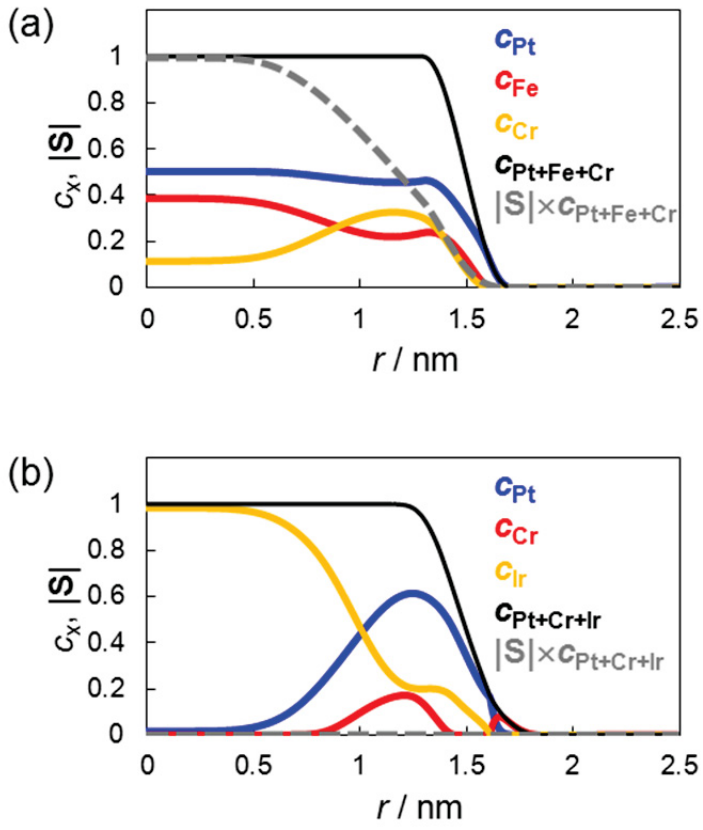

Fig. 3.5. Radial distribution of the mole fraction of each atom, c_x, and the long-range ordering parameter, $|\mathbf{S}|$, within (a) $Fe_{0.25}Cr_{0.25}Pt_{0.5}$ and (b) $Ir_{0.4}Cr_{0.1}Pt_{0.5}$ nanoparticles with diameters of 3 nm at 973.15 K.

3.4 Summary

The radial distributions of the phase transformations and surface segregation in single-alloy nanoparticles were examined as functions of the input values of alloy composition, particle diameter, and temperature. The compositional variation within a single particle was found to depend on the balance between the atomic interaction within particles and the surface energy, and the obtained specific equilibrium points that varied significantly with alloy composition. In the case where the attractive interaction between Pt and the alloyed component was large, especially when an ordered structure was formed, surface segregation was suppressed. In contrast, a weak attractive or repulsive interaction led to the enhancement of the surface layer formation. Thus, it was demonstrated that computer modeling studies are useful for obtaining the overall picture of how the equilibrium structure changes with the variations of the alloy components. It is therefore useful to consider alloy systems that have a microstructure with a Pt skin layer on a particles' surface to improve the catalytic activity. Among the examined binary alloys, the Cr–Pt system has the closest layout to this structure. Furthermore, the ternary-alloy system was briefly examined. In the case of $Ir_{0.4}Cr_{0.1}Pt_{0.5}$ nanoparticles, Cr improved the stability of the Pt-shell–Ir-core structure.

Chapter 4
Numerical Study of Li Diffusion in Polycrystalline $LiCoO_2$

4.1 Introduction

Layered Li transition-metal oxides are widely used as active materials for the positive electrodes of Li-ion rechargeable batteries [21], where intercalation of Li in the metal oxide is a fundamental phenomenon that determines the performance of the batteries. The intercalation process is significantly affected by the crystal anisotropy and grain boundaries, particularly for all-solid-state thin-film batteries as described in Sec. 1.2.2. Therefore, to improve the batteries, a thorough understanding of the intercalation process on the nanometer scale is essential.

Most previously reported numerical simulations [87−89] have adopted several assumptions of the anisotropic Li intercalation process, such as an isotropic grain model and linear Fickian diffusion of Li inside the grains. In these models, because the influence of the polycrystalline anisotropic microstructure on the Li mobility was taken into account through apparent diffusion coefficients, the reaction and diffusion processes of the actual battery electrode were greatly simplified. Consequently, such models could fail to capture important aspects of the charging or discharging dynamics in an essentially anisotropic inhomogeneous medium. It can be easily imagined that a

linked approach for simultaneously modeling the microstructure and transport would be indispensable, because microstructural modeling that does not consider transport cannot identify optimal transport properties for a particular application. The phase-field method is a promising technique [30,50] for calculating the morphological characteristics through microstructural evolution on a nanometer scale. The method has also been applied to describe Li diffusion in a phase-separated system [90,91] and to simulate the anisotropic electrochemical strain microscopy (ESM) response of polycrystalline $LiCoO_2$ [92].

This chapter focuses on gaining a quantitative understanding of the relationship between the morphology of the microstructure and Li diffusivity using numerical simulation techniques. To this end, phase-field models have been proposed for calculating the relationship between the realistic polycrystalline microstructure and the apparent Li diffusion coefficient, D_{app}. Practical applications are simulated using 2D models. A realistic 2D polycrystalline model has been generated from the phase-field simulations—a crystallographic orientation was randomly allocated to each crystal grain, and the grain boundary (GB) was treated as a thin layer between two crystal grains. The D_{app} value was obtained from the temporal evolution of the Li concentration using the Cahn–Hilliard diffusion equation [31], which treated non-Fickian Li diffusion in combination with the anisotropic self-diffusion tensor. A constitutive relationship between Li conductivity and quantitative microstructural features such as average grain size and crystallographic orientation was directly provided from the simulation results. The dependence

of D_{app} on various grain sizes and crystal orientation angles between neighboring grains in the microstructure models is discussed in Sec. 4.3.

4.2 Methods of Calculation

This section describes the methodology used for the numerical simulation of Li diffusion in a 2D polycrystalline microstructure. The temporal evolution of the microstructure was calculated using the phase-field method, based on a diffusion potential of Li that correlates with the equilibrium potential of $LiCoO_2$.

4.2.1 Cahn–Hilliard Diffusion Equation

In order to represent isotropic Li diffusion, the Cahn–Hilliard diffusion equation is introduced:

$$\frac{\partial c}{\partial t} = \nabla \cdot \left[\frac{c(1-c) D_{self}}{RT} \nabla \mu \right], \tag{4.1}$$

where c is the local concentration of Li, normalized by the maximum Li concentration, c_{Li}^{max}, so that it is dimensionless and has a value between 0 and 1. The coefficient D_{self} is the self-diffusion coefficient of Li. The coefficients R and T are the gas constant and the absolute temperature, respectively. Finally, μ represents the diffusion potential of Li, which is defined as the functional

derivative of the total chemical free energy, G_{sys}, with respect to the local concentration:

$$\mu = \frac{\delta G_{sys}}{\delta c}. \tag{4.2}$$

G_{sys} is expressed as the volume integral of the local chemical free energy, G_c, and the gradient energy term, E_{grad}, over the entire system:

$$G_{sys} = G_c + E_{grad} = \frac{1}{V}\int_{\mathbf{r}} \left[G_m + \frac{\kappa}{2}(\nabla c)^2 \right] d\mathbf{r}, \tag{4.3}$$

where G_m is the Gibbs free energy of the uniform binary solution in the Li–vacancy system, and κ is the gradient energy coefficient as estimated from the interaction parameters obtained by fitting the Gibbs free energy function [93] to the mixing enthalpy of the disordered solution. This mixing enthalpy value is estimated from first-principles calculations [94,95]. By substituting Eqs. (4.2) and (4.3) into Eq. (4.1), it can be rewritten as

$$\frac{\partial c}{\partial t} = \nabla \cdot \left[\frac{c(1-c) D_{self}}{RT} \nabla \left(\frac{\partial G_m}{\partial c} - \kappa \nabla^2 c \right) \right]. \tag{4.4}$$

Here, $\partial G_m / \partial c$ is evaluated by utilizing the electrochemical potential:

$$\frac{\partial G_m}{\partial c} = -n_{Li} F \left[U_{LiCoO_2}(c) - U_{ave} \right], \tag{4.5}$$

where n_{Li} is the number of electrons in the charge-transfer reaction, *i.e.*, $n_{Li} = 1$ in $Li^+ + e^- = Li$, and F is Faraday's constant. The term $U_{LiCoO_2}(c)$ is the equilibrium potential of $LiCoO_2$, which is evaluated using Eq. (4.6) [96]:

$$c = \sum_{i=1}^{n} \frac{c_{\max,i}}{1 + \exp\left[\frac{F}{\xi RT}\left(U_{\mathrm{LiCoO_2}} - U_i^0\right)\right]}. \quad (4.6)$$

It is noted that $U_{\mathrm{LiCoO_2}}(c)$ is given as a function of c. The parameters, $c_{\max,i}$, ξ, and U_i^0 are determined by fitting the function to experimental open-circuit potential data [93]. The average potential, U_{ave}, is given by the expression

$$U_{\mathrm{ave}} = (G_{\mathrm{LiCoO_2}} - G_{\mathrm{CoO_2}} - G_{\mathrm{Li}}) / (-n_{\mathrm{Li}} F). \quad (4.7)$$

In order to evaluate G_{m}, it is also possible to use a theoretical approach as an alternative to performing experiments. The thermodynamic parameters of the Gibbs free energy functions for the individual phases in the $\mathrm{Li}_x\mathrm{CoO_2}$ system were previously assessed, and a two-sublattice model [93] was adopted for the Li–vacancy ordered phase. The interaction parameter was determined so as to reproduce the formation entropy, ΔH, as estimated from first-principles calculations [94,95]. To verify the accuracy of the present phase-field model, it was used to estimate the thermodynamic factor, ω, defined as the ratio of D_{chem} to a given D_{self} for homogeneous $\mathrm{LiCoO_2}$. A one-dimensional model with an electrode thickness of 1 μm was employed to mimic the potentiostatic intermittent titration technique (PITT) [97]. The temperature was set at 300.15 K and a potential step of 2 mV was applied, with the current recorded as a function of time. D_{chem} was calculated from the time dependence of the current. The accuracy of this simulation program was verified through a comparison of the calculated value of ω with the experimental result [28,98], as shown in Fig. 4.1. It can be seen that ω varied considerably near a composition of δ = 0.5 ($\mathrm{Li_{0.5}CoO_2}$), which was induced by an increase in the degree of Li–vacancy ordering [99]. The simulated results based on both experimentally and

theoretically evaluated values for G_m were, overall, in good agreement with the measured results, thus justifying the modeling method and parameters used for the simulation.

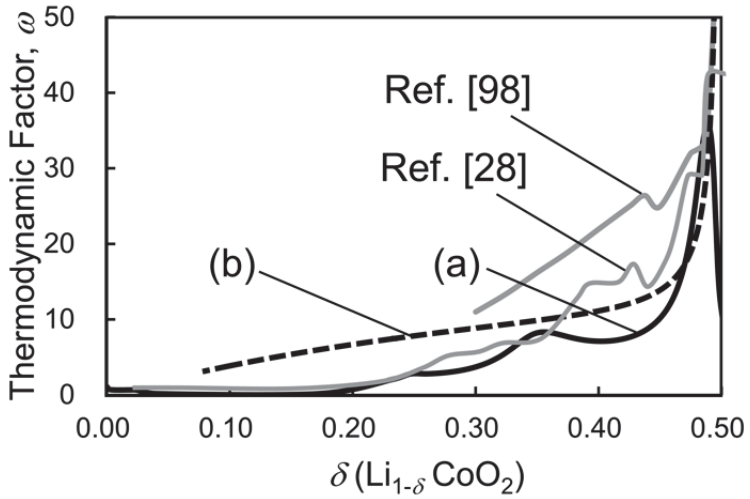

Fig. 4.1. Variation of the thermodynamic factor of Li (defined as the ratio of the chemical diffusion and self-diffusion coefficients) with Li composition. (a) The solid black line and (b) the dashed black line represent results of simulations performed using experimentally and theoretically evaluated U_{LiCoO_2}, respectively. The gray line represents the experimental results.

4.2.2 Li Diffusion in Polycrystalline Materials

Figure 4.2 shows the microstructural features considered in this model, with the crystal structure of fully lithiated $LiCoO_2$ shown in a hexagonal setting in Fig. 1.4. Equation (4.1) can be rewritten using the anisotropic diffusion tensor in order to represent Li diffusion within a $LiCoO_2$ grain:

$$\frac{\partial c}{\partial t} = \nabla \cdot \left[\frac{c(1-c)}{RT} \left(\mathbf{D}' \nabla \mu \right) \right]. \tag{4.8}$$

Microstructure characteristics were taken into account by adopting component values of the diffusion tensor, D'_{ij}, which reflect the local structure. In the inner grains, D'_{ij} is expressed as

$$D'_{ij} = A_{im} A_{jn} \delta_{mn} D_{mn}. \tag{4.9}$$

Here, we assume isotropic Li diffusion on the basal plane of $LiCoO_2$, with D_{11} (= D_{22}) and D_{33} corresponding to $D_{\text{self\_basal}}$ and $D_{\text{self\_}c\text{-axis}}$, respectively. $D_{\text{self\_}c\text{-axis}}$ is the self-diffusion coefficient along the crystallographic *c*-axis direction, while A_{ij} is the rotation matrix randomly allocated to each crystal grain:

$$\left(A_{ij} \right) = \begin{pmatrix} \cos\theta & -\sin\theta & 0 \\ \sin\theta & \cos\theta & 0 \\ 0 & 0 & 1 \end{pmatrix}. \tag{4.10}$$

In the present study, a two-dimensional polycrystalline microstructure was examined under plane strain. The isotropic strain in the basal plane of $LiCoO_2$ was assumed, and the crystallographic *c*-axis of each crystal grain was included in this plane. In this case, A_{ij} is uniquely defined by the orientation angle, θ, which is the angle between the crystallographic basal plane of $LiCoO_2$ and the global Li transport direction, corresponding to one of two axes of the Cartesian coordinate system. The orientation angle θ assigned to each grain is expressed by

$$\theta = m \Delta\theta, \tag{4.11}$$

where $\Delta\theta$ is defined as 180° divided by the total number of grains, N_{gb}. The variable m, which is an integer between zero and N_{gb}, was randomly assigned to

each crystal grain. When θ is zero or 180°, the c-axis of the hexagonal $LiCoO_2$ crystallite is perpendicular to the global Li transport direction.

The GB was assumed to be a thin layer between neighboring grains [100]. In the 2D GB model, a change in the Li concentration in the GB was calculated by the following equations, where the coefficient β was introduced to represent that the Li diffusivity along the GB core and that across the interface between a grain and a GB layer were different from the diffusivity within the grain:

$$\frac{\partial c}{\partial t} = -\frac{1}{h}\left(J_{i=h/2} - J_{i=-h/2}\right) + \frac{\partial}{\partial l}\left[\frac{c(1-c)\beta D_{\text{self}}}{RT}\frac{\partial \mu}{\partial l}\right]. \tag{4.12}$$

Here, h is the GB width, $\boldsymbol{J}_{i=h/2 \text{ or } -h/2}$ denotes the flux of Li across the interface between a grain and a GB layer, and l is the direction along the GB. Calculations were performed for such an inhomogeneous system consisting of the grain and the GB by solving the two types of differential equations, Eqs. (4.8) and (4.12), simultaneously.

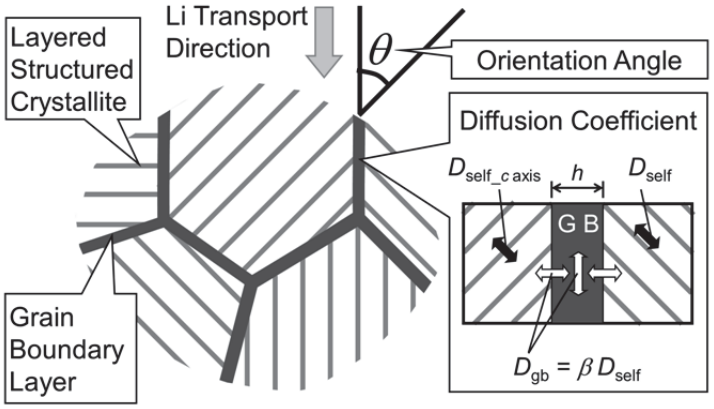

Fig. 4.2. Schematic illustration of the microstructural characteristics treated in this simulation.

4.2.3 Polycrystalline Microstructures

In order to quantitatively discuss the relationship between the polycrystalline microstructure and the Li diffusivity, various models of polycrystalline microstructures were prepared, as shown in Fig. 4.3. The microstructures were obtained using the multi-phase-field algorithm [101] under periodic boundary conditions. The ideal grain growth for a system was simulated under the assumption that the GB energy and the GB mobility were isotropic. The orientation angle θ assigned to each grain is defined by Eq. (4.11). The diameter of an irregularly shaped grain was calculated as that of the circle with the equivalent area. In the following section, the grain size in the polycrystalline model is represented by the ratio of the mean grain diameter to the length of the simulation region, L. Figure 4.4 shows the relationship between the grain size and the volume fraction of the GB layer, V_{gb}, for an assumed GB width of 10 nm.

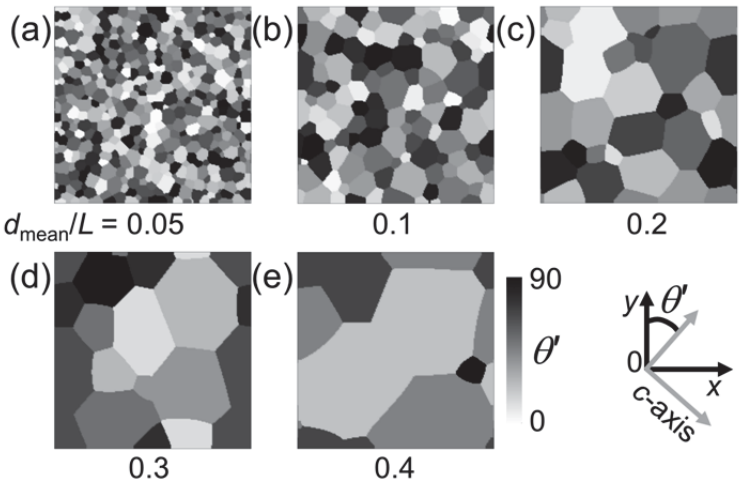

Fig. 4.3. Microstructures of randomly oriented grains with various approximate ratios of the mean grain diameter to the length of the simulation region: (a) 0.05; (b) 0.1; (c) 0.2; (d) 0.3; (e) 0.4. The orientation angle of each grain is represented by its gray tone. The variable θ' is defined as $\theta' = 90 - |90 - \theta|$.

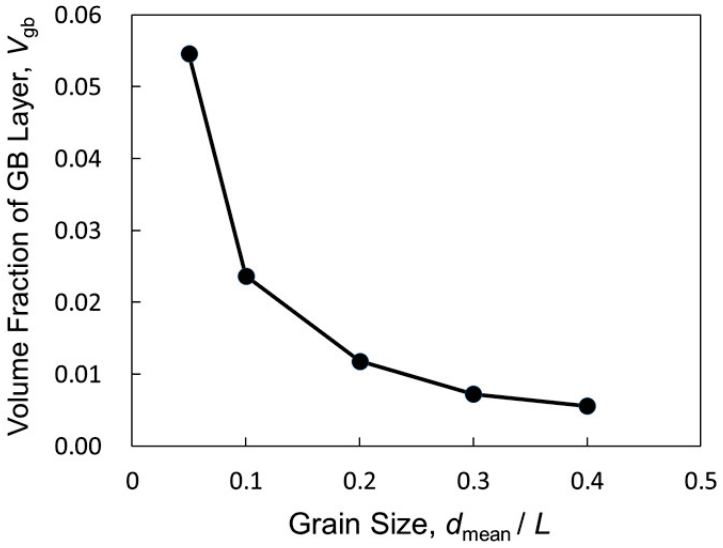

Fig. 4.4. Volume fraction of the GB layer as a function of the grain size. A GB width of 10 nm is assumed.

4.2.4 Numerical Calculation

Two-dimensional numerical calculations were performed by using the finite-volume method with the explicit Euler method. The boundary conditions are listed in Table 4.1. The temperature was 300.15 K, the grid spacing was 0.02 μm, and the simulation region was a square measuring 4.0 × 4.0 μm^2. Finer grid spacing near the GBs was used so that the GB surface could be well represented. The parameters used in the numerical calculation are listed in Table 4.2. Taking into account the experimental Li conductivities obtained using the PITT method for thin films with (003) and (104) preferred orientations [28], $D_{\mathrm{self\_}c\text{-axis}}$ was assumed to be 100 times smaller than the value of $D_{\mathrm{self\_basal}}$.

Table 4.1. Boundary conditions.

$x = 0$ and $x = L$	$y = 0$	$y = L$
$c_{x=0} = c_{x=L}$	$\mathbf{n}\cdot\nabla c = 0$	c = constant or J_{total} = constant

The temporal evolution of the Li concentration in the microstructure induced by a concentration gradient along the y-axis was calculated numerically, as shown in Fig. 4.5. The initial concentration of Li in the microstructure was 0.6, and the Li concentration at $y = L$ was fixed at 0.61. Once $\mathrm{d}c/\mathrm{d}t$ was obtained, D_{app} of Li in the calculation region was evaluated using the following equation

[97]:

$$D_{\mathrm{app}} = -\frac{\mathrm{d}\ln\left(\mathrm{d}c/\mathrm{d}t\right)}{\mathrm{d}t}\frac{4L^2}{\pi^2}, \text{ if } \; t >> L^2 / D_{\mathrm{app}}, \tag{4.13}$$

where L corresponds to the macroscopic Li diffusion length. In an isotropic diffusion system, where Eq. (4.1) holds, D_{app} corresponds to the chemical diffusion coefficient, and the value is greater than or equal to D_{self}.

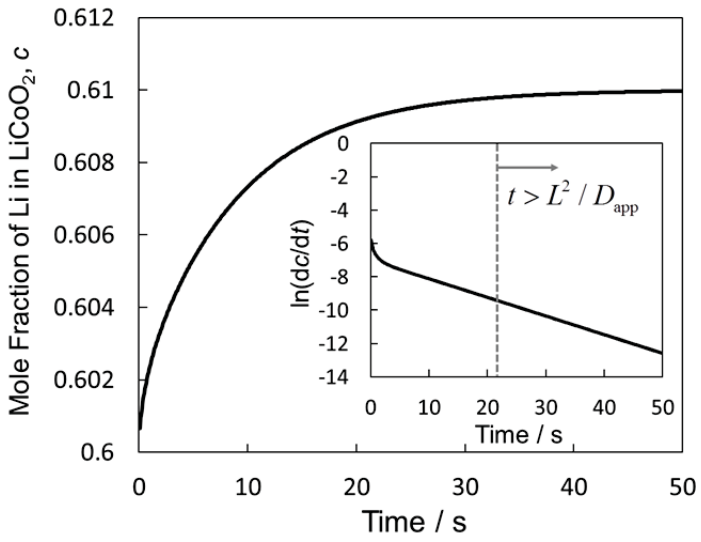

Fig. 4.5. Temporal evolution of the mean Li concentration in the simulation region. The concentration gradually approached the concentration supplied at the position of $y = L$. The value of $\mathrm{d}\ln(\mathrm{d}c/\mathrm{d}t)/\mathrm{d}t$ became constant when the time t was larger than L^2/D_{app}.

When the electrochemical reaction was explicitly treated with the purpose of investigating the degree of Li segregation under realistic discharge conditions, the Butler–Volmer equation [87] was incorporated in the model to describe the

charge-transfer reaction occurring across the $LiCoO_2$–electrolyte interface at $y = L$. The total Li intercalation flux per unit area, J_{total}, is then defined by the following expression:

$$J_{total} = \frac{1}{L}\int J(x, y = L)\,\mathrm{d}\,x, \tag{4.14}$$

with

$$J\left(x, y = L\right) = k\left\{\exp\left[\frac{\alpha_a n_{Li} F}{RT}\left(\phi - U_{LiCoO_2}\right)\right] - \exp\left[-\frac{\alpha_c n_{Li} F}{RT}\left(\phi - U_{LiCoO_2}\right)\right]\right\}, \tag{4.15}$$

$$k = k_0 \cos\theta\left(c_{Li}^{max} - c_{Li}\right)^{\alpha_a}\left(c_{Li}\right)^{\alpha_c}\left(c_{Li^+}\right)^{\alpha_a}, \tag{4.16}$$

where ϕ is the electrode potential and k is the kinetic rate of the electrochemical reaction, which depends on the angle between the basal plane of $LiCoO_2$ and the tangential line of the interface between $LiCoO_2$ and the electrolyte. The terms c_{Li} and c_{Li^+} in Eq. (4.16) are the Li concentrations in $LiCoO_2$ and the electrolyte, respectively; α_a and α_c are the anodic and cathodic transfer coefficients, respectively. In addition, k_0 is the kinetic rate constant of the electrochemical reaction and c_{Li}^{max} is the maximum Li concentration in $LiCoO_2$. The values of these parameters used for the simulations are also listed in Table 4.2. The equilibrium potential function of $LiCoO_2$ in Eq. (4.15) is the same as $U_{LiCoO_2}(c)$ in Eq. (4.6). The current density, I, for this reaction is expressed as $I = J_{total}/F$, and the value was fixed at 0.276 $mA{\cdot}cm^{-2}$. To obtain the converged ϕ value for each individual time step, the Newton–Raphson method was employed. In addition, the potential distribution in $LiCoO_2$ and the electrolyte and the mass transport of Li ions in the electrolyte were calculated using the conventional formulation given in Ref. [87].

Table 4.2. Values of parameters for the numerical simulation.

Parameter	Value
Self-diffusion coefficient of Li,	
$D_{\mathrm{self\_basal}}$ /cm^2·s^{-1}	1×10^{-9}[a]
$D_{\mathrm{self\_}c\text{-axis}}$ /cm^2·s^{-1}	1×10^{-11}
Grain boundary width, h /nm	10.0
Gradient energy coefficient, κ /J·m^2·mol^{-1}	-4.0×10^{-14}
Kinetic rate constant of the electrochemical reaction, k_0 /cm$^{5/2}$·mol$^{-1/2}$·s^{-1}	2.6×10^{-6}
Anodic transfer coefficient, α_a	0.5
Cathodic transfer coefficient, α_c	0.5
Maximum Li concentration, $c_{\mathrm{Li}}^{\max}$ /mol·cm^{-3}	0.051555

[a] Reference [26].

4.3 Results and Discussion

The dependence of D_{app} on the grain size and the manner in which the crystal orientation was assigned to each grain was investigated. The mean orientation angle, θ_{mean}, is defined by the following equation:

$$\theta_{mean} = 90 - \sum_{n_y=1}^{n_y=n_{y\_max}} \sum_{n_x=1}^{n_x=n_{x\_max}} \left| 90 - \theta\left(n_x, n_y\right) \right| / \left(n_{x\_max} \times n_{y\_max}\right), \quad (4.17)$$

where n_{x_max} and n_{y_max} denote the number of grid points along the x-axis and y-axis, respectively, in the numerical simulation region. For this method of assignment, θ_{mean} approached 45° as the number of grains increased. The D_{app} value of the single-crystalline model with θ = 45° was about 3.6 × 10^{-9} $cm^2 \cdot s^{-1}$. Figure 4.6 shows D_{app} as a function of the normalized grain size, d_{mean}/L, for simulations using two different values of β. In the case of β = 1.0, Li was assumed to diffuse in the GB with the same D_{self_basal} value as that in the inner grain. At a glance, all of the D_{app} values corresponding to the polycrystalline models were smaller than those of the single-crystalline model with θ = 45°. A decrease in the grain size led to an increase in D_{app}. When the calculation results for β = 0.01 were compared with those for β = 1.0, a decrease in the grain size did not directly lead to an increase in D_{app}. In this case, the GB appeared to have a blocking effect on Li diffusion. The Li transport involving the GB network was notably affected for a large value of β; the inverse proportionality between D_{app} and the grain size was mainly due to the Li diffusion process utilizing a kind of a channeling through the GB network.

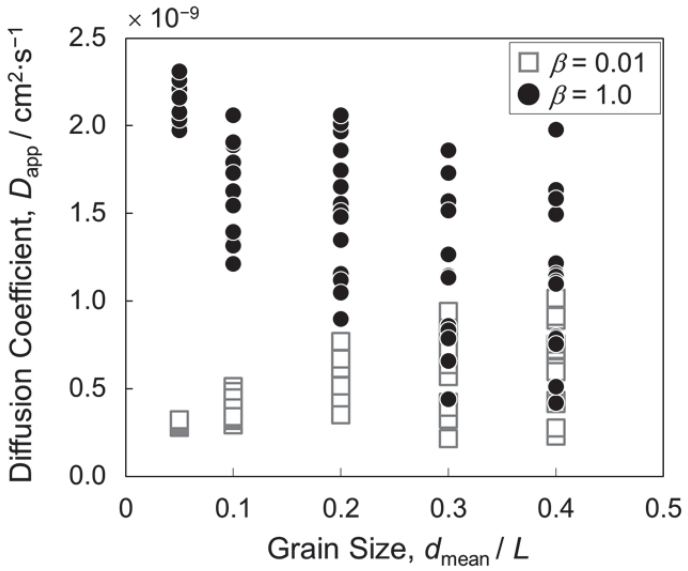

Fig. 4.6. Relationship between the apparent diffusion coefficient and the grain size. The distribution of D_{app} for each grain size and that of the β values originated from the different ways in which the crystal orientation of each grain was assigned.

Another important feature of the results, as shown in Fig. 4.6, was the remarkable variations in D_{app} even when d_{mean} was the same. These variations uniquely depended on the assignment of the orientation angle to each grain. The D_{app} value is plotted against θ_{mean} in Fig. 4.7. The symbols corresponding to d_{mean}/L values of 0.3 or 0.4 show that D_{app} decreased slightly as θ_{mean} increased. Since a θ value of 90° corresponded to a crystallographic *c*-axis parallel to the Li transport direction, the trend shown was reasonable. However, since the variation of D_{app} was still wide even with the same θ_{mean} value, it was difficult to estimate the value of D_{app} from only the value of θ_{mean}.

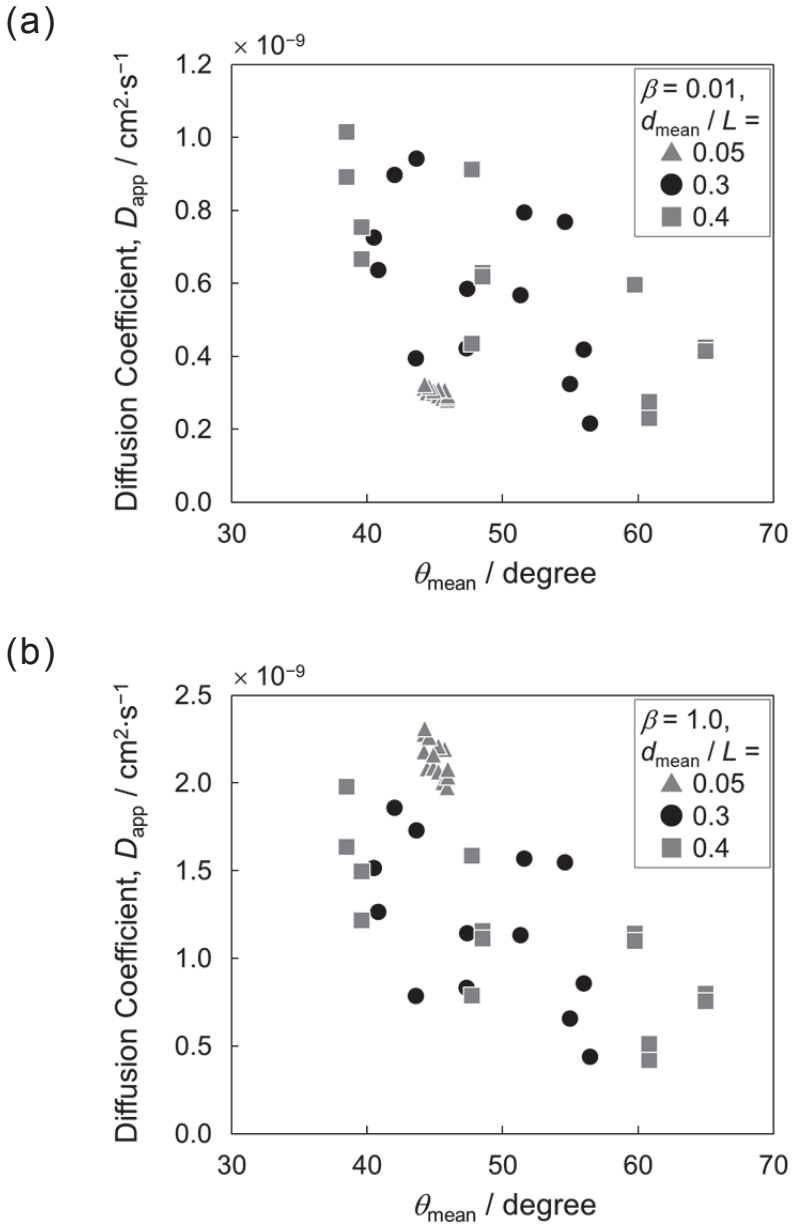

Fig. 4.7. Relationship between the apparent diffusion coefficient and the mean value of the orientation angle, θ_{mean}, estimated using Eq. (4.17) for (a) $\beta = 0.01$ and (b) $\beta = 1.0$.

In fact, the influence of the connectivity of the conduction path between the crystal grains was not represented by the θ_{mean} value. To address this issue, the area-averaged value was evaluated using the following equation to take into account the relative orientation between neighboring grains:

$$\theta_{\mathrm{relative}} = 90 - \sum_{n_y=1}^{n_y=n_{y\_\max}} \left| \sum_{n_x=1}^{n_x=n_{x\_\max}} \left[90 - \theta\left(n_x, n_y\right) \right] \right| / \left(n_{x\_\max} \times n_{y\_\max} \right). \qquad (4.18)$$

The summation in Eq. (4.18) takes into consideration the different signs of θ instead of the absolute value. In Fig. 4.8, D_{app} is plotted against the mean value of the relative orientation angle, $\theta_{\mathrm{relative}}$, and a clear correlation between the two was observed. Large $\theta_{\mathrm{relative}}$ values mean that for most interfaces parallel to the y-axis, the angles for the two neighboring grains sandwiching the interface had opposite signs. When all the GBs parallel to the y-axis were so-called twin boundaries, the $\theta_{\mathrm{relative}}$ value reached 90°, and the flux of Li was restricted by the region near the GBs because the 2D accessible path for Li diffusion was disconnected. The good correlation between $\theta_{\mathrm{relative}}$ and D_{app}, as shown in Fig. 4.8, implied that the characteristics of the GBs parallel to the Li transport direction significantly affected the Li diffusivity. Recently, experimental observation has revealed that the high-coincidence twin boundary stably exists in $LiCoO_2$ thin films [102]. Therefore, the restriction of Li flux by the disconnectedness of the 2D accessible path described in this chapter is believed to occur in an actual polycrystalline $LiCoO_2$ film. Moreover, the D_{app} values corresponding to the d_{mean}/L value of 0.05 for β = 1.0, shown in Fig. 4.8 (b), were somewhat larger than the values expected from the results for the d_{mean}/L values of 0.3 and 0.4. This was mainly because the Li flux in microstructures

with such a small grain size and such good conductive GBs was considerably affected by the GB diffusion. When GB diffusivity was poor, *e.g.*, when β = 0.01, the D_{app} value corresponding to d_{mean}/L = 0.05 was in good agreement with the one predicted using other d_{mean}/L values, as shown in Fig. 4.8 (a).

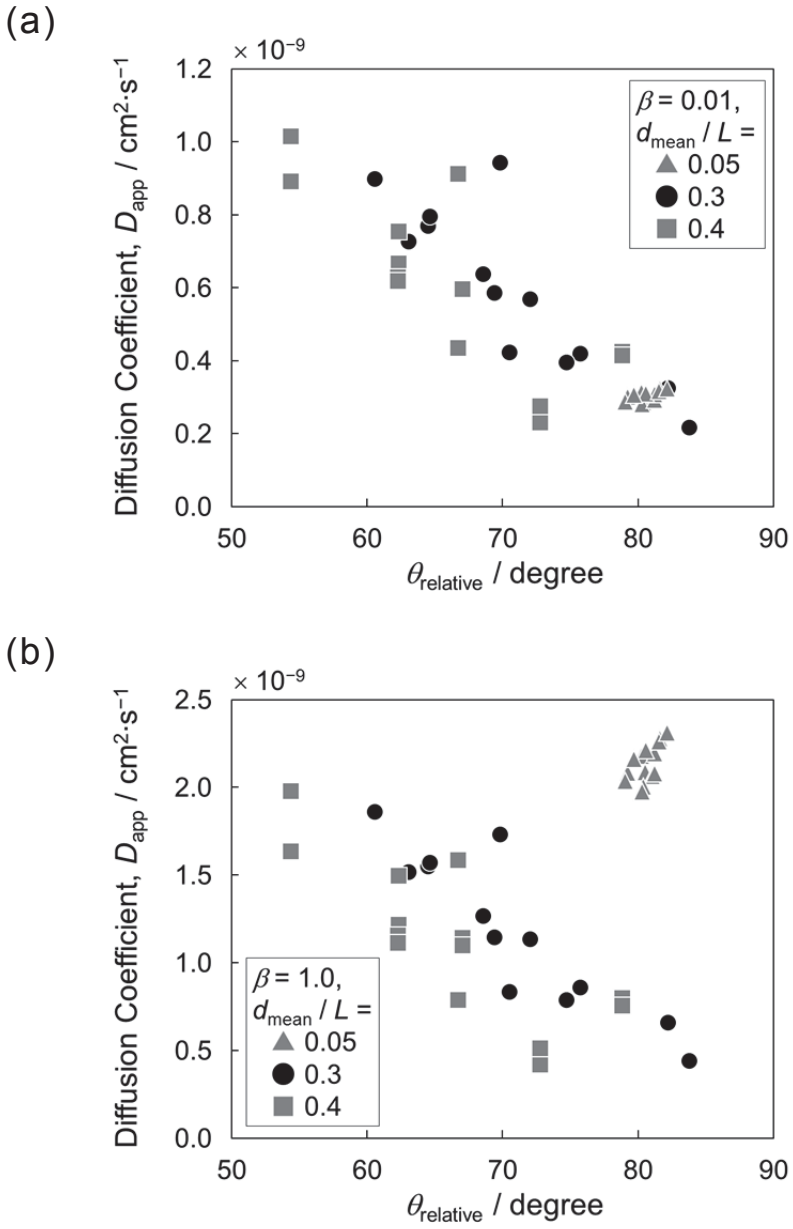

Fig. 4.8. Relationship between the apparent diffusion coefficient and the mean value of the orientation angle, $\theta_{relative}$, estimated using Eq. (4.18) for (a) β = 0.01 and (b) β = 1.0.

It is postulated that the Li diffusion coefficient approximates a linear relationship combining the diffusion coefficients of Li utilizing a GB diffusion circuit, $D_{\text{gb\_circuit}}$, and an alternative path, $D_{\text{grain–grain}}$, as shown in Eq. (4.19):

$$D_{\text{app\_mean}} = V_{\text{gb}} D_{\text{gb\_circuit}} + \left(1 - V_{\text{gb}}\right) D_{\text{grain–grain}} . \tag{4.19}$$

Here, $D_{\text{app\_mean}}$ is an average of values over a range of microstructures in which the β value and grain size are the same. If it is assumed that the value of $D_{\text{grain–grain}}$ is constant for all grain sizes present, then a plot of $D_{\text{app\_mean}}/V_{\text{gb}}$ against $(1-V_{\text{gb}})/V_{\text{gb}}$ yields a linear relationship. The V_{gb} value is represented in Fig. 4.4. As shown in Fig. 4.9, a linear relationship between $D_{\text{app\_mean}}/V_{\text{gb}}$ and $(1-V_{\text{gb}})/V_{\text{gb}}$ suggested a constant value of $D_{\text{grain–grain}}$ for all β values. However, the $D_{\text{grain–grain}}$ value did change slightly with β, as it incorporated the diffusion process across the GB layer. Consequently, changes in Li transferability per unit of GB surface, which were correlated with the β and θ_{relative} values, resulted in a change in $D_{\text{grain–grain}}$. The value of D_{app} was also influenced by the GB volume, which was accounted for, and normalized by, the V_{gb} value. Therefore, when the value of β was determined, the value of $D_{\text{app}}/V_{\text{gb}}$ was expected to be dependent only on changes in θ_{relative}. Fig. 4.10 shows the relationship between $D_{\text{app}}/V_{\text{gb}}$ and θ_{relative}, where it can be seen that variations in $D_{\text{app}}/V_{\text{gb}}$ were solely dependent on changes in β and θ_{relative}.

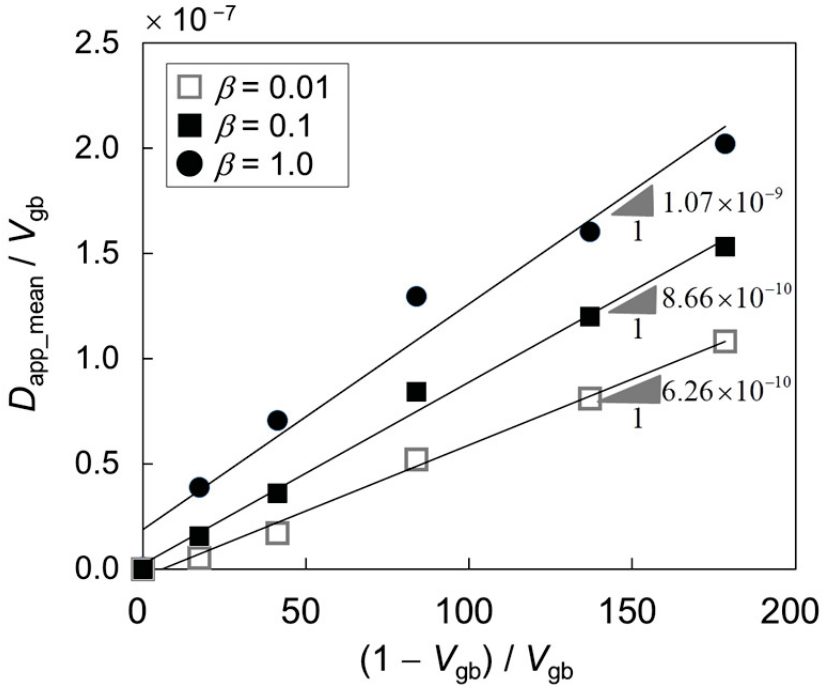

Fig. 4.9. Relationship between D_{app_mean}/V_{gb} and $(1-V_{gb})/V_{gb}$. Gradient values adjacent to the line, which correspond to $D_{grain-grain}$, were obtained by the least mean squares method for a set of plot points. D_{app_mean} is an average of values over a range of microstructures in which the β value and grain size are comparable.

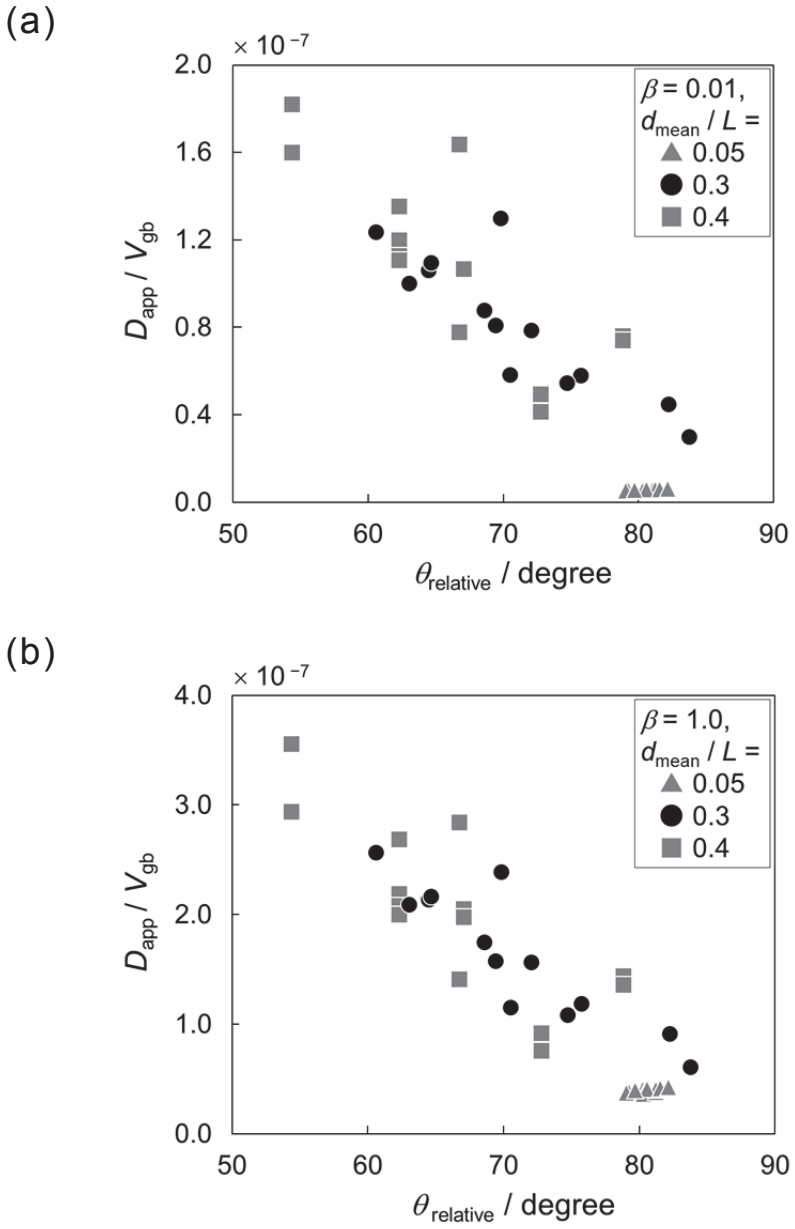

Fig. 4.10. Relationship between D_{app}/V_{gb} and $\theta_{relative}$ for (a) $\beta = 0.01$ and (b) $\beta = 1.0$.

Consequently, it is determined that Li diffusivity in a polycrystalline structure is largely influenced by two main factors: The first is the GB volume per unit volume, which affects the Li flux utilizing the GB network. The second is the relative orientation angle between neighboring grains and Li diffusion, which affects the Li flux per unit grain surface. When the grain size is significantly small, Li diffusivity most likely varies depending on the GB diffusion, since there are a number of ways the crystal orientation of each grain can be assigned such that the resultant θ_{relative} values are almost the same among the various simulation models. Conversely, the diffusivity within a large-grained structure model depends predominantly on the relative orientation angle between neighboring grains, even when the Li conductivity of the GB is quite large, resulting in variations in D_{app}. When the electrode size is quite large, such local inhomogeneities are averaged out. However, in the case of thin-film electrodes, the value of d_{mean} is not that high relative to the electrode thickness. Therefore, an evaluation of d_{mean}/L is useful for obtaining the appropriate electrode microstructure. Once it is possible to experimentally evaluate the grain size relative to electrode size from a 2D image, the possible in-plane variation in electrode performance in relation to d_{mean}/L can be roughly estimated.

The results of the calculations were also used to obtain a relative ratio of D_{app} for a microstructure with grains that were randomly oriented such that $\theta = 0°$. As seen in Figure 4.11, the obtained ratio decreased with increasing grain size and varied within a range of 0.05 to 0.45. In addition, because the ratio behaved similarly for both $\beta = 1$ and $\beta = 0.01$, it follows that the influence of

GB diffusivity and $\theta_{relative}$ could be evaluated separately. The experimental value for ionic conductivity, obtained using the electron blocking method with a randomly oriented sample, was between the conductivities for the (003) and (104) orientations of $LiCoO_2$ [28]. Furthermore, the ratio of the conductivity of a (104)-oriented film to that of a randomly oriented sample was roughly 0.3, giving a thin-film composition of $Li_{0.65}CoO_2$ [28]. Hence, the calculated results were consistent with experimental results.

Finally, the absolute value of D_{app} when $\beta = 1$, as presented in Fig. 4.6, was still quite large in comparison with the experimental D_{chem} of the pulsed-laser-deposited (PLD) film measured by PITT, which varied from 10^{-12} to 10^{-10} $cm^2 \cdot s^{-1}$ [27,28]. Therefore, in order to obtain a good match between the value of D_{app} and the measured value, an extremely low Li GB diffusivity is suggested. Recently, a combined study of high-resolution transition microscopy and first-principles calculations [102,103] has shown that the activation energy of Li diffusion at the twin boundary core is almost twice that of a single crystal. Therefore, this type of GB therefore seems to act as a barrier to Li diffusion.

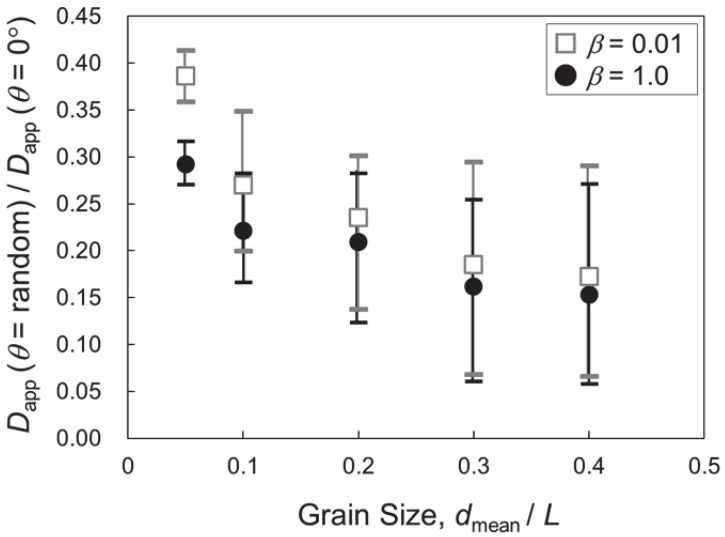

Fig. 4.11. Relationship between the grain size and the ratio of D_{app} of the microstructure with randomly oriented grains to that of the microstructure with oriented grains such that $\theta = 0°$. The open squares and filled circles denote the mean values of the ratio. The ranges of variation of the ratio are shown as error bars.

Another important aspect of the charging or discharging dynamics is the Li segregation in the polycrystalline $LiCoO_2$ thin film induced by the microstructural anisotropy. To investigate that, we used the phase-field model in combination with the electrochemical model. Figure 4.12 shows the change in the Li concentration in polycrystalline $LiCoO_2$ during the discharge process at a constant current. Lithium tends to rapidly diffuse in the direction along the basal plane. As shown in Fig. 4.12, more remarkable Li segregation was induced

when d_{mean}/L was larger than 0.1. The simulation results also showed that the Li segregation was enhanced by decreases in the GB diffusivity. When the grain size relative to the $LiCoO_2$ thickness was small, such as when $d_{mean}/L = 0.05$, the existence of several possible diffusion paths led to a decrease in the degree of Li segregation. These results suggest that Li piles up in one grain when an intergranular angle mismatch is large or when the GB diffusivity is poor, while the assumption of isotropic diffusion is valid for strictly limited cases. The detailed relationship between the microstructures and the discharge property is described in the next chapter.

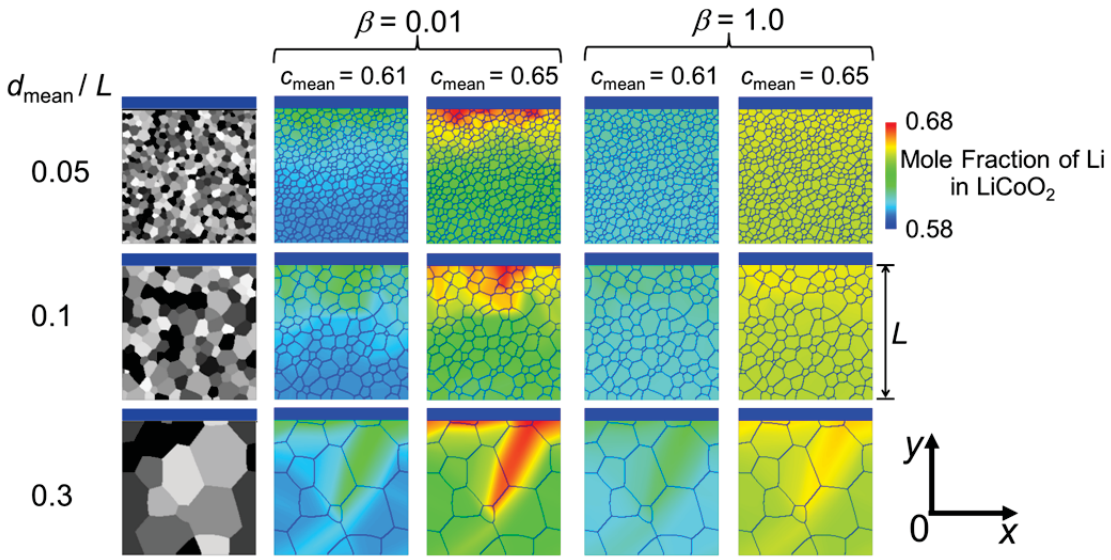

Fig. 4.12. Changes in Li concentration during a constant-current discharge process. The Li transport direction is parallel to the y axis. Here, c_{mean} indicates the Li concentration in Li_xCoO_2 averaged over the entire simulation region. The electrolyte near $LiCoO_2$ is represented by a blue thin layer at $y \geq L$.

4.4 Summary

A phase-field model was used to investigate Li diffusion in polycrystalline Li_xCoO_2 that is randomly oriented on a nanometer length scale. The simulation results demonstrated that Li diffusivity in anisotropic materials is determined by a balance between several basic characteristics related to microstructure, such as the GB properties, the crystallographic orientation, and the grain size.

Li diffusivity in a polycrystalline structure is determined by the GB properties and the mean relative orientation angle between neighboring grains. Diffusivity in a small-grained structure most likely varies depending on GB diffusion, since the mean relative orientation is almost the same among all the models generated for simulation. On the other hand, when the grain size is large, the variation in the mean relative orientation angle increases, and thus diffusivity varies considerably even when the Li conductivity of the GB is quite high. Consequently, it is possible that the diffusivity of a randomly oriented and large-grained microstructure will be one order of magnitude smaller than that of a textured microstructure with $\theta = 0°$.

Chapter 5
Effect of Microstructure on the Discharge Properties of Polycrystalline $LiCoO_2$

5.1 Introduction

As reported in Chapter 4, the phase-field model was used to investigate Li diffusion in randomly oriented polycrystalline $LiCoO_2$. A crystallographic orientation was randomly allocated to each crystal grain. The general trend in apparent Li diffusivity, which reflected the GB characteristics parallel to the Li transport direction, was explained by the grain boundary (GB) diffusivity, and by taking into account the relative orientations of neighboring grains.

In this chapter, the relationship between various microstructural features and the constant-current discharge properties of $LiCoO_2$ is presented. In particular, the influence of the elastic stress field associated with Li intercalation was investigated. A numerical model that includes the elastic stress field has previously been proposed in earlier studies [92,104,105]. However, most numerical simulations have adopted an isotropic diffusion medium [104,105] or have conducted separate evaluations of the diffusion process and the stress field [92]. Therefore, the influence of heterogeneous polycrystalline structure on the Li diffusion process has not been fully understood. On the other hand, the phase-field model, which could factor in non-Fickian diffusion generated from the Li concentration and the elastic strain,

offered a clear picture. The simulation took into account the Li diffusion along or across the GB modeled as a thin layer, as well as the effect of $LiCoO_2$ crystallographic anisotropy on the self-diffusion coefficient of Li. Furthermore, the model incorporated the Butler–Volmer equation to determine Li flux across the $LiCoO_2$–electrolyte interface. The effects of microstructure on the discharge properties were then explored as a function of the grain size, spatial distribution of the crystal orientation for each grain, and GB diffusivity.

5.2 Methods of Calculation

Formulations and implementations of the simulation of Li diffusion generated by the elastic stress field associated with Li concentration are described herein.

5.2.1 Formulation

In order to take into account the effect of elastic strain energy, the total free energy G_{sys} is expressed as

$$G_{sys} = G_c + E_{grad} + E_{str}, \tag{5.1}$$

where G_c, E_{grad}, and E_{str} correspond to the chemical free energy, gradient energy, and elastic strain energy, respectively. G_c and E_{grad} are determined in the manner described in Sec. 4.2.1. The term E_{str} is expressed in the following form [106]:

$$E_{\mathrm{str}} = \frac{1}{2V}\int_{\mathbf{r}} C_{ijkl}(\mathbf{r})\left[\varepsilon_{ij}^{\mathrm{c}}(\mathbf{r},t)-\varepsilon_{ij}^{0}(\mathbf{r},t)\right]\left[\varepsilon_{kl}^{\mathrm{c}}(\mathbf{r},t)-\varepsilon_{kl}^{0}(\mathbf{r},t)\right]\mathrm{d}\mathbf{r}, \tag{5.2}$$

where $C_{ijkl}(\mathbf{r})$ is the elastic stiffness constant; $\varepsilon_{ij}^{\mathrm{c}}(\mathbf{r},t)$ and $\varepsilon_{ij}^{0}(\mathbf{r},t)$ are the constrained strain and the eigenstrain, respectively. The variables $\varepsilon_{ij}^{\mathrm{c}}(\mathbf{r},t)$ and $\varepsilon_{ij}^{0}(\mathbf{r},t)$ are expressed as

$$\varepsilon_{ij}^{\mathrm{c}}(\mathbf{r},t) = \bar{\varepsilon}_{ij}^{0}(t) + \delta\varepsilon_{ij}^{\mathrm{c}}(\mathbf{r},t), \tag{5.3}$$

$$\varepsilon_{ij}^{0}(\mathbf{r},t) = A_{im}(\mathbf{r})A_{jn}(\mathbf{r})\eta_{mn}(\mathbf{r},t), \tag{5.4}$$

where $\eta_{mn}(\mathbf{r},t)$ is the lattice misfit and $A_{ij}(\mathbf{r})$ is the rotation matrix randomly allocated to each crystal grain, as shown in Eq. (4.10). Here, a two-dimensional polycrystalline microstructure is examined under plane strain, with the crystallographic *c*-axis of each crystal grain included in this plane. The strain in the basal plane of $LiCoO_2$ is assumed to be isotropic. The variable $\bar{\varepsilon}_{ij}^{0}(t)$ is the mean strain averaged over the entire system, whereas $\delta\varepsilon_{ij}^{\mathrm{c}}(\mathbf{r},t)$ is defined as the deviation of the local strain from $\bar{\varepsilon}_{ij}^{0}(t)$. When $\delta\varepsilon_{ij}^{\mathrm{c}}(\mathbf{r},t)$ is calculated using an equation for inhomogeneous elasticity, it results in a calculation that adopts a self-consistent iterative scheme [107], as described below. To satisfy the differential stress-equilibrium equations, Eq. (5.5) is introduced:

$$\sigma_{ij,j}^{\mathrm{el}}(\mathbf{r},t) = \frac{\partial\sigma_{ij}^{\mathrm{el}}(\mathbf{r},t)}{\partial x_j} = C_{ijkl}\left[\frac{\partial\delta\varepsilon_{kl}^{\mathrm{c}}(\mathbf{r},t)}{\partial x_j} - \frac{\partial\varepsilon_{kl}^{0}(\mathbf{r},t)}{\partial x_j}\right] + \frac{\partial\left\{\Delta C_{ijkl}(\mathbf{r})\left[\bar{\varepsilon}_{kl}^{\mathrm{c}} + \delta\varepsilon_{kl}^{\mathrm{c}}(\mathbf{r},t) - \varepsilon_{kl}^{0}(\mathbf{r},t)\right]\right\}}{\partial x_j} = 0. \tag{5.5}$$

Eq. (5.5) is then transformed to yield

$$C_{ijkl}\frac{\partial\delta\varepsilon_{kl}^{\mathrm{c}}(\mathbf{r},t)}{\partial x_j} = C_{ijkl}\frac{\partial\varepsilon_{kl}^{0}(\mathbf{r},t)}{\partial x_j} - \frac{\partial\left\{\Delta C_{ijkl}(\mathbf{r})\left[\bar{\varepsilon}_{kl}^{\mathrm{c}} + \delta\varepsilon_{kl}^{\mathrm{c}}(\mathbf{r},t) - \varepsilon_{kl}^{0}(\mathbf{r},t)\right]\right\}}{\partial x_j}. \tag{5.6}$$

When $u_i(\mathbf{r},t)$ is defined as a displacement, the relationship between $u_i(\mathbf{r},t)$ and $\delta\varepsilon_{kl}^{c}(\mathbf{r},t)$ can be written as

$$\delta\varepsilon_{kl}^{\mathrm{c}}(\mathbf{r},t)=\frac{1}{2}\left[\frac{\partial u_k(\mathbf{r},t)}{\partial x_l}+\frac{\partial u_l(\mathbf{r},t)}{\partial x_k}\right]. \tag{5.7}$$

Eq. (5.8) is obtained by substituting $\delta\varepsilon_{kl}^{\mathrm{c}}(\mathbf{r},t)$ with Eq. (5.7) in Eq. (5.6), followed by executing a Fourier transform:

$$C_{ijkl}k_jk_lu_k(\mathbf{k},t)=-ik_j\left\{C_{ijkl}\varepsilon_{kl}^0(\mathbf{k},t)-\left[\Delta C_{ijkl}(\mathbf{r})\left(\bar{\varepsilon}_{kl}^{\mathrm{c}}+\delta\varepsilon_{kl}^{\mathrm{c}}(\mathbf{r},t)-\varepsilon_{kl}^0(\mathbf{r},t)\right)\right]_{\mathrm{k}}\right\}, \tag{5.8}$$

where $\mathbf{k}$ is the reciprocal space vector, and $[]_{\mathrm{k}}$ means that the Fourier transform within the brackets occurs after the calculations in real space. Equation (5.8) can be rewritten as per Eq. (5.9) using $G_{ik}(\mathbf{k})=(C_{ijkl}k_jk_l)^{-1}$:

$$u_k(\mathbf{k},t)=-iG_{ik}k_j\left\{C_{ijkl}\varepsilon_{kl}^0(\mathbf{k},t)-\left[\Delta C_{ijkl}(\mathbf{r})\left(\bar{\varepsilon}_{kl}^{\mathrm{c}}+\delta\varepsilon_{kl}^{\mathrm{c}}(\mathbf{r},t)-\varepsilon_{kl}^0(\mathbf{r},t)\right)\right]_{\mathrm{k}}\right\}. \tag{5.9}$$

Substituting Eq. (5.9) into a Fourier transform of Eq. (5.7), followed by executing an inverse Fourier transform, the variable $\delta\varepsilon_{ij}^{\mathrm{c}}(\mathbf{r},t)$ can be expressed as

$$\begin{aligned}
\delta\varepsilon_{kl}^{\mathrm{c}(n)}(\mathbf{r},t)&=\frac{1}{2}\left(\frac{\partial u_k(\mathbf{r},t)}{\partial x_l}+\frac{\partial u_l(\mathbf{r},t)}{\partial x_k}\right)=\frac{1}{2}\int_k i\left\{k_lu_k(\mathbf{k},t)+k_ku_l(\mathbf{k},t)\right\}\exp(i\mathbf{k}\cdot\mathbf{r})\frac{d\mathbf{k}}{(2\pi)^3}\\
&=\frac{1}{2}\int_k -i^2\left\{k_lG_{ik}(\mathbf{k})+k_kG_{il}(\mathbf{k})\right\}k_j\left\{C_{ijkl}\varepsilon_{kl}^0(\mathbf{k},t)-\left[\Delta C_{ijkl}(\mathbf{r})\left(\bar{\varepsilon}_{kl}^{\mathrm{c}}+\delta\varepsilon_{kl}^{\mathrm{c}(n-1)}(\mathbf{r},t)-\varepsilon_{kl}^0(\mathbf{r},t)\right)\right]_{\mathrm{k}}\right\}\exp(i\mathbf{k}\cdot\mathbf{r})\frac{d\mathbf{k}}{(2\pi)^3}\\
&=\frac{1}{2}\int_k\left\{n_l\Omega_{ik}(\mathbf{n})+n_k\Omega_{il}(\mathbf{n})\right\}n_j\left\{C_{ijkl}\varepsilon_{kl}^0(\mathbf{k},t)-\left[\Delta C_{ijkl}(\mathbf{r})\left(\bar{\varepsilon}_{kl}^{\mathrm{c}}+\delta\varepsilon_{kl}^{\mathrm{c}(n-1)}(\mathbf{r},t)-\varepsilon_{kl}^0(\mathbf{r},t)\right)\right]_{\mathrm{k}}\right\}\exp(i\mathbf{k}\cdot\mathbf{r})\frac{d\mathbf{k}}{(2\pi)^3},
\end{aligned} \tag{5.10}$$

where $\Omega_{ij}(\mathbf{n})=k^2G_{ij}(\mathbf{k})$ and n in $\delta\varepsilon_{kl}^{\mathrm{c}(n)}(\mathbf{r},t)$ refers to the iteration number. In the case of inhomogeneous elasticity, since the right hand side of Eq. (5.10) contains $\delta\varepsilon_{ij}^{\mathrm{c}}(\mathbf{r},t)$, a self-consistent value of $\delta\varepsilon_{ij}^{\mathrm{c}}(\mathbf{r},t)$ is obtained using iterative calculation. For homogeneous elasticity, the elastic stiffness constant is not dependent on the global coordination, and iterative calculation is thus not necessary.

5.2.2 Numerical Calculation

The effect of various microstructures on the Li diffusivity was evaluated in combination with the Li diffusion model shown in the previous chapter and the two-dimensional model representing the orientation of the $LiCoO_2$. Figure 5.1 shows the two-dimensional polycrystalline microstructures generated from the multi-phase-field simulations [101]. The number of grid points along each axis, n_{max}, was set to be 256. The variable θ represents the relative angle with respect to the y-axis, as defined by Eq. 4.11, where the y-axis is parallel to the global direction of Li transport.

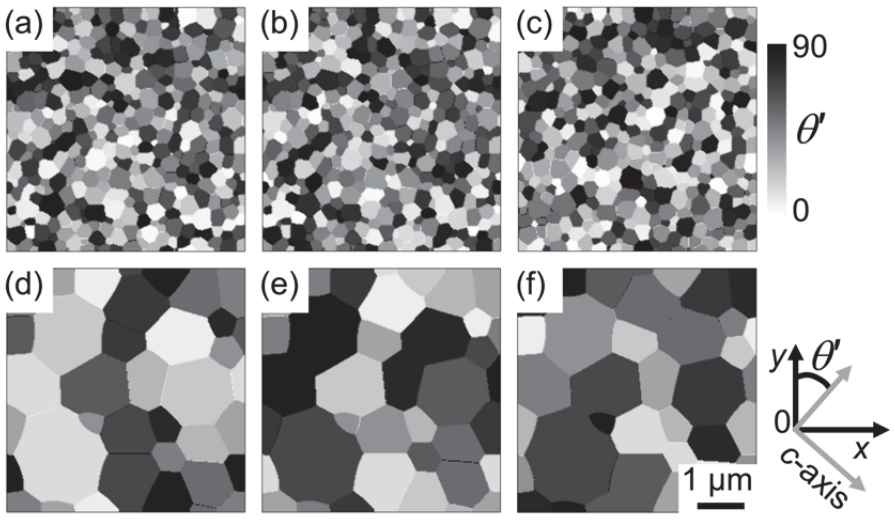

Fig. 5.1. Two-dimensional models of a polycrystalline microstructure with randomly oriented grains. The orientation angle of each grain is represented by its gray tone. The variable θ' is defined as $\theta' = 90 - |90 - \theta|$.

It is demonstrated in Chapter 4 that the difference in the apparent diffusion coefficient caused by the disconnectivity of Li diffusion paths between neighboring grains can be estimated by the area-averaged value defined in Eq. (4.18). It was confirmed that the apparent Li diffusivity of the polycrystalline model with θ defined in Eq. (4.11) decreased as $\theta_{\mathrm{relative}}$ increased. Fine- and coarse-grained models with median or upper/lower limit value of $\theta_{\mathrm{relative}}$ were examined, as shown in Table 5.1. The grid spacing was 0.02 μm. Finer grid spacing near the GBs was used to represent Li diffusion in the GB thin layer. Fisher *et al.* [102], using first-principles calculation, predicted that the activation energy of Li diffusion at the twin boundary core is almost twice as large as that in the single crystal. Therefore, it is important to examine the condition that allows the GB to acts as an obstacle to Li diffusion. The GB width was set to 2 nm, which approximately corresponded to the width of the region where the activation energy deviated from that inside the grain. $D_{\mathrm{self\_basal}}$ and $D_{\mathrm{self\_}c\mathrm{\text{-}axis}}$ of inner grains were 1.0×10^{-9} and 1.0×10^{-11} $\mathrm{cm^2 \cdot s^{-1}}$, respectively [26,28]. D_{gb} was introduced to represent the Li diffusivity along or across the GB thin layer, and is defined as $D_{\mathrm{gb}} = D_{\mathrm{self\_basal}}$ or $D_{\mathrm{gb}} = 0.01 D_{\mathrm{self\_basal}}$. The elastic stiffness components of $LiCoO_2$ were theoretically estimated in Ref. [108]. Here, we regard the elasticity of $LiCoO_2$ as being isotropic, and thus the corresponding stiffness component is defined by two parameters, λ and μ, which are called Lamé's constants. The values of λ and μ were set to 133.5 and 120.9 GPa, respectively, to reproduce the values of C_{33} ($= \lambda + 2\mu$) and C_{13} ($= C_{23} = \lambda$) in order to properly describe the displacement in the *c*-axis direction. When a Li atom is deintercalated from the host lattice, the lattice constant along the *c*-axis

increases locally owing to the electrostatic repulsion of the oxygen layer [94]. Therefore, it is assumed that the crystal lattice misfit is expressed as $\eta_{ij}(\mathbf{r},t)=\left[1-c(\mathbf{r},t)\right]\delta_{ij}\eta'_{ij}$. The coefficient δ_{ij} is the Kronecker delta. The values of $\eta'_{11}(=\eta'_{22})$ and η'_{33} were set at −0.005 and 0.05, respectively, based on previously reported lattice parameters measured from X-ray diffraction patterns, as shown in Fig. 5.1 [109,110].

The electrochemical reaction was explicitly treated to investigate the discharge capacity under realistic discharge conditions. The Butler–Volmer equation was incorporated into the model to determine the Li flux across the $LiCoO_2$–electrolyte interface at $y = 0$ and $y = L$, where L represents the length of the simulation region. The total Li intercalation flux per unit area was determined by Eq. (4.14). The adopted equilibrium potential of $LiCoO_2$, given as a function of Li concentration, was evaluated in Ref. [96]. The initial voltage, V, was about 4.026 V, which corresponded to a Li concentration of 0.6 at equilibrium. The kinetic rate constant of the electrochemical reaction was 2.0×10^{-6} $cm^{5/2}\cdot mol^{-1/2}\cdot s^{-1}$. The current density for this reaction was set to be 3.45 $mA\cdot cm^{-2}$, which corresponded to a discharge rate of approximately 20C discharge rate. The temperature was set at 298.15 K. Because the focus of this study is to clarify how the microstructure of $LiCoO_2$ affects its discharge properties, the model did not address the potential distribution in $LiCoO_2$ and the electrolyte, or the mass transport of Li ions in the electrolyte.

5.3 Results and Discussion

The effects of microstructure on the apparent diffusion coefficient and discharge properties were investigated and reported in the following sections.

5.3.1 Apparent Diffusion Coefficient

Figure 5.2 shows a schematic illustration of the oriented single crystal model. The stress was assumed to have a value of 0, and the Li composition was 1.0. Because allowance was made for the whole body to be freely distorted, the stress remained at zero when the Li composition was varied from 1.0 to 0.6. When the potential was increased stepwise from this state, the Li composition of the electrochemical reaction surface was higher than that of the single crystal interior. As a result of this compositional difference, an elastic strain was induced in the crystal. The distribution of σ_{xx} at a mean Li concentration of 0.605 is also shown in Fig. 5.2. A tensile stress in the *x* direction was induced in the (100)-oriented model (Fig. 5.2 (a)), in which the Li layer was parallel to the *x*-axis. The introduction of tensile elastic stress during Li intercalation has also been experimentally observed in a $LiCoO_2$ thin film with (104) preferred orientation using laser beam deflection [111]. On the other hand, the compressive stress state was along the *x* direction in the case of a (003)-oriented model (Fig. 5.2 (b)), in which the Li layer was perpendicular to the *x*-axis. Since

the misfit strain of the *c*-axis was one order of magnitude larger than that of the *a*- and *b*-axis, the absolute stress value for each model also changed by an order of magnitude. In addition, the vertical stress in the *y* direction was close to zero in each model.

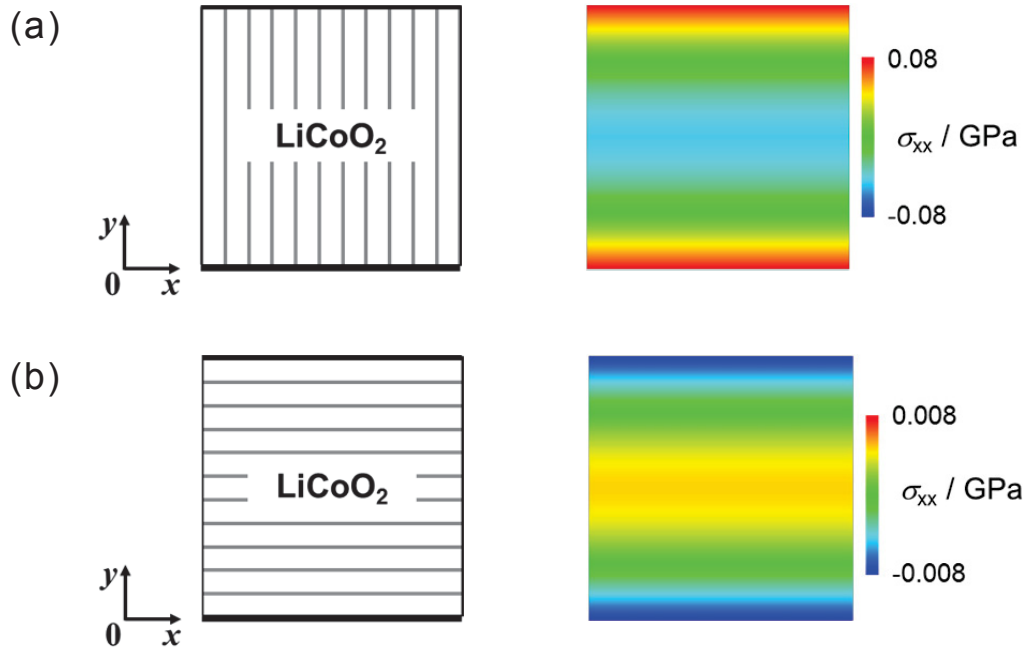

Fig. 5.2. Schematic illustrations of 2D single crystal models in which the (a) *c*-axis or (b) *a*-axis is parallel to the *x*-axis. The bold lines located on the upper or lower boundary of the *y*-axis represent the electrochemical interfaces. The figures on the right represent the distribution of σ_{xx} at a mean Li concentration of 0.605.

To clarify whether or not this variation in the elastic stress field affects Li diffusivity, the apparent diffusion coefficient, D_{app}, was estimated for each type of microstructure using PITT [97]. The kinetic rate constant of the

electrochemical reaction was set to 1.0×10^{-3} $cm^{5/2} \cdot mol^{-1/2} \cdot s^{-1}$ in order to prevent the surface reaction from becoming a rate-determining step. The boundary conditions at $x = 0$ and $x = L$ were $c_{x=0} = c_{x=L}$, and those at $y = 0$ and $y = L$ were $V = constant$. A potential step of about 8 mV (from 4.026 V to 4.018 V) was applied, and D_{app} was calculated from the time dependence of the current [97]. The apparent diffusion coefficients for each model are shown in Table 5.1.

Table 5.1. Apparent diffusion coefficients of Li in single-crystal models.

Microstructural Model	D_{app} ($\times 10^{-9}$ $cm^2 \cdot s^{-1}$)	
	E_{str} is omitted	E_{str} is included
Single Crystal Model		
(100)-oriented (Fig. 5.2 (a))	7.06	7.61
(003)-oriented (Fig. 5.2 (b))	0.073	0.073

The diffusion of Li along the y-axis began from the electrochemical reaction surface towards the crystal interior. Consequently, the D_{app} value of the (100) oriented model was larger than that of the (003) orientation model. Although the value obtained by multiplying the eigenstrain to the stress value was included in the Li diffusion potential, $\partial G_{sys}/\partial c$, Li diffusion was promoted in directions that reduced the stress gradient by reducing the Li concentration gradient. Therefore, in the case of the (100)-oriented model, the D_{app} value increased by about 8% when compared with the case where the elastic strain energy was not taken into account. In the (003)-oriented model, no significant difference was observed

since the misfit of the *a*-axis was small in comparison with the *c*-axis.

Table 5.2 shows D_{app} values for the polycrystalline microstructures shown in Fig. 5.1. In the present model, the mean value of $90-|90-\theta|$ was around 45°. Since all of the D_{app} values obtained were smaller than that of a single crystal where $|\theta| = 45°$, which was about 3.6×10^{-9} $cm^2 \cdot s^{-1}$, Li diffusion appeared to be restricted by the polycrystalline microstructure. Table 5.2 shows that the GB diffusivity exhibited a larger influence on D_{app} of the fine-grained model than that of the coarse-grained model. Moreover, D_{app} of the coarse-grained model also varied quite widely. This variation was mainly due to the assignment of an orientation angle to each grain, reflected in the value of $\theta_{relative}$ described in Sec. 4.3. The fine-grained microstructure exhibited less variation in Li diffusion, and it is thought that the existence of several possible diffusion paths led to a decrease in the degree of Li segregation.

The results also illustrate the effect of elastic strain energy, with its inclusion in G_{sys} causing an increase of a few percent in D_{app} of both the fine-grained and coarse-grained models. When the concentration of Li at the surface was higher than that in the bulk, the bulk was subject to compressive elastic stress, while the polycrystalline surface was subject to tensile elastic stress. This variation in the elastic stress field decreased when the Li concentration gradient between the bulk and surface was reduced. Therefore, when the bulk-to-surface Li concentration gradient was large, Li diffusion was promoted to alleviate the elastic stress field. The relative ratios calculated with either omission or inclusion of E_{str} of the most polycrystalline models, were smaller than that of the (100)-oriented model and larger than that of the

(003)-oriented model. However, the ratios were slightly varied depending on the polycrystalline microstructures. Therefore, the elastic stress field induced by the angle mismatch between neighboring grains is expected to perturb the influence of the elastic stress field generated by the concentration gradient. In addition, elastic strain energy may also play a larger role when the overall distortion of the diffusion medium is constrained, as observed in a polycrystalline thin film. This condition is therefore a potentially fruitful area for future research.

Table 5.2. Apparent diffusion coefficients of Li in polycrystalline models. The value of θ_{relative} is defined in Eq. (4.18). The values in parentheses denote the relative ratio calculated with either omission or inclusion of E_{str}.

Model	θ_{relative} (°)	D_{app} ($\times 10^{-9}$ cm^2·s^{-1})			
		$D_{\text{gb}} = D_{\text{self\_basal}}$		$D_{\text{gb}} = 0.01D_{\text{self\_basal}}$	
		E_{str} is omitted	E_{str} is included	E_{str} is omitted	E_{str} is included
Fine-Grained					
(a)	75.1	1.49	1.57 (1.05)	0.44	0.46 (1.05)
(b)	79.2	1.51	1.59 (1.05)	0.44	0.46 (1.05)
(c)	83.3	1.29	1.36 (1.05)	0.39	0.41 (1.05)
Coarse-Grained					
(d)	63.6	1.29	1.42 (1.10)	0.78	0.85 (1.09)
(e)	71.9	1.05	1.09 (1.04)	0.61	0.64 (1.05)
(f)	79.8	0.62	0.66 (1.06)	0.39	0.41 (1.05)

5.3.2 Discharge Properties

Figure 5.3 shows the constant-current discharge properties of the microstructures shown in Fig. 5.1. The black and blue lines denote the simulation results under the conditions of $D_{gb} = D_{self\_basal}$ and $D_{gb} = 0.01D_{self\_basal}$, respectively. The solid and broken lines indicate the inclusion and exclusion of the E_{str}, respectively. Fine-grained microstructures exhibited small variations in discharge properties (Figs. 5.3(a–c)), while coarse-grained microstructures exhibited larger variations (Figs. 5.3(d–f)). The differences in the discharge capacities of each microstructure appeared to have resulted from the Li segregation at the electrochemical reaction interface. Figure 5.4 shows the spatial distribution of Li concentration at a mean Li concentration of 0.65. In the case of the coarse-grained microstructure, a remarkable Li variation (Figs. 5.4(d–f)) was induced by initial assignment of the orientation angle distribution.

Another important feature shown in Fig. 5.3 is that the discharge capacities of the fine-grained models were smaller than those of the coarse-grained models when the GB behaved as a diffusion barrier. The effect of the elastic strain energy on the discharge properties was also evident. From the results of Fig. 5.3, the elastic strain energy slightly increased the discharge capacity. Figure 5.5 shows the differences in Li concentration (left) and von Mises stress (right). A greater decrease in the elastic stress field occurred in the vicinity of the region where the Li concentration increased. Although the effect of elastic strain energy was weaker than that of intergranular angle mismatch or GB diffusivity, it nonetheless led to a nontrivial change in Li diffusivity during discharge.

These tendencies imply that changes in the Li diffusivities manifested themselves directly as changes in the discharge capacities of the high discharge rate at 20C. Therefore, one obvious method for optimizing the discharge properties of $LiCoO_2$ is to synthesize $LiCoO_2$ with a textured microstructure that exhibits unidirectional grain orientations.

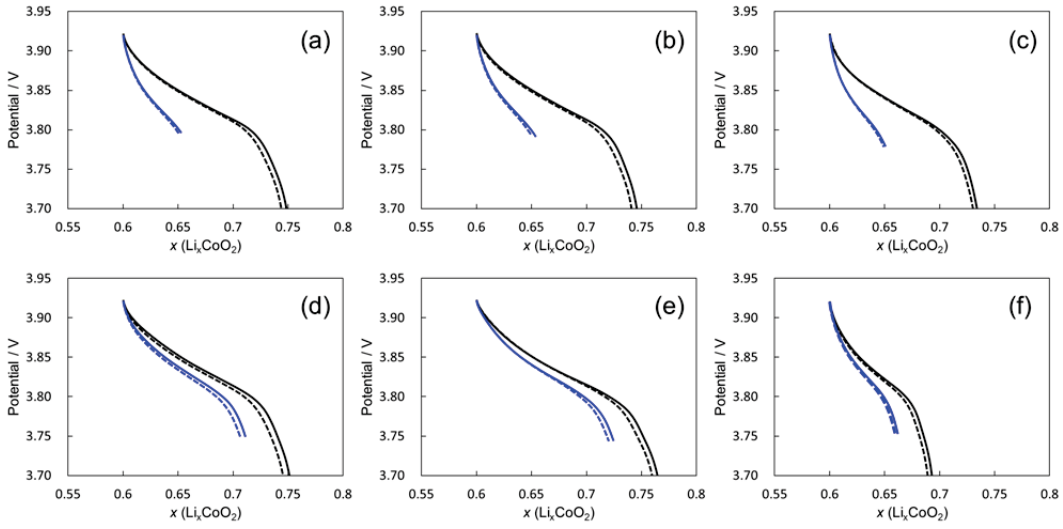

Fig. 5.3. Constant-current discharge properties at 298.15 K. The current density was fixed at 3.45 mA·cm^{-2}. The black and blue lines denote the simulation results under the conditions of $D_{gb} = D_{self\_basal}$ and $D_{gb} = 0.01D_{self\_basal}$, respectively. The solid and broken lines indicate the inclusion and exclusion of the E_{str}, respectively.

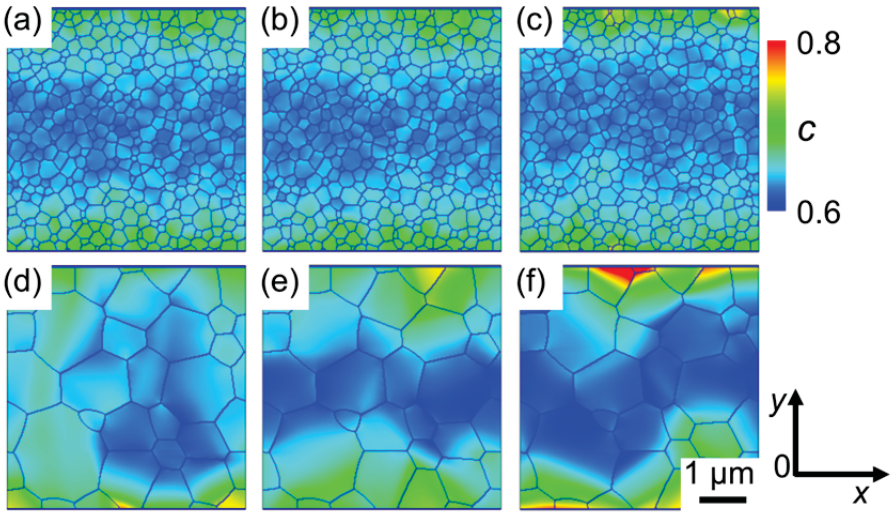

Fig. 5.4. Distribution of Li concentration during constant-current discharge. The Li transport direction was parallel to the y axis. The mean Li concentration in $LiCoO_2$ was about 0.65. D_{gb} was assumed to be equal to D_{self_basal}. E_{str} was included.

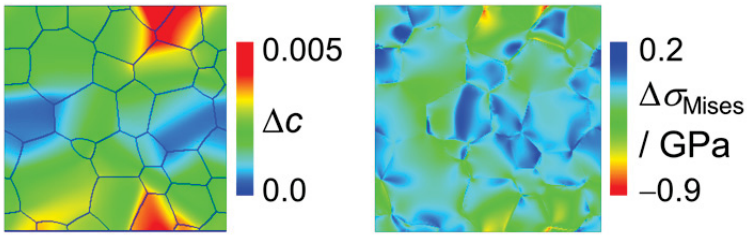

Fig. 5.5. Differences in the Li concentration (on the left hand side) and von Mises stress (on the right hand side), defined as $\Delta c = c(c_{mean} \approx 0.65) - c(c_{mean} \approx 0.61)$ and $\Delta\sigma_{Mises} = \sigma_{Mises}(c_{mean} \approx 0.65) - \sigma_{Mises}(c_{mean} \approx 0.61)$, using the results of model (e) in Fig. 5.4.

5.4 Summary

The discharge capacity of $LiCoO_2$ at a high discharge rate (*e.g.*, 20C-rate) was affected by the microstructure: specifically the grain size, spatial distribution of crystal orientations for each grain, and the GB diffusivity throughout the apparent Li diffusivity. The calculated results suggest that both the intergranular angle mismatch and the GB diffusivity are crucial parameters for evaluating the apparent discharge property.

A Li diffusion model for $LiCoO_2$, taking into account the elastic strain energy E_{str}, was developed. This model confirmed that the effect of a stress field on the apparent diffusion coefficient of Li varied depending on the relative relation between the crystallographic orientation and the Li diffusion direction. The elastic strain energy, varied according to the Li intercalation, also exhibited a non-negligible effect on the discharge properties. However, the ratio of D_{app} with E_{str} included to D_{app} with E_{str} omitted was smaller than: (i) the ratio of the chemical diffusion coefficient (7.06×10^{-9} $cm^2 \cdot s^{-1}$ at $Li_{0.6}CoO_2$) to the given self-diffusion coefficient (1×10^{-9} $cm^2 \cdot s^{-1}$); (ii) the ratio of D_{app} for a microstructure in which the grains were oriented such that $\theta = 0°$ to D_{app} for a microstructure with randomly oriented grains (~20 as estimated from Fig. 4.11).

Chapter 6
Conclusions and Future Work

6.1 Conclusions

In the search for ways to improve the performance of polymer-electrolyte fuel cells and Li-ion secondary batteries, the phase-field methods were applied to electrode materials with microstructures ranging from the nanometer to micrometer length scale. On the basis of the findings presented in each chapter, which are listed below, it can be concluded that phase-field modeling studies are useful for elucidating the driving forces behind nanostructure formation, as well as for gaining information on crucial aspects of anisotropic materials in order to quantitatively understand their atomic diffusion properties.

6.1.1 Phase-Field Modeling of Phase Transformations in Fe–Pt Nanoparticles

A phase-field model that describes the phase transformations and surface segregation in Fe–Pt binary-alloy nanoparticles was developed. The calculation results clearly showed that the atomic concentration and phase transformations inside these nanoparticles are sensitive to the alloy composition, particle size, and holding temperature. These results are consistent with the previously

reported experimental and simulation results. In addition, the calculation results suggested that the internal structure of the alloy nanoparticles often differ from that of the nominal bulk state because the variability in surface energy caused by the particle size distribution influences the thermal equilibrium microstructure of the nanoparticles. Atomistic simulations such as first-principles calculations, molecular dynamics, and Monte-Carlo simulation have been regarded as powerful tools to accurately probe the mechanism of microstructural formation from the viewpoint of atomic motion. However, in practical calculations, the system size is limited by the computational cost. As an alternative approach, it is concluded that the method proposed in this study can provide useful information on the internal structure of single-alloy nanoparticles.

6.1.2 Surface Segregations in Platinum-Based Alloy Nanoparticles

The radial distributions of the phase transformations and surface segregation in the various single-alloy nanoparticles were examined as functions of the input values of alloy composition, particle diameter, and temperature. To obtain the general attributes of the abovementioned relation, the radial distribution of the phase state and the atomic compositions of CrPt, FePt, CoPt, NiPt, CuPt, PdPt, IrPt, and AuPt nanoparticles with diameters below 10 nm at 973 K were investigated. The results revealed that the compositional variation within a

single particle depends on the balance between the atomic interaction within particles and surface energy, and the specific equilibrium points vary significantly with the alloy combination. To improve catalytic activity, alloy systems that have a microstructure with a Pt skin layer on the particle surface are worth considering. Among the examined binary alloys, the Cr–Pt system comes closest to having such a structure. Furthermore, a ternary-alloy system was briefly examined and it is suggested that a more desirable distribution of the phase state and atomic concentration inside a particle can be obtained by adopting the ternary-alloy system. In the case of $Ir_{0.4}Cr_{0.1}Pt_{0.5}$ nanoparticles, Cr improves the stability of the Pt-shell–Ir-core structure. This study has provided a basis for conducting additional extended surveys targeting binary- and ternary-alloy systems.

6.1.3 Numerical Study of Li Diffusion in Polycrystalline $LiCoO_2$

To gain a quantitative understanding of the relationship between the microstructural morphology and Li diffusivity, phase-field models for non-Fickian Li diffusion in two-dimensional polycrystalline microstructures were developed. The simulation results showed that the apparent Li diffusivity is sensitive to the diffusivity of grain boundaries, spatial distribution of the crystal orientation of each grain, and grain size. If we can experimentally

evaluate the grain size relative to the electrode size from a 2D image, we can roughly estimate the possible in-plane variation in electrode performance.

This study is expected to facilitate the understanding of Li transport properties such as those in a thin-film electrode for use in an all-solid-state battery. A comparison of the simulation results with the experimentally measured quantities that represent consequences of the multi-step process provides a quantitative understanding of each elemental step in the Li transport process. Moreover, the rate-determining step may change from the internal diffusion to the surface reaction when the surface reaction resistance increases. Therefore, the effect of microstructure on the discharge properties was subsequently investigated and is presented in the next chapter.

6.1.4 Effect of Microstructure on the Discharge Properties of Polycrystalline $LiCoO_2$

The constant-current discharge properties of polycrystalline $LiCoO_2$ were theoretically investigated in relation to the grain size, spatial distribution of the crystal orientation of each grain, and grain boundary (GB) diffusivity. The simulation results showed that the microstructure notably affects the discharge properties at a high discharge rate by modifying Li diffusivity. Intergranular angle mismatch and GB diffusivity are crucial parameters for the evaluation of apparent discharge properties. Since Li diffusivity is promoted to alleviate elastic stress, discharge capacity is slightly increased. Although the effect of

elastic strain energy is weaker than the effects of intergranular angle mismatch and GB diffusivity, it leads to a nontrivial change in Li diffusivity during discharge. Therefore, an obvious method for optimizing the discharge properties of $LiCoO_2$ is to synthesize $LiCoO_2$ with a textured microstructure exhibiting unidirectional grain orientations.

6.2 Future Work

1. In order to design and stably retain a thinly coated Pt surface structure in a nanoparticle, more extensive ternary-alloy systems as functions of particle size and heat treatment temperature will be explored. Moreover, simulations for multi-particle systems along with the particle size distributions will be needed for practical applications in real systems.

2. For the study on Li diffusivity in a practical electrode structure used in LIBs, simulations of Li diffusion in $LiCoO_2$, potential distribution in $LiCoO_2$ and the electrolyte, and mass transport of Li ions in the electrolyte will be required. To reduce the simulation time in order to complete the study, a more efficient numerical algorism including a parallelized code must be developed.

3. The present phase-field method is developed by linking it with CALPHAD data and material parameters such as mobility, compositional dependence of lattice parameters, elastic constants, and interfacial energies. To perform broad surveys on alloy phases in multinary alloy systems, parameter estimation utilizing first-principles calculations should be given thorough consideration.

Bibliography

[1] S. Chu, A. Majumdar, Nature 488 (2012) 294−303.

[2] B. Scrosati, J. Garche, J. Power Sources 195 (2010) 2419−2430.

[3] M. Park, X. Zhang, M. Chung, G.B. Less, A.M. Sastry, J. Power Sources 195 (2010) 7904−7929.

[4] K.Y. Chan, J. Ding, J. Ren, S. Cheng, K.Y. Tsang, J. Mater. Chem. 14 (2004) 505−516.

[5] K.A. Mauritz, R.B. Moore, Chem. Rev. 104 (2004) 4535−4585.

[6] C.Y. Wang, Chem. Rev. 104 (2004) 4727−4766.

[7] V. Mehta, S. Cooper, J. Power Sources 114 (2003) 32−53.

[8] M.K. Debe, Nature 486 (2012) 43−51.

[9] Y. Ma, P.B. Balbuena, Surf. Sci. 602 (2008) 107−113.

[10] J. Greeley, I.E.L. Stephens, A.S. Bondarenko, T.P. Johansson, H.A. Hansen, T.F. Jaramillo, J. Rossmeisl, I. Chorkendorff, J.K. Norskov, Nature Chem. 1 (2009) 552−556.

[11] C. Wang, D. Li, M. Chi, J. Pearson, R.B. Rankin, J. Greeley, Z. Duan, G. Wang, D. van der Vliet, K.L. More, N.M. Markovic, V.R. Stamenkovic, J. Phys. Chem. Lett. 3 (2012) 1668−1673.

[12] A. Bonakdarpour, R. Löbel, R.T. Atanasoski, G.D. Vernstrom, A.K. Schmoeckel, M.K. Debe, J.R. Dahn, J. Electrochem. Soc. 153 (2006) A1835−A1846.

[13] D. Alloyeau, G. Prévot, Y.L. Bouar, T. Oikawa, C. Langlois, A. Loiseau, C. Ricolleau, Phys. Rev. Lett. 105 (2010) 255901.

[14] R. Ferrando, J. Jellinek, R.L. Johnston, Chem. Rev. 108 (2008) 845−910.

[15] V.R. Stamenkovic, B.S. Mun, K.J.J. Mayrhofer, P.N. Ross, N.M. Markovic, J. Am. Chem. Soc. 128 (2006) 8813−8819.

[16] T. Takeshita, H. Murata, T. Hatanaka, Y. Morimoto, ECS Trans. 16 (2008) 367−373.

[17] K. Mizushima, P.C. Jones, P.J. Wiseman, J.B. Goodenough, Mat. Res. Bull. 15 (1980) 783−789.

[18] E. Plichta, M. Salomon, S. Slane, M. Uchiyama, D. Chua, W.B. Ebner, H.W. Lin, J. Power Sources 21 (1987) 25−31.

[19] J.J. Auborn, Y.L. Barberio, J. Electrochem. Soc. 134 (1987) 638−641.

[20] E. Antolini, Solid State Ionics 170 (2004) 159−171.

[21] J.-M. Tarascon, M. Armand, Nature 414 (2001) 359−367.

[22] J. R. Wilson, J. S. Cronin, S. A. Barnett, S. J. Harris, J. Power Sources 196 (2011) 3443−3447.

[23] X. Wang, I. Loa, K. Kunc, K. Syassen, M. Amboage, Phys. Rev. B 72 (2005) 224102.

[24] J. Sugiyama, K. Mukai, Y. Ikedo, H. Nozaki, M. Månsson, I. Watanabe, Phys. Rev. Lett. 103 (2009) 147601.

[25] M. Okubo, Y. Tanaka, H. Zhou, T. Kudo, I. Honma, J. Phys. Chem. B 113 (2009) 2840−2847.

[26] A. Van der Ven, G. Ceder, M. Asta, P.D. Tepesch, Phys. Rev. B 64 (2001) 184307.

[27] H. Xia, L. Lu, Electrochim. Acta 52 (2007) 7014−7021.

[28] J. Xie, N. Imanishi, T. Matsumura, A. Hirano, M. Matsumura, Y. Takeda,

O. Yamamoto, Solid State Ionics 179 (2008) 362−370.

[29] J.B. Bates, N.J. Dudney, B.J. Neudecker, F.X. Hart, H.P. Jun, S.A. Hackney, J. Electrochem. Soc. 147 (2000) 59−70.

[30] L.Q. Chen, Ann. Rev. Mater. Res. 32 (2002) 113−140.

[31] J.W. Cahn, J. Chem. Phys. 42 (1965) 93−99.

[32] S.M. Allen, J.W. Cahn, Acta Metall. 27 (1979) 1085−1095.

[33] H.L. Lukas, S.G. Fries, B. Sundman, Computational Thermodynamics–The Calphad Method, Cambridge Univ. Press, Cambridge, 2007.

[34] T. Koyama, Computational Materials Design: Simulation of Microstructures, Uchida Rokakuho Publishing, Tokyo, 2011.

[35] J.W. Cahn, J.E. Hilliard, J. Chem. Phys. 28 (1958) 258−267.

[36] Y. Saito, An Introduction to the Kinetics of Diffusion Controlled Microstructural Evolutions in Materials, CORONA, Tokyo, 2000.

[37] T. Koyama, Y. Tsukada, Elasticity of Microstructure and Phase Transformation: Introduction to Phase-Field Microelasticity Theory, (Uchida Rokakuho Publishing, Tokyo, 2012.

[38] A.J. Bard, L.R. Faulkner, Electrochemical Methods–Fundamentals and Applications, Second ed., John Wiley & Sons, Inc., Hoboken, 2001.

[39] R.J. Leveque, Finite Volume Methods for Hyperbolic Problems, Cambridge Univ. Press, Cambridge, 2002.

[40] F.L. Williams, D. Nason, Surf. Sci. 45 (1974) 377−408.

[41] R.V. Chepulskii, W.H. Butler, Phys. Rev. B 72 (2005) 134205.

[42] M. Müller, K. Albe, Phys. Rev. B 72 (2005) 094203.

[43] M. Müller, P. Erhart, K. Albe, Phys. Rev. B 76 (2007) 155412.

[44] R.V. Chepulskii, W.H. Butler, A. van de Walle, S. Curtarolo, Scr. Mater. 62 (2010) 179−182.

[45] P. Moskovkin, M. Hou, J. Alloys Compd. 434−435 (2007) 550−554.

[46] L.V. Pourovskii, A.V. Ruban, I.A. Abrikosov, Y.K. Vekilov, B. Johansson, Phys. Rev. B 64 (2001) 035421.

[47] M. Schurmans, J. Luyten, C. Creemers, R. Declerck, M. Waroquier, Phys. Rev. B 76 (2007) 174208.

[48] H. Deng, W. Hu, X. Shu, L. Zhao, B. Zhang, Surf. Sci. 517 (2002) 177−185.

[49] G. Wang, M.A. Van Hove, P.N. Ross, M.I. Baskes, J. Chem. Phys. 122 (2005) 024706.

[50] T. Koyama, Sci. Technol. Adv. Mater. 9 (2008) 013006.

[51] T. Koyama, H. Onodera, J. Jpn. Inst. Met. 68 (2004) 1008−1012.

[52] Y.K. Takahashi, T. Koyama, M. Ohnuma, T. Ohkubo, K. Hono, J. Appl. Phys. 95 (2004) 2690−2696.

[53] S. Yamakawa, K. Okazaki-Maeda, M. Kohyama, S. Hyodo, J. Phys.: Conf. Ser. 100 (2008) 072042.

[54] B. Zhou, A.C. Powell, J. Membr. Sci. 268 (2006) 150−164.

[55] W. Villanueva, K. Grönhagen, G. Amberg, J. Ågren, Phys. Rev. E 77 (2008) 056313.

[56] A.T. Dinsdale, CALPHAD 15 (1991) 317−425.

[57] K. Asp, J. Ågren, Acta Mater. 54 (2006) 1241−1248.

[58] P. Fredriksson, B. Sundman, CALPHAD 25 (2001) 535−548.

[59] K. Binder, J.L. Lebowitz, M.K. Phani, M.H. Kalos, Acta Metall. 29 (1981) 1655−1665.

[60] A. Dannenberg, M.E. Gruner, A. Hucht, P. Entel, Phys. Rev. B 80 (2009) 245438.

[61] W.R. Tyson, W.A. Miller, Surf. Sci. 62 (1977) 267−276.

[62] J.W. Arblaster, Platinum Met. Rev. 50 (2006) 118−119.

[63] H.E. Schaefer, Phys. Status Solidi A 102 (1987) 47−65.

[64] M. Watanabe, T. Masumoto, D.H. Ping, K. Hono, Appl. Phys. Lett. 76 (2001) 3971−3973.

[65] T. Miyazaki, O. Kitakami, S. Okamoto, Y. Shimada, Z. Akase, Y. Murakami, D. Shindo, Y.K. Takahashi, K. Hono, Phys. Rev. B 72 (2005) 144419.

[66] C.B. Rong, N. Poudyal, G.S. Chaubey, V. Nandwana, R. Skomski, Y.Q. Wu, M.J. Kramer, J.P. Liu, J. Appl. Phys. 102 (2007) 043913.

[67] C.B. Rong, D.R. Li, V. Nandwana, N. Poudyal, Y. Ding, Z.L. Wang, H. Zeng, J.P. Liu, Adv. Mater. 18 (2006) 2984−2988.

[68] Z.L. Wang, J.M. Petroski, T.C. Green, M.A. El-Sayed, J. Phys. Chem. B 102 (1998) 6145−6151.

[69] A. Barybinand, V. Shapovalov, J. Appl. Phys. 109 (2011) 034303.

[70] S. Zhao, S. Wang, H. Ye, J. Phys. Soc. Jpn. 70 (2001) 2953−2957.

[71] H.L. Xin, J.A. Mundy, Z. Liu, R. Cabezas, R. Hovden, L.F. Kourkoutis, J. Zhang, N.P. Subramanian, R. Makharia, F.T. Wagner, D.A. Muller, Nano Lett. 12 (2012) 490−497.

[72] J. Preusner, S. Prins, R. Volkl, Z.-K. Liu, U. Glatzel, Mat. Sci. Eng. A 510−511 (2009) 322−327.

[73] D. Kim, J.E. Saal, L. Zhou, S. Shang, Y. Du, Z. Liu, CALPHAD 35 (2011)

323−330.

[74] X. Lu, B. Sundman, J. Ågren, CALPHAD 33 (2009) 450−456.

[75] T. Abe, B. Sundman, H. Onodera, J. Phase Equilib. Diffus. 27 (2006) 5−13; http://www.nims.go.jp/cmsc/pst/database/cu-elem/cupt/cupt_abe.TDB.

[76] P.E.A. Turchi, V. Drchal, J. Kudrnovský, Phys. Rev. B 74 (2006) 064202.

[77] T. Abe, Computational Materials Design: Computational Thermodynamics, Uchida Rokakuho Publishing, Tokyo, 2011, pp. 157−160.

[78] V. Grolier, R. Schmid-Fetzer, J. Electron. Mater. 37 (2008) 264−278.

[79] Y.N. Wen, J.M. Zhang, Solid State Commun. 144 (2007) 163−167.

[80] B.Q. Fu, W. Liu, Z.L. Li, Appl. Surf. Sci. 255 (2009) 8511−8519.

[81] M.J. Mehl, D.A. Papaconstantopoulos, Phys. Rev. B 54 (1996) 4519−4530.

[82] Y. Ouyang, H. Chen, X. Zhong, J. Mater. Sci. Technol., 19 (2003) 243−246.

[83] A. Khoutami, B. Legrand, G. Tréglia, Surf. Sci. 287−288 (1993) 851−856.

[84] B.J. Lee., CALPHAD 17 (1993) 251−268.

[85] C. Zhang, J. Zhu, D. Morgan, Y. Yang, F. Zhang, W.S. Cao, Y.A. Chang, CALPHAD 33 (2009) 420−424.

[86] A. Bonakdarpour, J. Wenzel, D.A. Stevens, S. Sheng, T.L. Monchesky, R. Löbel, R.T. Atanasoski, A.K. Schmoeckel, G.D. Vernstrom, M K. Debe, J.R. Dahn, J. Electrochem. Soc. 152 (2005) A61−A72.

[87] P. Ramadass, B. Haran, R. White, B.N. Popov, J. Power Sources 123 (2003) 230−240.

[88] S. Santhanagopalan, Q. Guo, P. Ramadass, R.E. White, J. Power Sources 156 (2006) 620−628.

[89] S. Santhanagopalan, Q. Guo, R.E. White, J. Electrochem. Soc. 154 (2007)

A198−A206.

[90] B.C. Han, A. Van der Ven, D. Morgan, G. Ceder, Electrochim. Acta 49 (2004) 4691−4699.

[91] G.K. Singh, G. Ceder, M.Z. Bazant, Electrochim. Acta 53 (2008) 7599−7613.

[92] D.W. Chung, N. Balke, S.V. Kalinin, R.E. Garćia, J. Electrochem. Soc. 158 (2011) A1083−A1089.

[93] T. Abe, T. Koyama, CALPHAD 35 (2011) 209−218.

[94] A. Van der Ven, M.K. Aydinol, G. Ceder, G. Kresse, J. Hafner, Phys. Rev. B 58 (1998) 2975−2987.

[95] C. Wolverton, A. Zunger, Phys. Rev. B 57 (1998) 2242−2252.

[96] Q. Zhang, Q. Guo, R.E. White, J. Electrochem. Soc. 153 (2006) A301−A309.

[97] C.J. Wen, B.A. Boukamp, R.A. Huggins, W. Weppner, J. Electrochem. Soc. 126 (1979) 2258−2266.

[98] Y.I. Jang, B.J. Neudecker, N.J. Dudney, Electrochem. Solid-State Lett. 4 (2001) A74−A77.

[99] J.N. Reimers, J.R. Dahn, J. Electrochem. Soc. 139 (1992) 2091−2097.

[100] D. Gryaznov, J. Fleig, J. Maier, Solid State Ionics 177 (2006) 1583−1586.

[101] S.G. Kim, D.I. Kim, W.T. Kim, Y.B. Park, Phys. Rev. E 74 (2006) 061605.

[102] C.A.J. Fisher, R. Huang, T. Hitosugi, H. Moriwake, A. Kuwabara, Y.H. Ikuhara, H. Oki, Y. Ikuhara, Nanosci. Nanotechnol. Lett. 4 (2012) 165−168.

[103] H. Moriwake, A. Kuwabara, C.A.J. Fisher, R. Huang, T. Hitosugi, Y.H. Ikuhara, H. Oki, Y. Ikuhara, Adv. Mater. 25 (2013) 618−622.

[104] J. Christensen, J. Newman, J. Electrochem. Soc. 153 (2006) A1019−A1030.

[105] S. Renganathan, G. Sikha, S. Santhanagopalan, R.E. White, J. Electrochem. Soc. 157 (2010) A155−A163.

[106] Y.U. Wang, Y.M. Jin, A.G. Khachaturyan, J. Appl. Phys. 91 (2002) 6435−6451.

[107] S.Y. Hu, L.Q. Chen, Acta Mater. 49 (2001) 1879−1890.

[108] F.X. Hart, J.B. Bates, J. Appl. Phys. 83 (1998) 7560−7566.

[109] Y. Takahashi, N. Kijima, K. Tokiwa, T. Watanabe, J. Akimoto, J. Phys.: Condens. Matter 19 (2007) 436202.

[110] Y. Takahashi, N. Kijima, K. Dokko, M. Nishizawa, I. Uchida, J. Akimoto, J. Solid State Chem. 180 (2007) 313−321.

[111] S.I. Pyun, J.Y. Go, T.S. Jang, Electrochim. Acta 49 (2004) 4477−4486.

List of Papers

The present thesis is based on the following papers:

[I] S. Yamakawa, R. Asahi, T. Koyama, “Phase-Field Modeling of Phase Transformations in Platinum-Based Alloy Nanoparticles,” Mater. Trans. 54 (2013) 1242−1249.

[II] S. Yamakawa, R. Asahi, T. Koyama, “Surface Segregations in Platinum-Based Alloy Nanoparticles,” accepted for publication in Surface Science.

[III] S. Yamakawa, H. Yamasaki, T. Koyama, R. Asahi, “Numerical Study of Li Diffusion in Polycrystalline $LiCoO_2$,” J. Power Sources 223 (2013) 199−205.

[IV] S. Yamakawa, H. Yamasaki, T. Koyama, R. Asahi, “Effect of Microstructure on Discharge Properties of Polycrystalline $LiCoO_2$,” Solid State Ionics (in press).

The following paper is closely related to the present thesis:

[V] S. Yamakawa, K. Okazaki-Maeda, M. Kohyama, S. Hyodo, “Phase-Field Model for Deposition Process of Platinum Nanoparticles on Carbon Substrate,” J. Phys.: Conference Series 100 (2008) 072042.

List of Oral Presentations

[I] S. Yamakawa, H. Yamasaki, T. Koyama, R. Asahi, “Phase-Field Modelling of Lithium Intercalation in Polycrystalline Oxide,” JSME 24th Computational Mechanics Division Conference (CMD2011), Okayama, Japan, Oct 8−10, 2011.

[II] S. Yamakawa, H. Yamasaki, T. Koyama, R. Asahi, “Phase-Field Modeling of Lithium Intercalation in Polycrystalline $LiCoO_2$,” 52nd Battery Symposium in Japan, Tokyo, Japan, Oct 17−20, 2011.

[III] S. Yamakawa, R. Asahi, T. Koyama, “Phase-Field Simulation of Alloy Nanoparticles,” 150th Annual Meeting of the Japan Institute of Metals, Tokyo, Japan, March 28−30, 2012.

[IV] S. Yamakawa, S. Sakurai, R. Asahi, T. Koyama, “Phase-Field Study of Compositional Variation within Bimetallic Nanoparticle,” JSME 25th Computational Mechanics Division Conference (CMD2012), Kobe, Japan, Oct 6−9, 2012.

[V] S. Yamakawa, H. Yamasaki, K. Ide, T. Koyama, R. Asahi, “Effect of Microstructure on Li Diffusivity of Polycrystalline $LiCoO_2$,” JSME 26th Computational Mechanics Division Conference (CMD2013), Saga, Japan, Nov 2−4, 2013.

List of Poster Presentations

[I] S. Yamakawa, H. Yamasaki, T. Koyama, R. Asahi, “Phase-Field Modeling of Li Intercalation in Polycrystalline $LiCoO_2$,” the 3rd International Symposium on Advanced Microscopy and Theoretical Calculations (AMTC3), Gifu, Japan, May 9−11, 2012.

[II] S. Yamakawa, R. Asahi, T. Koyama, “Phase-field Study of Phase Transformations in Platinum-based Alloy Nanoparticles,” the 5th International Symposium on Designing, Processing and Properties of Advanced Engineering Materials (ISAEM-2012) and AMDI-3, Toyohashi, Japan, Nov 5−8, 2012.

[III] S. Yamakawa, R. Asahi, T. Koyama, “Phase-Field Modeling on Phase Transformations in Platinum-Based Alloy Nanoparticles,” 2012 MRS Fall Meeting, Boston, MA, USA, Nov 25−30, 2012.

[IV] S. Yamakawa, H. Yamasaki, T. Koyama, R. Asahi, “Microstructural Factors Affecting Lithium Diffusion in Lithium Cobalt Oxide,” the 19th International Conference on Solid State Ionics (SSI-19), Kyoto, Japan, June 2−7, 2013.